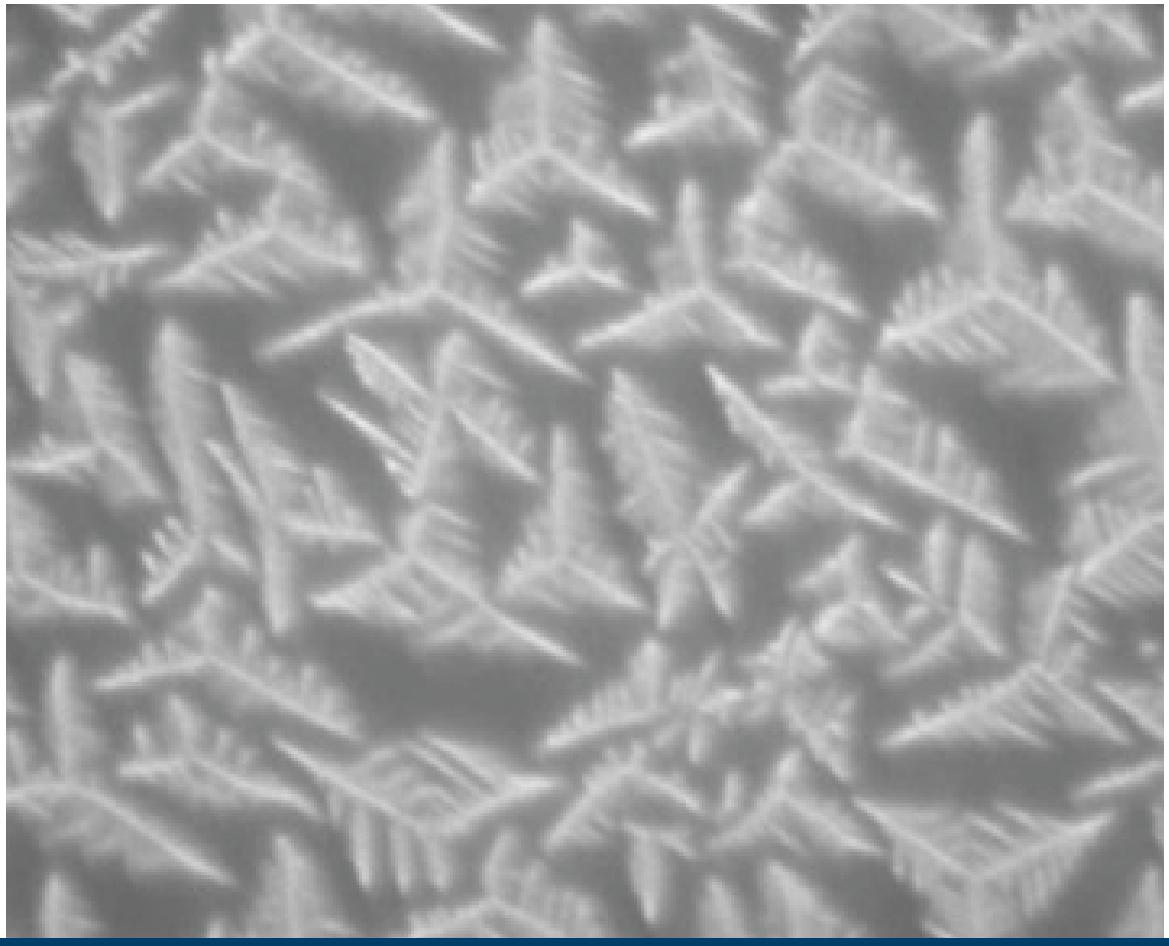

Different growth modes of molecular adsorbate systems and 2D materials investigated by low-energy electron microscopy

Janina Elisabeth Felter

Schlüsseltechnologien / Key Technologies
Band / Volume 206
ISBN 978-3-95806-434-8

Mitglied der Helmholtz-Gemeinschaft

JÜLICH
Forschungszentrum

Schriften des Forschungszentrums Jülich
Reihe Schlüsseltechnologien / Key Technologies Band / Volume 206

Forschungszentrum Jülich GmbH
Peter Grünberg Institut (PGI)
Functional Nanostructures at Surfaces (PGI-3)

Different growth modes of molecular adsorbate systems and 2D materials investigated by low-energy electron microscopy

Janina Elisabeth Felter

Schriften des Forschungszentrums Jülich
Reihe Schlüsseltechnologien / Key Technologies Band / Volume 206

ISSN 1866-1807 ISBN 978-3-95806-434-8

Bibliografische Information der Deutschen Nationalbibliothek.
Die Deutsche Nationalbibliothek verzeichnet diese Publikation in der
Deutschen Nationalbibliografie; detaillierte Bibliografische Daten
sind im Internet über http://dnb.d-nb.de abrufbar.

Herausgeber und Vertrieb:	Forschungszentrum Jülich GmbH Zentralbibliothek, Verlag 52425 Jülich Tel.: +49 2461 61-5368 Fax: +49 2461 61-6103 zb-publikation@fz-juelich.de www.fz-juelich.de/zb
Umschlaggestaltung:	Grafische Medien, Forschungszentrum Jülich GmbH
Druck:	Grafische Medien, Forschungszentrum Jülich GmbH
Copyright:	Forschungszentrum Jülich 2019

Schriften des Forschungszentrums Jülich
Reihe Schlüsseltechnologien / Key Technologies, Band / Volume 206

D 82 (Diss. RWTH Aachen University, 2018)

ISSN 1866-1807
ISBN 978-3-95806-434-8

Vollständig frei verfügbar über das Publikationsportal des Forschungszentrums Jülich (JuSER)
unter www.fz-juelich.de/zb/openaccess.

"Supercalifragilisticexpialigetisch"

- *Mary Poppins*

Contents

Chapter 1

Introduction

In most electronic devices, as in computers, mobile phones and solar cells, silicon is still the base material. However, new classes of materials exhibit great potential, on the one hand, for higher performance and lower power consumption in conventional semiconductor technology and, on the other hand, for opening new markets, as for flexible, light weight and transparent nanotechnology: organic molecules and 2D materials [2, 45, 49]. Both classes of materials are subject of the studies reported in this thesis.

Organic Molecules

Organic molecules have gained considerable attention for both fundamental research and device application over the last three decades. They have shown high potential for thin film applications like organic solar cells (OSC) [77, 194], light emitting diodes (OLED) [64, 81, 162] and field-effect transistors (OTFT) [89]. Today, such devices are entering our daily life in smart phone displays and TV screens [49, 133]. In order to access the full potential of organic molecules, a deep understanding of the fundamental mechanisms, which govern the properties of the active layers in such devices, is necessary. The initial growth and the formation of the first molecular layer on a substrate are of particular interest as this layer acts as a template for the further growth of the organic film and determines the electronic properties of the interface [171, 195, 200].

In this context, the adsorption of large π-conjugated molecules on different metal substrates is of great interest since these systems represent prototype systems for which the intermolecular interactions and the interactions between molecule and metal surface can be studied in detail. These two kinds of interactions determine the molecular orientation, the ordering and growth of the first layer, and therefore the properties of the interface [67, 154, 160, 164].

The investigation of this decisive interplay between different interaction mechanisms for molecules on metal substrates and, in particular, its influence on the growth mode, is the subject of the first part of this thesis. For this purpose, two model systems are investigated (mainly) by Low-Energy Electron Microscopy (LEEM) and Diffraction (LEED). These techniques have proven to be excellent tools to investigate the lateral growth of molecular (mono)layers in-situ and in real time [3, 34, 67, 71–73, 82, 107, 109, 140, 141, 158].

The initial growth of the perylene derivative 3,4,9,10-perylene tetracarboxylic dianhydride (PTCDA) on Cu(001) is investigated quantitatively. While it is well

known that the attractive intermolecular interaction of the PTCDA molecules leads to the growth of compact islands at already very low coverage [54, 66], this process is quantified in this work by determining two important parameters which influence the island formation: the cohesion energy of two PTCDA molecules and the diffusion barrier of the adsorbed molecules. While the first depends mainly on the molecule-molecule interaction, the second is strongly influenced by the interaction between molecule and substrate.
In contrast to PTCDA, the closely related molecule 1,4,5,8-naphthalene tetracarboxylic dianhydride (NTCDA) exhibits a completely different growth mode on the same substrate. It does not form compact islands but a dendrite-like network. This interesting growth mode, which was not found for NTCDA on other substrates, e.g., on Ag(111) [62], can be explained by the interplay of molecule-molecule and molecule-substrate interactions favouring growth of long and thin molecular chains.

2D materials
Another group of materials which has great potential for applications in modern electronics are 2D materials [2, 26, 45, 64]. Since a single layer of graphene was successfully exfoliated for the first time in 2004 [116], the field of 2D materials increased rapidly. Besides graphene, hexagonal boron nitride (hBN) is a prominent and frequently studied member of this family. It has a honeycomb structure, similar to graphene, but is formed of nitrogen and boron atoms. Because of its structural and electronic properties, in particular, its insulating nature [184], it is of highest interest in hetero-epitaxial systems in conjunction with other 2D materials or molecules [2, 31, 55, 193].
Single hBN layers are typically produced either by mechanical ex-foliation of single crystals [31] or in-situ by chemical vapour deposition utilizing a catalytic process when a metal surface is annealed in an atmosphere of borazine or other precursors [30, 86, 98, 120, 151, 152, 161]. Especially the latter process has a high potential as scalable method and guarantees the lowest level of contamination.
The growth of hBN via chemical vapour deposition was studied on several metal substrates. Generally, the degree of reactivity of the substrate has strong influence on the growth rate and on the morphology of the hBN layer [7, 21, 30, 112, 122, 137, 161]. For highly reactive metals, strongly corrugated and buckled films were found while with decreasing reactivity the films become flatter and more weakly bonded to the substrate. The Cu(111) surface has been recently shown to exhibit a rather weak hBN/metal interaction [21, 80]. This weak bonding could be very important for processes where the substrate has to be etched away for further device production.
Therefore, the growth of hBN on this surface is investigated in detail in the second part of this thesis with the aim to draw conclusions about the atomic processes on the surface and the interplay between the different interaction mechanisms. In contrast to aromatic organic molecules on metal surfaces where the intermolecular interactions are mostly based on van-der Waals interaction, electrostatic forces and hydrogen bonds, the borazine molecules have to dissociate or at least dehydrogenate to form covalent bonds between each other in order to form a layer of hBN. This explains the particular importance of the molecule-substrate interaction in this case.

In the case of hBN on Cu(111), fractal structures with three strongly preferred growth branches are found, which are mostly well aligned with the Cu(111) substrate and exhibit a three-fold symmetric shape. Both, the fractal island shapes as well as the preferred growth directions can be explained by rather simple assumptions and growth models involving DLA and different dehydrogenation states.

Combining organic molecules and 2D materials

Beside its application in van der Waals heterostructures, hBN is of highest interest as template for the formation of epitaxial layers of organic molecules because it could lead to the decoupling of these adsorbates from the metal surface [32, 96, 138]. Recently, Brülke et al. [22] have shown that a monolayer of hBN on Cu(111) is able to decouple the first PTCDA layer from the copper substrate chemically and electronically. In this thesis, the growth and lateral structure of PTCDA on hBN/Cu(111) are discussed which also indicate the weak interaction between molecules and 2D substrate.

Outline

The structure of this thesis is as follows:

After this short introduction, the LEEM setup and the complementary techniques are introduced in chapter 2. Additionally, the image processing, sample preparation and temperature determination are discussed. A brief introduction into the theoretical background of growth theory is given in chapter 3.

In chapter 4, the growth of compact PTCDA islands on Cu(001) is reported. By applying methods developed for atomic nucleation on surfaces, the critical cluster size for the formation of stable clusters, the diffusion barrier for individual molecules and, in combination with pair-potential calculations, the cohesion energy of a cluster of two molecules are determined for this system.

The growth of NTCDA on Cu(001) is the topic of chapter 5. In contrast to similar organic/metal systems [54, 57, 62, 76, 102, 106, 107], NTCDA does not form compact islands on Cu(001). Instead, a static domain shape is observed during growth of the first layer which is explained with a substrate-induced dendrite-like growth mode. Additionally, this system is used as prototype system for a proof of principle experiment: momentum microscopy of a single molecular domain performed with the LEEM/PEEM instrument. This is important since the k-space maps of systems with many symmetry-equivalent domains often cannot be analysed unambiguously. Furthermore, a second phase found at higher substrate temperatures is discussed briefly.

In chapter 6, the self-terminated growth of the first hBN layer on Cu(111) is described. For this system, fractal structures with three strongly preferred growth branches are found that are mostly well aligned with the Cu(111) substrate and exhibit a three-fold symmetric shape. Additionally, the growth at various substrate temperatures is discussed.

The growth and lateral structure of PTCDA on hBN/Cu(111) is investigated in chapter 7. It is found that PTCDA on hBN/Cu(111) forms a herringbone structure very similar to that on Au(111) indicating a weak interaction between the molecules and the 2D substrate.

Finally, this work concludes with a summary of the most important results and an outlook.

Chapter 2

Experimental setup

In this chapter, an overview of the experimental setup is given. First, the central tool, the Low-Energy Electron Microscope (LEEM), and its contrast mechanisms are discussed. Then, Low-Energy Electron Diffraction (LEED), Photoemission Electron Microscopy (PEEM) and Angular-Resolved Photoemission Spectroscopy (ARPES) are described. Additionally, the influence of beam damage on the measurements and the image processing are discussed. The complementary methods, Scanning Tunneling Microscopy (STM), Normal Incidence X-ray Standing Wave (NIXSW) measurements and pair potential calculations, are introduced briefly in the following. Finally, sample preparation and temperature determination are described.

2.1 LEEM and related techniques

All LEEM experiments are performed in an Aberration Corrected Low-Energy Electron Microscope (Elmitec AC-LEEM 3) with a lateral resolution down to 2.0 nm [58]. The electron beam path is indicated in Fig. 2.1 and an overview of the most important optical components is given in Fig. 2.2.
The electrons are emitted from a Schottky field emitter which produces a highly coherent electron beam with low energy dispersion. Then, the electrons are accelerated to 20 keV, travel through the illumination column and are deflected by the first sector field. Before they hit the sample at normal incidence (or under a small angle for dark-field LEEM as diescribed in Section 2.1.3), they are decelerated to only a few eV. This rather low interaction energy allows surface-sensitive measurements [13] and provides the opportunity to prevent considerable electron beam damage in sensitive materials like organic molecules as discussed in section 2.1.4. The interaction energy can be set by the start voltage U_{start} which differs only by a small offset from the actual electron energy. This energy strongly influences the contrast of the image as discussed in the next section. A large portion of the electrons is reflected by or diffracted from the sample. The electrons are re-accelerated to the objective lens, are deflected into the intermediate optics by the first sector field and reach through the second sector field the mirror column where they are reflected. The tetrode mirror can improve the lateral resolution to 2.0 nm by reducing the chromatic and spherical aberrations of the objective lens [58]. Then, the electrons pass the imaging column and the hemispherical energy analyser with its energy slit (ES). The latter has an energy resolution of less than

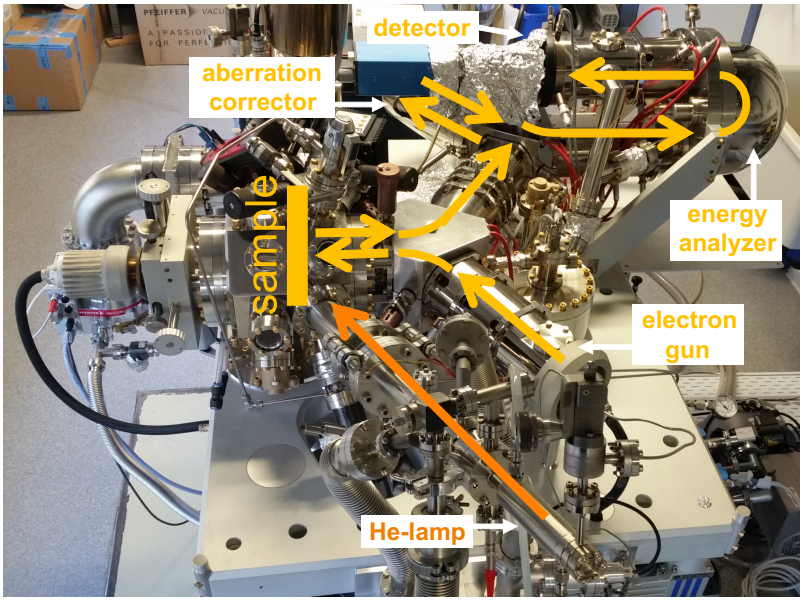

Figure 2.1: Photo of the LEEM instrument: The electron beam path is indicated with yellow arrows. The electrons are emitted from the electron gun, interact with the sample, travel through some optics including aberration corrector and energy analyser and reach the detector. Additionally, the instrument is equipped with a focused He-lamp to illuminate the sample (orange arrow) and emit photoelectrons for PEEM and ARPES measurements.

150 meV. This enables spectroscopic PEEM, ARPES and LEED measurements free from inelastic scattered electrons as discussed below. Finally, the electrons reach the microchannel plate (MCP) detector through the projector column.
During the whole electron beam path, the spatial and momentum information of the electrons are maintained which allows to measure a spatially resolved image of the surface in a single shot without the need to scan over the surface like in STM or SEM. Image and back-focal planes are present at different points in the electron beam path. The image at the detector is affected differently when apertures are inserted in an image or a back-focal plane. The illumination aperture (IA) located in an image plane within the incident beam path of the first sector field enables to illuminate only a small part of the sample with electrons which is very useful for LEED measurements. In a similar way, the selected-area aperture (SA), which is also located in the first sector field but in the excident beam path, is used to choose only electrons which are reflected, diffracted or, in the case of PEEM and ARPES, emitted from a selected area. The contrast aperture (CA) located in the back-focal plane within the field lens (FL) can be applied to cut off off-axis electrons which might be generated by spherical aberration or to obtain an image only of electrons emitted from the sample under a specific angle which is important for dark-field LEEM (see section 2.1.3).

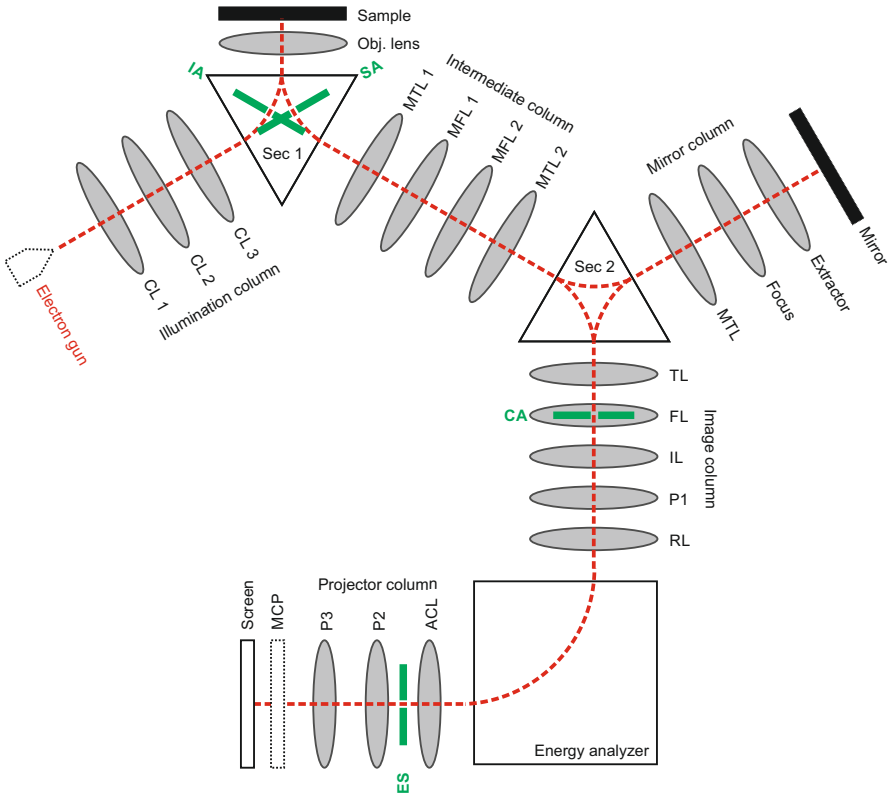

Figure 2.2: Scheme of the most important optical components of the LEEM instrument. (i) Illumination column: electron gun, condensor lens 1-3 (CL 1-3). (ii) First sector field (Sec 1). (iii) Objective lens and sample. (iv) Intermediate column: mirror field lenses and mirror transfer lenses 1 and 2 (MTL1, MFL1, MFL2, MTL2). (v) Second sector field (Sec 2). (vi) Mirror column: mirror transfer lens (MTL), focus, extractor and mirror. (vii) Image column: transfer lens (TL), field lens (FL), illumination lens (IL), projective lens (P1) and retardation lens (RL) (viii) Energy analyser. (ix) Projector column: acceleration lens (ACL), projective lens 2 and 3 (P2 and P3), microchannel plates (MCP) and screen (x) Apertures (green): illumination aperture (IA), selected-area aperture (SA), contrast aperture (CA) and energy slit (ES).

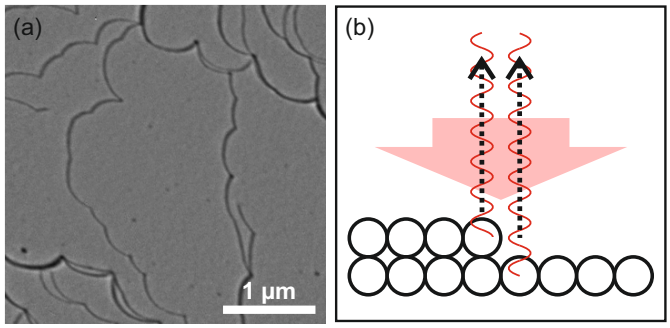

Figure 2.3: Phase contrast in BF-LEEM: (a) Clean Cu(001) surface in the slight underfocus at $U_{\text{start}} = 2\,\text{V}$. The dark, slightly curved lines correspond to step edges. (b) Simplified explanation of the phase contrast at step edges. The electrons reflected from the upper and lower terraces interfere destructively with each other leading to a dark contrast close to the step edge as shown in (a).

2.1.1 Bright-field microscopy

In LEEM, electrons of rather low energies (less than 100 eV) are used for image formation. The interaction mechanisms of low-energy electrons with matter differ strongly from electrons with higher energies. Especially, the dominance of forward scattering decreases with decreasing electron energy while elastic backscattering becomes more important. This elastic backscattering is used in LEEM and depends strongly but not monotonically on the electron energy and the atomic number Z of the scatterer. In the case of solids with periodic structures, the geometric and electronic structure influences this reflectivity additionally. For example, if the electron energy corresponds to a band gap of the material, the electrons are (nearly) totally reflected since no allowed states are present in the bulk. Nevertheless, the reflected intensity is always lower than the incoming intensity because of energy loss mechanisms, surface states or scattering at defects or phonons. A more detailed description of the interactions of slow electrons with matter is given in [13] and [4].
In Bright-Field LEEM (BF-LEEM), the specularly reflected electrons are used for image formation and contrast is produced by local differences in the intensity of the (00)-spot on the sample surface for example caused by different materials. In other cases, local differences in the diffraction conditions can generate a sufficient contrast at certain electron energies [13]. These local differences can be generated by different surface structures [11, 12, 143, 166] or by surface strain as in the case of graphene on Ir(111) [115, 140].

The phase contrast generates a dark contrast at atomic step edges as in the case of the Cu(001) surface depicted in Fig. 2.3 (a). The dark, slightly curved lines correspond to step edges. A simplified explanation is given in Fig. 2.3 (b). The phase shift between the electron waves reflected from the upper and lower terrace leads to destructive interference between these electron waves close to the position of the step edge. A more accurate explanation is given in [4, 27]. There, an analytic wave optical model based on the Fresnel equations is applied which is able to explain the energy- and focus-dependent appearance of step edges and

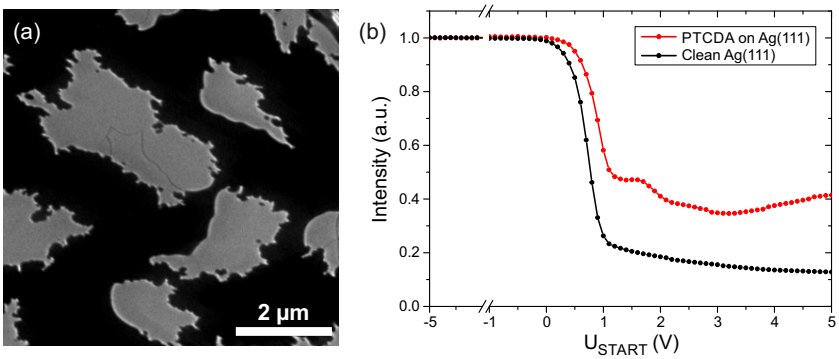

Figure 2.4: Contrast in BF-LEEM of PTCDA on Ag(111): (a) PTCDA islands (bright contrast) on Ag(111) (dark contrast) in the focus at $U_{\text{start}} = 2\,\text{V}$. (b) LEEM-IV curves of the clean Ag(111) substrate and a PTCDA island on Ag(111).

to identify the lower and upper terrace of a step edge (step sense).
Additionally, the topographic and the quantum size contrast should be mentioned. The topographic contrast occurs at hillocks, three-dimensional crystals and depressions on an otherwise flat surface where local field distortions influences the electron trajectory [13]. The quantum size contrast is important in layered systems where (depending on energy and layer thickness) destructive or constructive interference of electron waves reflected at the different layers effects the measured BF-intensity [11, 28, 79, 103, 114].

To find the electron energy with the best contrast experimentally, LEEM-IV curves are taken as depicted in Fig. 2.4 (b) for PTCDA islands on a Ag(111) surface. Here, the normalized intensities of the silver surface and a PTCDA island on Ag(111) are plotted depending on start voltage. For negative start voltages, the electrons are reflected before they even reach the sample and are not able to interact with it. Consequently, the intensity is constant and maximal. With increasing start voltage, i.e., increasing electron energy, the electrons are able to overcome the work function of the sample and interact with it. At this point, the intensity decreases significantly. Since the work function of PTCDA on Ag(111) is slightly larger than the one of the clean Ag(111) surface, this abrupt decrease in intensity occurs for PTCDA at higher start voltages than for Ag(111). For start voltages between 0 V and 5 V, the PTCDA islands exhibit a higher reflectivity than the silver substrate. Thus, bright PTCDA islands on a dark silver crystal can be seen in Fig. 2.4 (a) for a start voltage of 2 V. An even better contrast is achievable at higher start voltages like 5 V; however, beam damage might be a problem in these cases as discussed in section 2.1.4.
A much more sophisticated analysis of LEEM-IV curves has been developed by Flege et al. [46, 47].

2.1.2 Low-energy electron diffraction

LEEM can be easily combined with Low-Energy Electron Diffraction (LEED) since the diffraction pattern appears in the back-focal plane of the objective lens.

The LEED pattern is visible when the lenses of the image column are tuned to image a diffraction plane onto the detector instead of an image plane.
Electron diffraction can be explained by the Ewald's construction in reciprocal space (Fig. 2.5 (a)). The Ewald's sphere radius is given by the length of the wave vector of the incident electrons k_0 which, in turn, depends on the electron energy. Due to the short probing depth of the low-energy electrons, the diffraction can be treated as a quasi two-dimensional problem and the reciprocal lattice can be described with diffraction rods which are oriented perpendicularly to the surface (dashed lines). Since the problem is only approximately two-dimensional, the intensity along the rods is modulated. The arrangement of the intersection points of the rods with the surface plane depends on the lateral lattice of the sample. Constructive interference occurs at all points where the Ewald's sphere intersects with a diffraction rod since there the in-plane component of the momentum transfer $\mathbf{q}^{\parallel}$ equals a translation vector $\mathbf{g}$ of the two-dimensional reciprocal lattice. For the case in Fig. 2.5 (a), the corresponding vectors are indicated in red and green. As an example, a LEED measurement of NTCDA on Cu(001) is depicted in Fig. 2.5 (b). [75, 87, 101, 174]
In contrast to conventional LEED measurements, the LEED spots do not move significantly in a LEEM instrument when the electron energy is changed. Due to the high acceleration the electrons undergo between sample and objective lens, the change in kinetic energy of a few eV is neglectable. This simplifies the evaluation of LEED-IV curves significantly and gives the opportunity to average LEED measurements over a larger energy range to enhance the visibility of all LEED spots. The number of diffraction spots is only limited by the size of the Ewald's sphere, and not by the angular transmission of the objective lens (indicated in blue) since the microscope potential (20 keV) is very high in comparison to the applied start voltages (few eV) resulting in an acceptance-angle of almost 180°. Additionally, the image is not partly shadowed by the electron gun and by using the energy analyser inelastically scattered electrons can be cut off by an energy slit. [13]
Another difference to conventional LEED is the possibility to illuminate only a small area of the sample with electrons and to investigate its reciprocal structure.

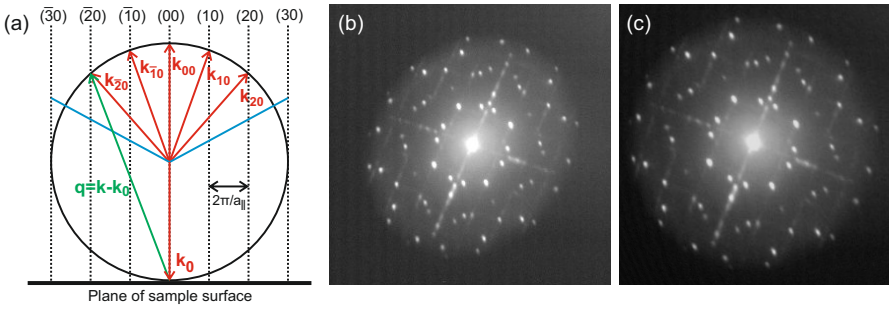

Figure 2.5: Low-Energy Electron Diffraction (LEED): (a) Ewald's sphere construction for a 2D problem (see text for more details). (b) LEED pattern of a monolayer film of NTCDA on Cu(001) at $U_{\text{start}} = 20\,\text{V}$. (c) The same pattern as in (b) after distortion correction by the software LEEDcal.

For this purpose, an aperture (IA) is positioned in the illuminating beam at the position of an image plane within the first sector field (Fig. 2.2). These LEED measurements from areas of only a few µm^2 are called μLEED. They allow for example the determination of the geometric structure of individual islands or to disentangle several different crystalline structures which would overlap in a conventional LEED as in the case of various mixed structures of PTCDA and CuPc on Ag(111) [66]. For all LEED measurements in this thesis, areas of 18 µm^2 and less were chosen.
Additionally, all LEED images (and ARPES measurements) are corrected using the software LEEDcal [59] to compensate for distortions due to lens aberrations and misalignment. This software calculates the image distortions from a reference measurement of a known LEED structure and undistorts the actual LEED measurement with this information. This has been done in Fig. 2.5 (c) for the measurement in Fig. 2.5 (b). The known structures of Cu(111), PTCDA on Ag(111) or NTCDA on Cu(001) are used for calibrating the distortion correction in this thesis.

2.1.3 Dark-field microscopy

In Dark-Field LEEM (DF-LEEM), the non-specular diffracted beams are used to generate contrast in a real space image for example between various rotational and mirror domains of the same molecular structure. For this purpose, the contrast aperture (CA) is introduced into a focal plane (Fig. 2.2) so that only the electrons emitted under a specific angle can pass the aperture and contribute to the image projected onto the detector. This angle can be changed either by adjusting the position of the contrast aperture or by changing the incidence angle of the electron beam on the sample. The second procedure is chosen to avoid additional aberrations due to a beam which is not travelling on the optical axis. Additionally, it is much more reproducible than the first procedure and enables to assign a certain LEED spot to the corresponding DF-LEEM image. [4, 11, 13]
As an example, the DF-LEEM measurements of a closed monolayer PTCDA on Ag(111) are depicted in Fig. 2.6. On this substrate, six rotational and mirror domains of the same PTCDA structure occur which are not distinguishable in BF-LEEM. The six LEED spots, which were chosen for DF-LEEM and correspond to the six different domains, are marked in (a). The corresponding DF-LEEM measurements are shown in (c) and are summarised in the false-colour image in (b).

2.1.4 Beam damage

In electron microscopy, electron beam damage of the sample is always an important concern. The extremely low electron energies of only a few eV used in LEEM let assume that the induced damage is minimal. However, the influence of the beam is still observed in some cases, it depends strongly on the chosen start voltage and the beam can effect the measurement in different ways.
In most cases, beam damage occurs at higher electron energies ($U_{\text{start}} > 10\,\text{V}$) which are necessary for LEED and DF-LEEM measurements. Here, a decreasing

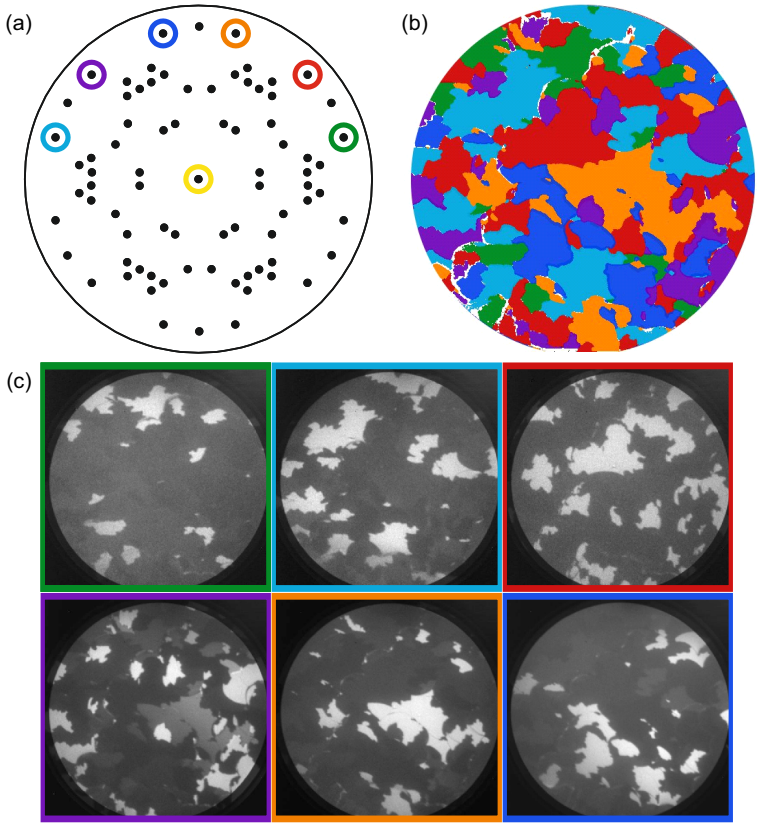

Figure 2.6: DF-LEEM measurements of a closed monolayer PTCDA on Ag(111): (a) Simulated LEED pattern; the (00)-spot (yellow) and the six LEED spots which are chosen for DF-LEEM measurements are marked. (b) False colour image of the six PTCDA domains in real space. (c) Dark-field LEEM images of the six PTCDA domains which contribute to the false colour image in (b) (FOV 10 µm, $U_{\text{start}} = 10\,\text{V}$).

intensity of the LEED spots or the DF-LEEM images with illumination time can be observed for some samples. In Fig. 2.7 (a), a BF-LEEM image of a monolayer NTCDA on Cu(001) is depicted which is taken after a LEED measurement where start voltages of $U_{\text{start}} \leq 15\,\text{V}$ were applied. The area illuminated with electrons during this LEED measurement was limited by an illumination aperture and can be recognized in the BF-LEEM image because of the significantly reduced intensity (highlighted in red). Since the influence of the electrons on different surface structures or parts of an island can be different, the contrast can be influenced as well [139].
Additionally, dynamical processes such as nucleation of islands or Ostwald ripening can be influenced. An influence on the nucleation process has been observed in the case of CuPc on Cu(001) where the island density in the regime of electron illumination was significantly increased in comparison to the rest of the sample

[66]. In the case of PTCDA on Cu(001), Ostwald ripening, i.e. the transition from many small islands to a few larger islands, is usually observed when the sample is heated slightly after the deposition process at room temperature. For $U_{\text{start}} \leq 2\,\text{V}$, no influence of any electron beam illumination was observed on this ripening. However, a LEEM-IV measurement ($U_{\text{start}} \leq 5\,\text{V}$) after the deposition and before the heating changed the result. On the area which was illuminated with electrons, no change could be observed despite the increased temperature. Therefore, the observed sample area was changed. As depicted in Fig. 2.7 (b), above the edge of the former electron beam (indicated in red) significantly larger islands are observed. Here, Ostwald ripening has taken place.
In this thesis, several precautions were taken to prevent an influence of beam damage on the results. For all LEEM measurements, start voltages below 2 V were used which proved not to damage the organic films or hBN layers prepared in this thesis significantly. After LEED, LEEM-IV and DF-LEEM measurements for which higher start voltages are necessary, it was always checked if any indications of beam damage could be observed. When changes could be recognized, the sample position was changed or the experiment was repeated.

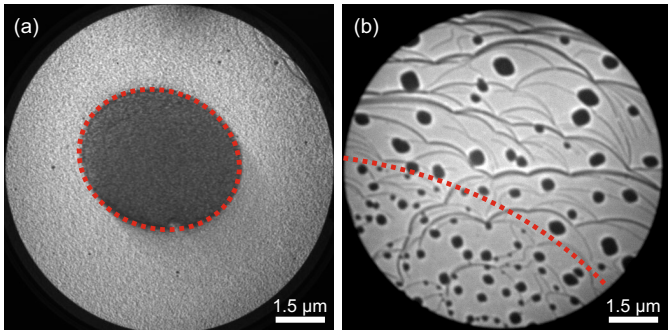

Figure 2.7: Beam damage: (a) Monolayer NTCDA on Cu(001) in slight underfocus at $U_{\text{start}} = 2.4\,\text{V}$ after a LEED measurement at $U_{\text{start}} = 7.5\,\text{V}$. The area used for the LEED measurements was limited by the illumination aperture, is indicated in red and appears much darker than the rest of the sample. (b) PTCDA islands (dark contrast) on Cu(001) in underfocus at $U_{\text{start}} = 2\,\text{V}$. After deposition, a LEEM-IV measurement ($U_{\text{start}} \leq 10\,\text{V}$) was performed on the area below the red line. Then, the sample was slightly heated to observe Ostwald ripening. It can clearly be seen that Ostwald ripening took place only at the upper part of the sample which was not illuminated by the beam in the LEEM-IV experiment.

2.1.5 Photoemission electron and momentum microscopy

In Photoemission Electron Microscopy (PEEM) and momentum microscopy, the sample is illuminated with photons instead of electrons. When the photon energy is high enough, photo-electrons are emitted from the sample which travel through the rest of the microscope as in the case of an electron source. They

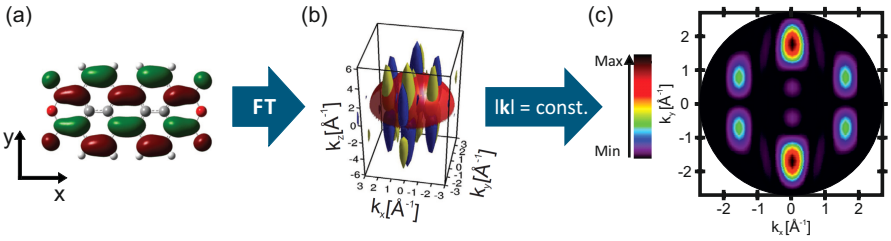

Figure 2.8: Calculation of the angular-resolved photoemission signal of the LUMO of PTCDA: (a) Wave function of the LUMO of a free PTCDA molecule. (b) Fourier transform of (a). (c) The angular intensity distribution results from the evaluation of the absolute square of (b) on a hemispherical sphere with the radius $k = \sqrt{(2m/\hbar^2)E_{kin}}$. (Calculations done by Daniel Lüftner, University Graz)

are accelerated between sample and objective lens by 20 keV (reduced by the start voltage), pass the two sector fields, the aberration corrector and the energy analyser before they reach the MCP detector. In the PEEM mode, the same lens settings are used as in the LEEM mode and the photo-electrons are used to produce a real-space image of the sample. For momentum microscopy, the settings for LEED are applied to measure the angular distribution of the emitted photo-electrons. In contrast to conventional Angular-Resolved Photo-Electron Spectroscopy (ARPES) measurements, the electron distribution in the $k_x k_y$-plane is measured in one shot without the need to rotate the sample or to scan in k-space. In PEEM and momentum microscopy mode, energy resolved measurements can be achieved in combination with the hemispherical electron analyser and an appropriate energy slit (ES). When the energy slit is introduced into the electron beam, only electrons with a certain kinetic energy can pass it. The adjustment of the start voltage U_{start} gives the opportunity to scan in kinetic energy. The absolute binding energies are calibrated with the position of the Fermi edge.

In this thesis, two illumination sources in the UV range are used. The Hg-lamp manufactured by LOT-Oriel group Europe is mainly applied for the alignment procedure in the PEEM mode. The FOCUS HIS 14 High Density VUV Source with a spot size of 300 µm and a photon energy of 21.2 eV (HeI radiation) is mainly used for momentum microscopy which is explained in the following in more detail.

The kinetic energy of the electrons E_{kin} emitted from the sample depends on the photon energy $\hbar\omega$, the work function ϕ_{A} of the sample and the binding energy E_{B} of the state from which the electron is emitted.

$$E_{\text{kin}} = \hbar\omega - \phi_{\text{A}} - E_{\text{B}} \tag{2.1}$$

The intensity of the photo-electrons is determined by Fermi's Golden rule.

The approximation of a plane wave as simplest approximation for the final state of the photoemission process simplifies the calculation of the angular intensity distribution $I(\theta, \varphi, E_{\text{kin}})$ significantly. Then, it is mainly given by the absolute squared Fourier transform of the initial wave-function Ψ_{i}. [123]

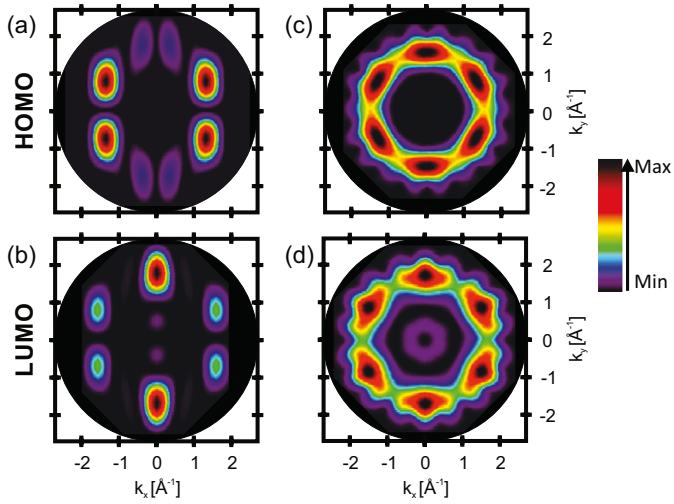

Figure 2.9: Calculation (done by Daniel Lüftner, University Graz) of the CBE maps of the HOMO and LUMO of the free PTCDA molecule ((a)+(b)) and PTCDA on Ag(111) ((c)+(d)).

$$I(\theta, \varphi, E_{\text{kin}}) \sim |\mathbf{A} \cdot \mathbf{k}|^2 \cdot |\widehat{\Psi}_i(\mathbf{k}, E_{\text{kin}})|^2 \tag{2.2}$$

The factor $|\mathbf{A}\cdot\mathbf{k}|^2$ scales the intensity of the pure orbital emission pattern according to the angle between the direction of the photo-electrons $\mathbf{k}$ and the incoming radiation given by the vector potential of the exciting electromagnetic wave $\mathbf{A}$. [123]

Although the plane wave approximation is a very crude approximation that cannot generally be used for analysing ARPES data, it has been applied very successfully in specific cases. Examples are the successful assignment [123], the orbital tomography deconvolution [124, 156, 160] and the reconstruction of the wavefunction of molecular orbitals [100, 185].

For molecular adsorbates, the initial state Ψ_i corresponds to the wave function of the molecular orbital. The angular-resolved photoemission signal can be calculated in three steps as illustrated in Fig. 2.8 for the LUMO of PTCDA. The wave function of the molecular orbital is calculated with DFT for a free molecule in the gas phase (a). Subsequently, the wave function is Fourier transformed (b). The absolute square of this result has to be evaluated on a hemispherical sphere with the radius $k = \sqrt{(2m/\hbar^2)E_{\text{kin}}}$. This leads to the two-dimensional intensity distribution as a function of the parallel momentum components k_x and k_y and is called constant binding energy (CBE) map (c). The result is characteristic for each molecular orbital thus it enables the identification of the emitting molecular orbital. [123]

However for many molecular adsorbates on metal substrates, different orientations of molecules on the surface contribute to the angular-resolved photoemission signal as depicted in Fig. 2.9 (c) and (d) for PTCDA on Ag(111) where twelve molecules with different orientations contribute to the maps. For comparison, the CBE maps for the HOMO and LUMO of a free PTCDA molecule are depicted

in (a) and (b), respectively. [123, 156]
For a more quantitative analysis, the contributions of specific molecular orbitals to the measured photo-electron yield can be separated from each other by orbital tomography which was introduced by Puschnig et al. [124]. In this procedure at every measured binding energy E_B, a two-dimensional fit of all contributing CBE maps $\Phi_i(k_x, k_y)$ to the measured intensity distribution is performed. Additionally, the signal of the substrate $I_{sub}(k_x, k_y, E_B)$ and a constant background $c(E_B)$ is considered.

$$F(k_x, k_y, E_B) = \sum a_i(E_B)\Phi_i(k_x, k_y) + b(E_B)I_{sub}(k_x, k_y, E_B) + c(E_B) \qquad (2.3)$$

The fitting parameters a_i are interpreted as density of states projected on the corresponding molecular orbital (PDOS).
This method allows to determine the PDOS for all orbitals which are relevant in the (binding) energy range of interest. Two examples that are related to the work presented here are the distinction between the two LUMO positions of the two PTCDA molecules in the unit cell on Ag(111) [156] and the determination of the different charge transfers into the two molecules PTCDA and CuPc forming mixed ordered structures on Ag(111) [160].

2.1.6 Image processing

In this thesis, the open source program Image J [135] and the related software Fiji [130] is applied for image processing. It is used for example to average LEEM or PEEM images, read out intensity values of certain areas or adjust the contrast settings. Three important processing steps are described in more detail in the following.

Flat field correction

The sensitivity of the micro-channel plate (MCP) detector, i.e., the amplification of the electron signal, is not homogeneous in the complete detector area. However, the area dependency is constant over several month, as long as the system is not vented and the MCP is not illuminated with too high electron intensities, but it changes with the applied settings on the detector strongly. This inhomogeneity can be corrected by using a so called mirror image for calibration [66, 139]. At a start voltage of $-5\,V$, the electrons are not able to interact with the sample so that all electrons are reflected from the surface leading to an image which is independent from the surface morphology and exhibits a constant intensity distribution except for the inhomogeneity caused by the MCP. Calibration of the image plate is performed by dividing the images of interest by the mirror mode image.

Threshold method

The threshold method is used to determine island sizes. After a flat field correction is applied, the intensity on the islands is nearly constant and differs significantly from the also nearly constant intensity on the substrate if an appropriate start voltage was chosen. Then, a threshold can be set in Fiji which creates a

binary image so that all pixels with a value higher than the chosen threshold appear dark and the once with a lower value white. Artefacts from step edges and other defects can be corrected manually. Afterwards, this new image can be analysed further to determine for example the island size distributions.

False colour images

In the DF-LEEM measurements discussed in this thesis, up to six different domains can be distinguished in the case of organic monolayers and even more in the case of hBN on Cu(111). Often, they are depicted as false colour images which are produced by two different methods.
In Fiji [130], the different DF-LEEM images can be merged in a false colour "composite" image by replacing the gray values of each images with the corresponding colour value. An example is depicted in Fig. 5.14 (f) where each colour represents one DF-LEEM image. The advantage of this method is that the intensity information of the single measurements is still encoded in the intensity of the corresponding colour.
For the second method, the domains are identified using the threshold method. Then, the binary images are overlapped manually. An example is depicted in Fig. 2.6 (b). This method is applied when hints of a second domain occur in one DF-LEEM image (as observed for the image in Fig. 2.6 (c) marked in purple).

2.2 Complementary techniques

2.2.1 Scanning tunnelling microscopy

Scanning Tunneling Microscopy (STM) is applied as complementary technique to determine the molecular structure and orientation of the NTCDA molecules on Cu(001) and to support the model which evolved from the LEEM data.
Since STM is a well-known technique, an introduction into the theoretical and technical background is not given here. But a detailed introduction can be found in [180].
In this thesis, a commercial Omicron Variable Temperature STM is used which was build in 1998. The chamber is equipped with a sputter gun, an NTCDA evaporator and a quadrupole mass spectrometers (QMS) for the preparation of NTCDA monolayers on the Cu(001) crystal. A LEED instrument is also available giving the opportunity to compare the preparations in the STM with those done in the LEEM instrument. All STM images shown in this thesis were done by Markus Franke [50]. The program WSxM is applied for the analysis of the STM images [74].

2.2.2 X-ray standing wave method

Normal Incidence X-ray Standing Wave (NIXSW) is a method to determine the adsorption heights of adsorbates on crystalline substrates with extremely high precision ($\Delta z < 0.04\,\text{Å}$). In many previous studies, it was successfully applied to investigate the adsorption of organic molecules on metal substrates [56, 68, 108, 154, 156, 160] and of two-dimensional systems like graphene [147, 148] and hBN [21]. In the following, a brief introduction into the basic principles is given. More detailed descriptions can be found in the descriptions of Zegenhagen [196–198] and Woodruff [191, 192] or in the dissertations of Mercurio [108] and Stadtmüller [157].
In an NIXSW experiment, a crystal is illuminated with a monochromized X-ray beam in normal incidence to the Bragg planes of the selected reflection. Photon energies E are chosen which fulfill the Bragg condition of this crystal plane. Therefore, a diffracted beam is produced which is coherent with the incoming beam. The interference of these beams generates a standing wave field with the local photon intensity I_{SW} depending on E:

$$I_{\text{SW}}(E,z) = 1 + R(E) + 2\sqrt{R(E)}cos\left(\nu(E) - \frac{2\pi z}{d_{hkl}}\right)$$

which is normalized to the incoming beam intensity. z is the vertical coordinate, d_{hkl} the distance between the chosen Bragg planes, R the reflectivity and ν the phase difference between the incoming and the reflected beam given by $\frac{E_{\text{H}}}{E_0} = \sqrt{R} \cdot exp(i\nu)$.
According to the theory of dynamic diffraction, the diffraction peak close to the Bragg condition even of an ideal crystal has a certain width, the Darwin width. This means that the energy of the incoming photon beam E can be changed slightly while the reflectivity R has a value different from zero (a diffracted beam still exists). Besides the reflectivity $R(E)$, the phase between incoming and reflected wave $\nu(E)$ is varied with E which leads to a shift of the standing wave

field inside the crystal perpendicular to the Bragg planes.
Since the photon absorption, and thus, for example, the photoelectron emission of an atom on the surface, depends on the local photon intensity, the XSW-field can be used to determine the position of the atom by analysing the XPS signal for various photon energies close to the Bragg condition. The chemical sensitivity of the XPS signal allows to distinguish the heights of chemically different species for example of the anhydride and the carboxylic oxygen in PTCDA [68].
Nevertheless, a lot of atoms of the same species contribute to the XPS signal with slightly different vertical heights because of disorder. Thus, the vertical normalized height distribution $f(z)$ has to be introduced.

$$I_{\mathrm{SW}} = 1 + R(E) + 2\sqrt{R(E)} \int_0^{d^{\mathrm{H}}} f(z) cos\left(\nu(E) - \frac{2\pi z}{d_{hkl}}\right) dz$$

$$= 1 + R(E) + 2\sqrt{R(E)} F^{\mathrm{H}} cos\left(\nu(E) - 2\pi P^{\mathrm{H}}\right)$$

In the second line, two important parameters are introduced. The coherent position P^{H} corresponds to the averaged vertical position in fractions of the Bragg plane distances above the nearest Bragg plain. The coherent fraction F^{H} is a parameter for the vertical ordering with values between 0 and 1. In most cases, a value of 0 corresponds to a homogeneous distribution of heights (complete disorder) while a coherent fraction of 1 corresponds to a perfectly ordered layer with all atoms of the measured species on the same height.
These two parameters are the central results of each XSW experiment and are plotted in a polar diagram, the so-called Argand diagram. An example is plotted in Fig. 5.4 (d).

2.2.3 Pair potential calculations

In this section, the pair potential approach is discussed briefly which represents a simple theoretical model considering van der Waals and electrostatic interactions to calculate the interaction energy between two or more molecules and to find the most favourable adsorption configurations for molecules. The parametrization and the implementation of this approach is based on the work of Kröger et al. [91]. It has been successfully applied on molecular systems on weakly interacting surfaces [95].

The pair potential Φ corresponding to the interaction energy between two molecules A and B is defined as:

$$\Phi(\mathbf{r}) = \sum_i \sum_j \left(\phi_{ij}^{\mathrm{vdW}}(r_{ij}) + \phi_{ij}^{\mathrm{ES}}(r_{ij})\right).$$

Here, the interaction energies of each atom i of molecule A and of each atom j of molecule B are summed up considering the electrostatic potential ϕ_{ij}^{ES} and the van der Waals potential ϕ_{ij}^{vdW}. Both depend only on the distance r_{ij} between the atoms. The electrostatic potential ϕ_{ij}^{ES} is given by the Coulomb potential:

$$\phi_{ij}^{\mathrm{ES}}(r_{ij}) = \frac{Z_i Z_j}{4\pi\epsilon_0 r_{ij}}$$

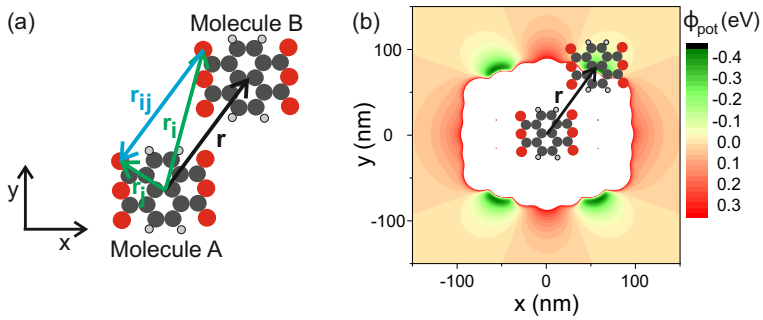

Figure 2.10: Pair potential approach. (a) The relative displacement vectors **r** between the center of masses of the molecules (black) and the fixed arrangement of atoms within the molecule NTCDA determine the vectors $\mathbf{r_i}$, $\mathbf{r_j}$ and $\mathbf{r_{ij}}$ (green and blue). (b) Pair potential map of two parallelly oriented NTCDA molecules as a function of the lateral displacement **r**. Most favourable adsorption sites for molecules are usually reflected in deep minima in the pair potential.

The partial charges of the atoms within the molecule Z_i and Z_j were calculated by natural bond orbitals population analysis with the Gaussian03 package. More details can be found in [95].
The van der Waals potential includes the Pauli repulsion described by an exponential function and the attractive London force which is proportional to r_{ij}^{-6}:

$$\phi_{ij}^{\mathrm{vdW}}(r_{ij}) = a_{ij}e^{-b_{ij}r_{ij}} - \frac{c_{ij}}{r_{ij}^6}$$

The element parameters a_{ij}, b_{ij} and c_{ij} are called specific non-bonding parameters. For symmetric pairs (atom i and j are of the same species), values for b_{ij} and c_{ij} can be found in literature [48, 145, 149] and a_{ij} is optimized in order to find the minimum energy at a distance corresponding to the van der Waals radius of the specific atom reported by [18]. In the case of asymmetric pairs (atom i and j are not of the same species), the geometric mean of the symmetric pairs is applied for a_{ij}, b_{ij} and c_{ij}.
The molecules are assumed to be rigid objects with the atomic distances of the gas phase geometry calculated by DFT (Gaussian03). Distortions upon adsorption are neglected. Consequently, the relative displacement vectors **r** between the center of masses of the molecules (black) and the fixed arrangement of atoms within the molecule NTCDA determine the vectors $\mathbf{r_i}$, $\mathbf{r_j}$ and $\mathbf{r_{ij}}$ (Fig. 2.10 (a)).
In this work, the pair potentials are depicted in two-dimensional maps in which the energy potential for various positions in the (xy)-plane of a molecule is colour coded as depicted in Fig. 2.10 (b). Green corresponds to a negative pair potential and thus attraction while red describes positive pair potentials and repulsion. Most favourable adsorption sites for molecules are usually reflected in deep minima in the pair potential [95].

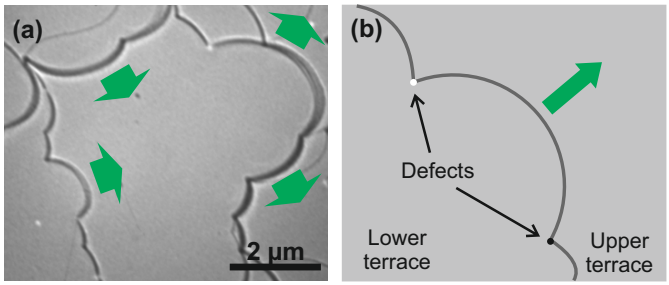

Figure 2.11: Step edge movement (indicated with green arrows). (a) LEEM image of Cu(001) in underfocus at $U_{\text{start}} = 2\,\text{V}$. (b) Sketch of the movement and bending of step edges during annealing.

2.3 Sample preparation

The ultra-high vacuum (UHV) system of the LEEM instrument consists of three chambers: the column, where most of the optical components are located in, and the main and the preparation chamber where the sample preparation takes place. Before each experiment, the copper crystals are cleaned by several sputtering and annealing cycles in the preparation chamber. For sputtering, a 3:2 mixture of argon and hydrogen is used which has proven to exhibit better results regarding terrace sizes on Cu(001) than pure argon [66]. After sputtering, the Cu(001) crystal is annealed for 10 min and the Cu(111) crystal for 30 min at 900 K. For heating, a tungsten filament is integrated into the sample holder which is constructed to also allow electron bombardment onto the back of the crystal for additional heating power. The final annealing step is performed in the main chamber and is observed with LEEM. Here, even higher annealing temperatures (about 150 K higher) and longer annealing times (up to 1 h) are applied to reach larger terrace sizes.

At these temperatures, the evaporation of Cu atoms from the step edges can be observed leading to the movement of step edges as depicted in Fig. 2.11. The movement is indicated with green arrows and gives the opportunity to identify on which side of the step edge the upper and lower terrace is located (step sense). When a step edge approaches a defect on its way over the surface, the step edge is temporarilly pinned at this position leading to the characteristic bending of the step edges so that the upper terrace is located on the concave side of a step edge. The curvature does not change significantly during the cooling of the crystal back to room temperature; thus, the step sense can be determined without watching the annealing process at that particular area. Another oppertunity to determine the step sense is described in [27].

The annealing is stopped when the sizes of the Cu terraces are large enough for the planed experiment. Then, the crystal is cooled down to the temperature used for the preparation of organic or hBN layers. In the case of organic films, the substrate has temperatures close to room temperature (300 K to 400 K) while it is significantly higher (900 K to 1100 K) during hBN preparation.

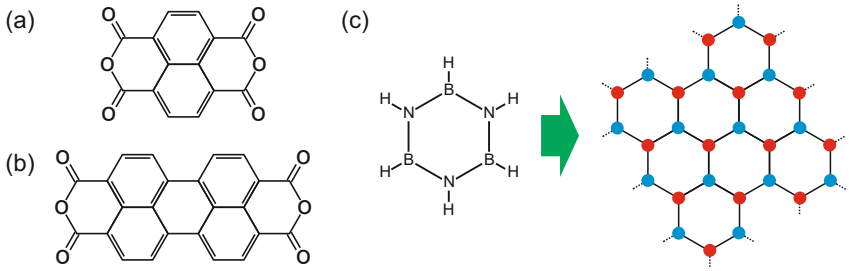

Figure 2.12: Chemical structural models of (a) NTCDA (b) PTCDA and (c) borazine which is used to prepare hBN.

2.3.1 Preparation of molecular layers

All organic films are prepared under UHV conditions with a base pressure better than 5×10^{-10} Torr in the main chamber during observation with LEEM, DF-LEEM or LEED. The NTCDA and PTCDA molecules, which are depicted in Fig. 2.12 (a) and (b), respectively, were purified before hand by at least three sublimation cycles and are evaporated onto the sample with custom-made Knudsen cell evaporators. Before each experiment, the evaporators are preheated for at least one hour to guarantee a constant deposition rate. A shutter in front of the evaporator prevents molecules to reach the sample during the preheating and enables an accurately defined start and end point of the deposition. The deposition rates are calibrated by measuring the time needed to deposit a complete monolayer.

2.3.2 hBN-prepartion

The hexagonal Boron Nitride (hBN) monolayers are prepared in the main chamber during observation with LEEM. In contrast to the deposition of organic molecules, the hBN is fabricated from the gas borazine ($(BH)_3(NH)_3$) directly on the hot Cu(111) crystal by chemical vapour deposition (CVD) as depicted in Fig. 2.12 (c). For this purpose, the borazine is dosed via a leak valve into the chamber while the Cu crystal is kept at a temperature of 400 to 1100 K after the last annealing cycle. Typically, pressures between 0.5 and 5×10^{-7} Torr are chosen for preparation which are measured with an ion gauge. The preparation is finished by closing the leak valve and subsequent cooling down to room temperature by less than $1\,\mathrm{K\,s^{-1}}$.
The borazine was purchased from Katchem spol s.r.o, Czech Republic and was under argon atmosphere for transport. It was continuously stored below 0 °C after delivery in order to minimize thermal degradation. The liquid was filled into a small glass tube which was evacuated to about 2×10^{-2} bar before. The argon and hydrogen, a decomposition product which possibly already formed, was pumped away while the borazine was frozen by liquid nitrogen. Then, the borazine was defrosted again. This cleaning procedure was repeated at least five times before the glass tube was connected to the main chamber of the LEEM by a leak valve where it was continuously stored below 0 °C as well.

2.3.3 Sample temperature measurements

For temperature measurement, a tungsten/rhenium (W/Re 95%/5% - W/Re 74%/26%, by weight) alloy thermocouple is spot welded to the sample holder very close to the crystal. Usually, such a set up is expected to yield realistic sample temperature values. However, the situation is more complicated in the LEEM setup since the sample and its holder are biased with approximately 20 kV. Therefore, the read out electronics of the temperature is positioned in a high voltage (HV) rack together with many other electronic devices like power supplies etc., also floating on 20 kV. It was found that with this setup the measured sample temperature depends on the temperature within the HV-rack [173] and, therefore, on the temperature in the room. Since the laboratory is not air conditioned, this is a significant problem which can be solved by an appropriate calibration. In this thesis, the calibration method based on the work of Jonas van Bebber [173] and of Jana Wolters [190] is applied which is described in the following briefly.
Between the temperatures in the room, in the HV rack and measured at the sample by the thermocouple (without any heating or cooling), linear tendencies were found. Under the assumption that the room temperature and the actual sample temperature are equal, a calibration was found which is based on data taken at many different HV rack temperatures. This calibration determines an offset between the measured and the actual sample temperature which depends on the HV rack temperature.
For each experiment in this thesis, the temperature in the HV rack was recorded to determine this offset, in particular, for the temperature dependent measurements. For all experiments, it is assumed that the offset between the measured and the actual sample temperature depends on the temperature in the HV-rack only and not on the actual sample temperature as well.
The calibration has been done for each sample holder separately and was repeated regularly, in particular, when anything was changed with the sample holder (e.g thermocouple, crystal or filament). However, the uncertainty on the actual sample temperature (referring to this calibration) is still between 5 K and 15 K.

Chapter 3

Theoretical background

In this chapter, a brief introduction into nucleation theory is given including the derivations of the most important equations and methods which are applied in chapter 4 for the determination of the critical cluster size, the diffusion barrier and the cohesion energy of PTCDA on Cu(001). Since nucleation theory was developed for the hetero- and homoepitaxial growth of *atomic* layers only, this chapter will not treat the growth of molecules directly. However, it has been shown that the results of nucleation theory are also valid for many molecular systems [25, 66, 129, 155, 165].

3.1 Rate equations

In this section based on the description of Michely and Krug [110], the rate equations are introduced which are necessary for the derivations of some important equations which are applied in this thesis. They describe the different atomistic processes on the surface, like deposition of atoms on the surface, formation of dimers, growths or decay of islands by attachment and detachment of adatoms, in terms of rates. For reasons of simplicity, the case of complete condensation is discussed only where the sticking coefficient, the percentage of atoms which stays on the surface and does not desorb from it after deposition, is 1. This is a good approximation for the most systems investigated in this thesis.
The first rate of interest is the deposition rate R which increases the number of adatoms on the surface n_1 as illustrated in Fig. 3.1. At sufficient substrate

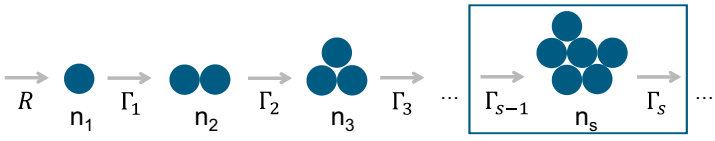

Figure 3.1: After deposition with rate R, the adatoms are able to diffuse over the surface. When an adatom hits another adatom or an already existing cluster of atoms, they can form a dimer or it can be integrated into a cluster. Hence, clusters of various sizes can be formed. n_s describes the density of clusters with s atoms and Γ_s the transition rate from clusters with s atoms to clusters containing $s+1$ atoms.

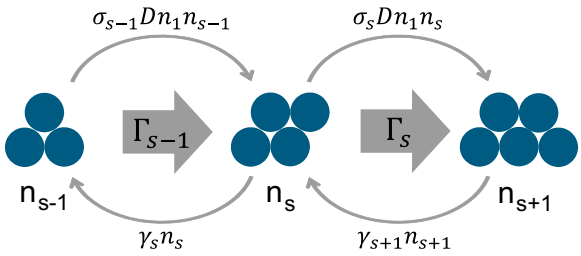

Figure 3.2: The change of the density of clusters with s atoms n_s depends on the transition rates Γ_{s-1} and Γ_s. These rates include the attachment of an atom to a cluster and the detachment of an adatom from a cluster. For more details, see text.

temperatures T, the adatoms are able to diffuse over the surface which is quantified by the diffusion coefficient D. When an adatom hits another adatom, they can form a dimer. This process reduces the number of adatom and increases the number of dimers. Additionally, adatoms can hit already existing clusters of atoms so that clusters of various sizes can be formed. The adatom density n_1 and the density of clusters with s atoms n_s can be described with rate equations. For this purpose, the transition rate of clusters containing s atoms to clusters containing $s+1$ atoms is defined as Γ_s as also depicted in Fig. 3.1. This rate includes the attachment of an atom to a cluster of s atoms and the detachment of an adatom from a cluster containing $s+1$ atoms as depicted in Fig. 3.2. The attachment rate is proportional to the diffusion coefficient D, the adatom density n_1 and the density n_s while the detachment only depends on the density n_{s+1}. The proportionality factors are given by the capture number σ_s and the detachment rate γ_{s+1}, respectively. Therefore, the density of islands with s atoms changes according to

$$\frac{dn_s}{dt} = \Gamma_{s-1} - \Gamma_s \quad \text{with} \quad \Gamma_s = \sigma_s D n_1 n_s - \gamma_{s+1} n_{s+1} \tag{3.1}$$

The adatom density n_1 on the surface increases as atoms are deposited with the rate R. Simultaneously, it decreases when a dimer of two adatoms is formed or when a cluster grows by attachment of an adatom:

$$\frac{dn_1}{dt} = R - 2\Gamma_1 - \sum_{s\geq 2} \Gamma_s \tag{3.2}$$

At a certain size ($s > i$), the clusters are assumed to be stable. Thus, the detachment rate γ_s is zero. The critical cluster size i is defined as the number of atoms in the largest cluster that is not yet stable. Therefore, the stable island density N changes with

$$\frac{dN}{dt} = \sum_{s=i+1}^{\infty} \frac{dn_s}{dt} = \Gamma_i - \Gamma_{i+1} + \Gamma_{i+1} - \Gamma_{i+2} + \Gamma_{i+2} - \Gamma_{i+3} + ... = \sigma_i D n_1 n_i \tag{3.3}$$

Under the assumption of thermal equilibrium among the unstable clusters, the transition rates for the unstable clusters Γ_s ($1 \leq s \leq i-1$) are zero. Then, the

change of the adatom density n_1 is given by

$$\frac{dn_1}{dt} = R - \sigma_i D n_1 n_i - \overline{\sigma} D n_1 N \quad \text{with} \quad \overline{\sigma} = N^{-1} \sum_{s=i+1}^{\infty} n_s \sigma_s \tag{3.4}$$

Additionally, the detailed balance relation [183] is fulfilled in thermal equilibrium:

$$\Omega n_s \approx (\Omega n_1)^s e^{\frac{E_s}{k_B T}} \quad (2 \leq s \leq i) \tag{3.5}$$

Here, Ω is the area of an adsorption site and E_s is the total binding energy of a cluster of s atoms.
With the equations 3.3, 3.4 and 3.5, the island densities and the adatom densities can be calculated. The solution displays two temporal regimes. In the first regime, stable clusters are widely spaced and new clusters nucleate in between. In the second regime, the nucleation rate is zero since the existing island edges are the most probable places for the adatoms to be attached. Thus, the number of islands is constant and the islands only grow in size. This regime is called steady state regime and is discussed in the following section in more detail. For higher coverages, the rate equations are not applicable any more since coalescence of islands becomes important.

3.2 Steady state regime

In the steady state regime, the island density N and the adatom density n_1 are constant. With this assumption and the equations 3.3, 3.4 and 3.5, the islands per adsorption site $\widehat{N}$ is given by

$$\widehat{N} = \Omega N = \left[(i+2)\sigma_i \overline{\sigma}^{-(i+1)} \Theta\right]^{\frac{1}{i+2}} \left(\frac{\Omega^2 R}{D}\right)^{\frac{i}{i+2}} e^{\frac{E_i}{(i+2)k_B T}} \tag{3.6}$$

This equation is the main result of nucleation theory for the case of a 2D system and complete condensation [110]. Two important relations deduced from this equation and applied in chapter 4 are

$$N \sim \left(\frac{R}{D}\right)^{\frac{i}{i+2}} \quad \text{and} \quad N \sim exp\left(\frac{iE_D + E_i}{(i+2)k_B T}\right) \quad \text{with} \quad D = D_0 exp\left(-\frac{E_D}{k_B T}\right). \tag{3.7}$$

These relations make it possible to determine the critical cluster size i, the diffusion barrier E_D and the cohesion energy E_i of a cluster with i atoms experimentally. However, this requires many growth experiments with various deposition rates and at various substrate temperatures.

3.3 Island size distributions

The investigation of the island size distribution in the steady-state regime gives the opportunity to determine the critical cluster size i at a certain temperature with only one growth experiment as long as there is enough statistics (large

number of islands). The following description is based on the work of Amar et al. [5, 6].
The island size distribution, N_s, is the density (i.e. number of islands per site) of islands containing s atoms at the coverage θ. According to the dynamical scaling assumption [38, 39, 179], there is a scaled island size distribution $f_i(s/S)$ which is only determined by the critical cluster size i so that the island size distribution can be written in the general scaling form [6]:

$$f\left(\frac{s}{S}\right) = \frac{N_s S^2}{\theta} \quad \text{for} \quad s \geq 2 \tag{3.8}$$

Here, S is the mean island size and θ the coverage with

$$S = \frac{\sum_{s\geq 2} sN_s(\theta)}{\sum_{s\geq 2} N_s(\theta)} \quad \text{and} \quad \theta = \sum_{s\geq 1} sN_s(\theta). \tag{3.9}$$

In order to determine the critical cluster size i from experimental data, an explicit model for this scaled island size distribution $f_i(s/S)$ is needed. In this thesis, the following ansatz is applied for $f_i(s/S)$ which has been successfully applied for molecular systems [129, 155, 165] and was developed by Amar et al. [5]:

$$f_i(u) = C_i u^i e^{-ia_i u^{\frac{1}{a_i}}} \quad \text{with} \quad u = s/S \tag{3.10}$$

where C_i and a_i are given by the equations

$$(ia_i)^{a_i} = \frac{\Gamma[(i+2)a_i]}{\Gamma[(i+1)a_i]} \quad \text{and} \quad C_i = \frac{(ia_i)^{(i+1)a_i}}{a_i \Gamma[(i+1)a_i]}. \tag{3.11}$$

The values for C_i and a_i can be found in [119].
This model allows to determine the critical cluster size from a measured island size distribution if the dynamical scaling assumption is valid. First, the island sizes in the aggregation regime are measured as described in 2.1.6 and are plotted in a histogram. Then, this measured distribution is normalized according to equation 3.8 and is compared with the theoretical curves $f_i(s/S)$ for various i.

Chapter 4

Growth of PTCDA on Cu(001)

The adsorption of organic molecules on metal surfaces is of highest interest for applications in the field of organic electronics [10, 16, 49, 81, 162] and for fundamental studies of the interaction mechanisms. Of particular interest is the initial growth and the formation of the first molecular layer, as this layer acts as a template for further growth and determines the charge injection properties at the interface [171, 195, 200].
In this chapter, the initial growth of the perylene derivative PTCDA on Cu(001) is investigated not only qualitatively, but quantitatively. The attractive intermolecular interaction of the PTCDA molecules leads to the growth of compact islands at already very low coverage. This attractive interaction determines the cohesion energy $E_B^{(2)}$ of two PTCDA molecules while the diffusion barrier E_D is strongly influenced by the interaction between molecule and substrate. Here, these two important growth parameters are determined.

In the first section of this chapter, it is shown that the growth of the first monolayer PTCDA on Cu(001) can be divided into three regimes: nucleation, aggregation and coalescence. Then, the island number densities (number of islands per unit area) are determined within the aggregation regime for various experiments performed at different substrate temperatures (300 K-390 K) but with a constant deposition rate. An Arrhenius-type plot reveals two temperature regimes which most probably exhibit two different critical cluster sizes. This data has the potential to reveal the diffusion barrier E_D of one and the cohesion energy $E_B^{(2)}$ of two PTCDA molecules on Cu(001) when the critical cluster sizes i are known. Therefore, these critical cluster sizes are determined for both regimes in the third and fourth section. This is done by applying methods developed for atomic nucleation on surfaces which were introduced in chapter 3. The first method is based on the analysis of island size distributions while for the second method the critical cluster size is calculated from the dependence of the island number densities on the deposition rate. In section 5, the diffusion barrier E_D and, in combination with pair potential calculations, the cohesion energy $E_B^{(2)}$ are identified for PTCDA on Cu(001). Finally, the determined critical cluster sizes i are discussed in section 6.
Please note that the growth study presented here has been started within the framework of the dissertation of Caroline Henneke [66] and was finished within this thesis. Therefore in the first three sections, LEEM measurements performed

and analysed by Caroline Henneke are briefly presented and discussed. The corresponding conclusions are then used for the further investigations reported in the last three sections.

4.1 Aggregation regime

Atomic and molecular growth of a monolayer can in gerneral be divided into three regimes: nucleation, aggregation and coalescence. This is indicated for the example of PTCDA on Cu(001) in Fig. 4.1 with a LEEM image series measured by Caroline Henneke [66]. In the nucleation regime, new PTCDA islands nucleate until a coverage of 0.08 ML is reached. From this point on, the number of islands is constant and the islands grow in size. This is the second regime, the aggregation regime. The islands at a coverage of 0.23 ML and 0.47 ML are shown in Fig. 4.1 (b) and (c), respectively. The end of the aggregation regime is marked by starting coalescence of PTCDA islands at 0.65 ML. In this experiment, the begin and end of the aggregation regime were well-visible. This is an important prerequisite for all following analyses since they all are valid only in the aggregation regime.
For higher coverages, more islands grow together (Fig. 4.1 (d)) until almost the entire surface is covered by the monolayer (Fig. 4.1 (e)). The nucleation of the second monolayer (dark contrast in Fig. 4.1 (f)) starts as soon as the first layer is completed but not before which is in good agreement with previous results

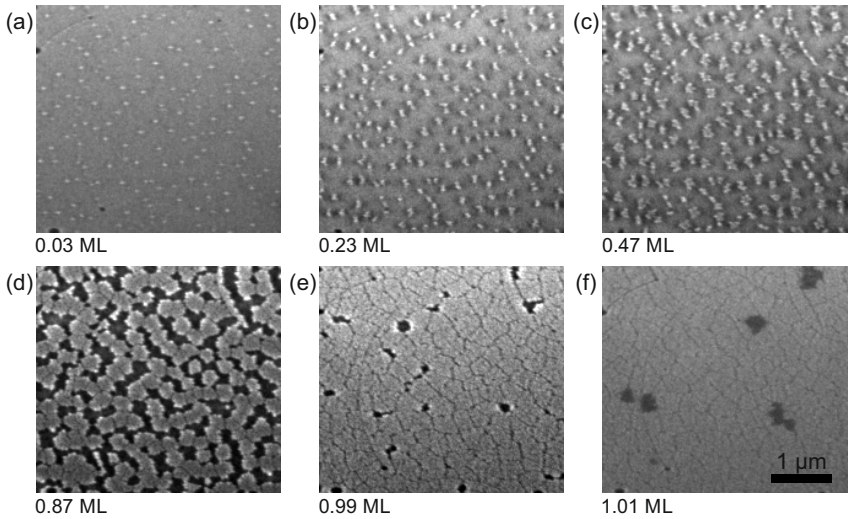

Figure 4.1: LEEM image series taken during the growth of PTCDA on Cu(001) at 350 K with a deposition rate of 25 min/ML. (a) Nucleation of PTCDA islands (bright contrast) starts soon after the deposition is started. (b, c) In the aggregation regime, the existing islands grow in size but their number stays constant. (d) The islands start to coalesce. (e) The first monolayer of PTCDA is nearly complete. (f) As soon as the first layer is complete, the second layer starts to nucleate (dark contrast). Images were taken at 2 V (a-c) and 1.3 V (d-f) with slight under focus. This figure has been adapted from [66] with permission.

[105, 106].

4.2 Island density vs. temperature

According to classical mean-field nucleation theory, the cohesion energy $E_B^{(s)}$ of one molecule to a cluster of $s-1$ molecules and the diffusion barrier for individual molecules E_D can be determined by measuring the island densities ρ in the aggregation regime at different temperatures T but for a constant deposition rate R if the critical cluster size i is known and desorption is neglectable [23, 24, 177, 178]:

$$\rho \propto \exp\left(\frac{\Sigma_{s=2}^{(i)} E_B^{(s)} + i \cdot E_D}{(i+2) k_B T}\right). \tag{4.1}$$

In order to determine these energies, Caroline Henneke has performed and analysed twelve deposition experiments of PTCDA at different substrate temperatures (300 - 390 K) but constant deposition rate in her thesis [66]. The influence of step edges was avoided by only considering islands in sufficient distance to the step edges. Measurements at higher temperatures were not possible since the high mobility of the molecules leads to only one island growing on each terrace and the influence of step edges became crucial.
The island densities of these twelve experiments are shown in an Arrhenius-type plot in Fig. 4.2. The linear trend expected from equation 4.1 is clearly visible but also a clear kink at 317 K and different slopes for higher and lower temperatures.

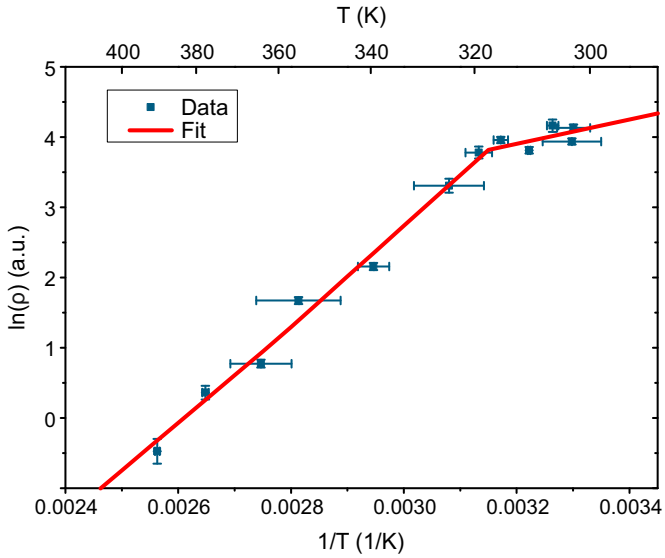

Figure 4.2: Log-plot of the island density ρ vs. the inverse substrate temperature T (Arrhenius-type plot). A linear dependency is expected according to equation 4.1. The clear change in slope at approximately 317 K is caused by a change in the critical cluster size. This figure has been adapted from [66] with permission.

This indicates a change of the critical cluster size at this temperature. For the quantitativ analysis, see [66].

4.3 Critical cluster size and island size distributions

A well-established method to determine the critical cluster size i from island size distributions is based on the dynamic scaling assumption [6, 38, 39, 113, 179] which was developed for adatoms on surfaces and corresponds to a normalization to eliminate the influence of the coverage on the island size distribution. It was already successfully applied to several molecular adsorbate systems [25, 119, 129, 155, 165]. In the PhD thesis of Caroline Henneke [66], it has been shown that this normalization is also applicable for the system PTCDA on Cu(001).
The island size distributions of PTCDA on Cu(001) deposited at various temperatures were extracted from LEEM images taken in the aggregation regime [66]. In Fig. 4.3, they are depicted after normalization. In the next step, the critical cluster size i was determined by comparing the peak width of the normalized island size distribution with the theoretical curves $f_i(s/S)$. For the theoretical curves, the ansatz of Amar et al. [5] is applied (see section 3.3 for more details). For temperatures below 317 K, the experimental island size distributions are in good agreement with the theoretical curves for $i = 1$ as shown in Fig. 4.3 (a). Fortunately, this result allows to determine the diffusion barrier E_D. With increasing temperature, it is expected that the critical cluster size increases since

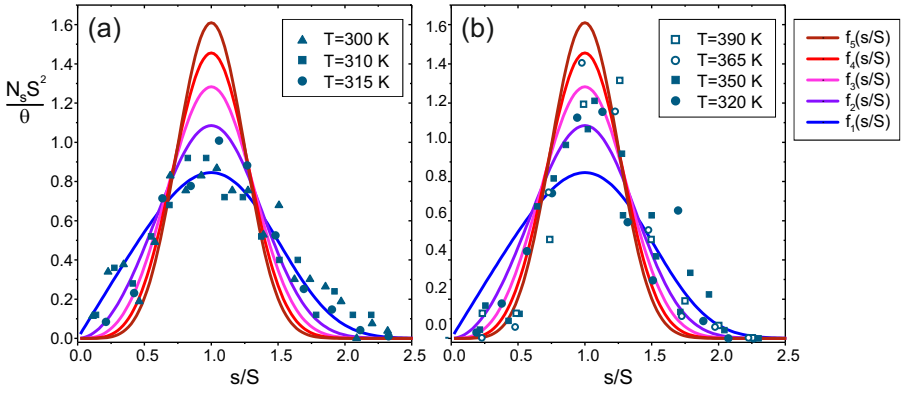

Figure 4.3: Island size distributions for different substrate temperatures during the deposition. (a) For temperatures below 317 K, the data points represent the shape of the theoretical curve for $i = 1$ very well. (b) With increasing temperature, it is expected that the critical cluster size increases since we observed a change in slope in Fig. 4.2. In accordance with this, the shape of the measured island size distributions become narrower. But it is hard to distinguish if the theoretical curve for $i = 2$ or $i = 3$ fits the data better. This figure has been adapted from [66] with permission.

a change in slope was observed in Fig. 4.2. In accordance with this, the shape of the measured island size distributions become narrower. But it is hard to decide whether the theoretical curves for $i = 2$ or $i = 3$ agree better with the experimental data, so it is unclear whether the critical cluster size increases to 2 or 3 [66].
Therefore, another approach to determine the critical cluster size i is chosen in the framework of this dissertation where the deposition rate is varied instead of the substrate temperatures.

4.4 Critical cluster size and deposition rate variation

The approach to determine the critical cluster size i for temperatures above 317 K is based on the dependency of the island density ρ on the deposition rate R and the diffusion constant D at constant substrate temperature T [24, 177]:

$$\rho \propto \left(\frac{D}{R}\right)^{\chi}, \quad \chi = \frac{i}{i+2}. \tag{4.2}$$

Since D is a constant in the observed system, the critical cluster size i determines the slope of $ln(\rho)$ if plotted versus $ln(R)$. However, this method is experimentally very expensive because many measurements with (very) different deposition rates are necessary to determine the critical cluster size. Since we know from the previous results that the critical cluster size does not change for the temperature range from 317 K to 390 K, it is sufficient to choose only one temperature within this regime. Therefore, 13 experiments have been performed with deposition rates in the range of 6-225 min/ML at a temperature of 334 K. The results are shown in Fig. 4.4 in a log-log plot of the island density ρ vs. the deposition rate R. The linear fit to the data is indicated as dashed line and has a slope which corresponds to $i_{\mathrm{FIT}} = 2.81 \pm 0.44$. This value is in good agreement with $i = 3$ while $i = 2$ is out of the experimental uncertainty. Note that three linear curves are included in the plot with slopes calculated for the critical cluster sizes $i = 2, 3$ and 4; clearly, the one for $i = 3$ agrees best with the data. Therefore, we conclude that the correct critical cluster size for the temperature range from 317 K to 390 K is $i = 3$ while it is $i = 1$ for temperatures between 300 and 317 K as it was discussed before.

These results open up new questions which are addressed in the following sections: Why is the critical cluster size $i = 2$ not observed, why does it directly change from 1 to 3 at 317 K, and which conclusions can be drawn regarding cohesion energies?

4.5 From critical cluster sizes to energies

From the critical cluster sizes and the slopes in Fig. 4.2, the diffusion barrier and cohesion energies for certain molecular arrangements can be obtained. The case of $i = 1$ gives the diffusion barrier while cases of $i > 1$ may allow to calculate the cohesion energy of one molecule to a cluster of $i - 1$ molecules. In our case, we have experimental data for $i = 1$ and $i = 3$.

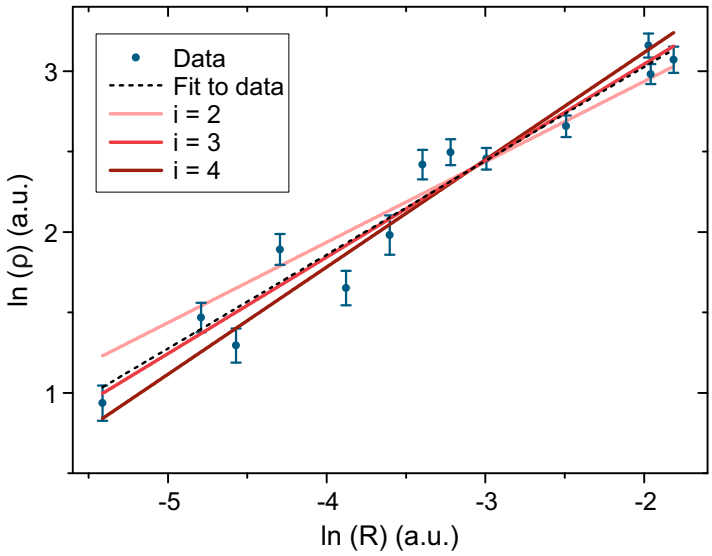

Figure 4.4: Log-log plot of the island density ρ vs. the deposition rate R of 13 experiments with deposition rates in the range of 6 - 225 min/ML. For comparison, three theoretical curves with fixed slopes, according to the corresponding critical cluster sizes, are included into the plot. The slope of the fitted curve is in good agreement with the theoretical curve for $i = 3$.

For temperatures below 317 K, a critical cluster size of 1 was observed. This enables to calculate the diffusion energy with the slope m_1 [66] for the corresponding temperature regime in Fig. 4.2 with equation 4.1:

$$m_1 = \frac{E_\mathrm{D}}{3k_\mathrm{B}} \rightarrow E_\mathrm{D} = (0.45 \pm 0.21)\,\mathrm{eV}. \tag{4.3}$$

This value is higher than the one determined by Tejima et al. [165] who found a range of $0 < E_\mathrm{B} < 0.20\,\mathrm{eV}$ for pentacene on SiO_2.
Between 317 K and 390 K, a critical cluster size of 3 is observed. In combination with the corresponding slope m_3 [66] in Fig. 4.2 and the already calculated diffusion barrier E_D, the cohesion energy of three molecules $E_\mathrm{B}^{(2)} + E_\mathrm{B}^{(3)}$ can be determined:

$$m_3 = \frac{3E_\mathrm{D} + E_\mathrm{B}^{(2)} + E_\mathrm{B}^{(3)}}{5k_\mathrm{B}} \rightarrow E_\mathrm{B}^{(2)} + E_\mathrm{B}^{(3)} = (1.77 \pm 0.68)\,\mathrm{eV}. \tag{4.4}$$

Since a critical cluster size of 2 is not observed experimentally, only the sum $E_\mathrm{B}^{(2)} + E_\mathrm{B}^{(3)}$ can be obtained directly. But, a closer look at the smallest stable molecular configurations for different critical cluster sizes as illustrated in Fig. 4.5 and pair potential calculations based on van-der-Waals and electrostatic interaction [95] allow to correlate $E_\mathrm{B}^{(2)}$ and $E_\mathrm{B}^{(3)}$ with each other.

From STM and LEED measurements [54, 131], it is known that PTCDA molecules form a commensurable herringbone pattern on Cu(001). Therefore, only molecular orientations are considered which correspond to this geometry

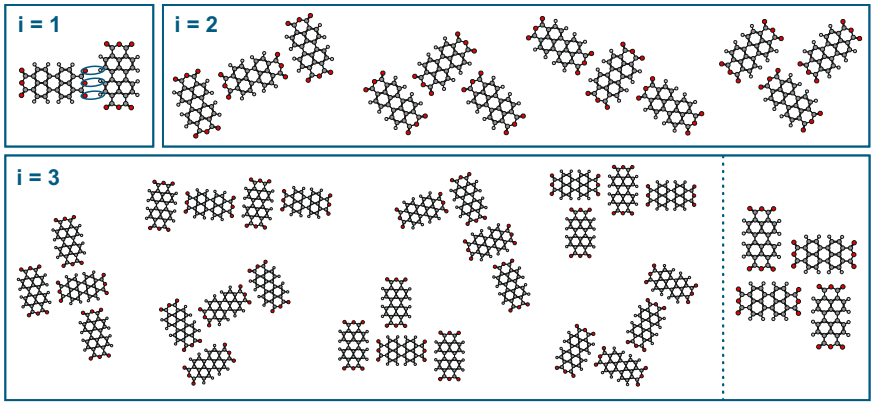

Figure 4.5: Stable molecular configurations for different critical cluster sizes assuming that the herringbone structure of PTCDA/Cu(001) is already formed within such small clusters of PTCDA. For nearly all cases, the last incorporated molecule achieves a similar energy gain considering van-der-Waals and electrostatic effects (according to pair potential calculations) and is able to form three additional hydrogen bonds to the existing cluster as indicated for $i = 1$ (blue ellipses). Only the configuration on the right for $i = 3$ is different. Here, six hydrogen bonds can be formed and the energy gain considering van-der-Waals and electrostatic effects is significantly higher (see text for more details).

(assuming that the influence of the substrate, the condition of commensurability, is crucial already for such small clusters).
For the case of $i = 1$, one of the two situations found experimentally, the smallest possible cluster consisting of two molecules is already stable. Within the herringbone pattern, this allows only one configuration, as shown in Fig. 4.5. It has been shown earlier that positioning two PTCDA molecules in an orientation corresponding to the herringbone pattern leads to an energy gain of maximal 0.63 eV considering van-der-Waals and electrostatic interaction [95]. Three additional hydrogen bonds that can be formed between the molecules stabilize the configuration even further as indicated in Fig. 4.5 for $i = 1$ with blue ellipses.
When a third molecule is added, four possible configurations can be found which are in agreement with the commensurate herringbone pattern (Fig. 4.5, $i = 2$). In all four cases, the third molecule is able to form again three additional hydrogen bonds and, according to pair potential calculations (an example is shown in Fig. 4.6 (a)), it yields a similar energy gain as the second molecule considering van-der-Waals and electrostatic effects (maximal 0.61 eV). This means that a similar amount of energy has to be spent to separate one molecule from a cluster of 2 or 3 molecules. Therefore, the assumption of $E_B^{(2)} \approx E_B^{(3)}$ is reasonable.
With this assumption and eq. 4.4, the cohesion energy of two PTCDA molecules on Cu(001) amounts to

$$E_B^{(2)} = (0.89 \pm 0.34)\,\text{eV}.$$

This value is higher than the binding energy for pentacene on SiO2 of < 0.40 eV [165] and for para-hexaphenyl on amorphous mica of 0.74 eV (calculations) [119].

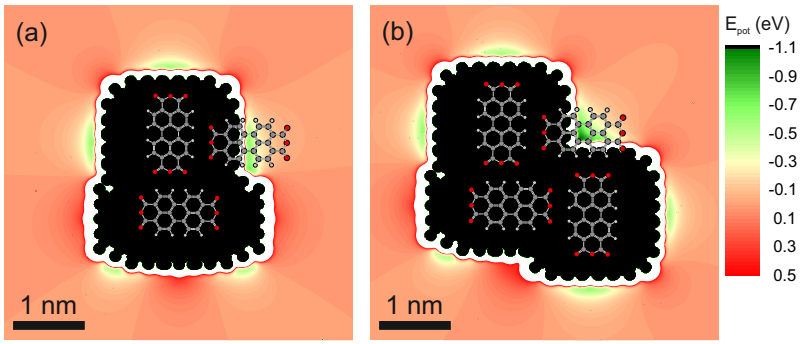

Figure 4.6: Examples of pair potential calculations for a PTCDA molecule approaching a cluster of (a) two and (b) three molecules: (a) The position of two molecules are fixed while the pair potential considering van-der-Waals and electrostatic effects is calculated for the third molecule at various positions. The maximal energy gain in an orientation corresponding to the herringbone pattern amounts to 0.61 eV. (b) For this configuration of four molecules, the energy gain for the fourth molecule amounts to more than 1.05 eV.

If it is assumed that van-der-Waals and electrostatic effects contribute with about 0.6 eV, which is in general agreement with the pair potential calculations [95], the three H-bonds have to contribute with 0.1 eV each in order to explain this value for $E_B^{(2)}$ and $E_B^{(3)}$. This appears to be realistic although all values might be slightly to high.

4.6 Change in critical cluster size at 317 K

In the last section, the cohesion energy of two PTCDA molecules on Cu(001) $E_B^{(2)}$ was determined although a critical cluster size of two is experimentally not observed. But so far, the reason for the omission of the critical cluster size $i = 2$ was not discussed. An explanation is given with Fig. 4.5.
Here, all possible binding configurations for two, three and four molecules within one cluster are depicted. For nearly all cases, the last incorporated molecule achieves a similar energy gain considering van-der-Waals and electrostatic effects (about 0.6 eV) and is able to form three additional hydrogen bonds to the existing cluster. Therefore, a very similar amount of energy is necessary for all these configurations to break one molecule out of the cluster. Only, the configuration on the right for $i = 3$ is different. Here, six hydrogen bonds can be formed and the energy gain considering van-der-Waals and electrostatic effects amounts to more than 1 eV (see Fig. 4.6 (b)). Hence, this configuration is expected to be significantly more stable than the other possible configurations for $i = 3$ and for $i = 2$ and $i = 1$.
Therefore, it is plausible that a temperature regime exists where a cluster of four PTCDA molecules is stable on Cu(001) while all smaller clusters are unstable. This situation corresponds to a critical cluster size of $i = 3$ which was found experimentally for 317 K-390 K. With decreasing temperature, it is expected that also the configurations consisting of three molecules ($i = 2$) become stable

at some point. However at the same temperature also clusters of two molecules already become stable as demonstrated by the energy calculations reported in the last paragraph ($E_B^{(2)} \approx E_B^{(3)}$). Therefore, no temperature window exists where a cluster of three molecules is stable while a cluster of two is unstable. This causes the direct jump form $i = 3$ to $i = 1$ as it is observed at 317 K, experimentally.

4.7 Summary

In this chapter, the growth of PTCDA on Cu(001) was examined not only qualitatively, but quantitatively. By analysing island size distributions within the aggregation regime and applying methods developed for atomic nucleation on surfaces, it was possible to determine the critical cluster size i for the formation of stable clusters for temperatures between 300 K and 390 K. The fact that a value of $i = 1$ was found for temperatures below 317 K enabled to calculate the diffusion barrier for individual molecules on this surface: $E_D = (0.45 \pm 0.21)$ eV. For temperatures above 317 K, the case of $i = 2$ is experimentally not observed; instead four molecules are needed to form a stable cluster ($i = 3$). Nevertheless, it was possible to determine in combination with pair potential calculations a second crucial parameter for layer growth: the cohesion energy of two molecules which amounts to $E_B^{(2)} = (0.89 \pm 0.34)$ eV. Additionally, the direct change of critical cluster size from 1 to 3 at 317 K could be explained.

Chapter 5

Growth of NTCDA on Cu(001)

Molecular adsorbate systems offer a variety of possibilities to tune their geometric, electronic, and optical properties. Of particular interest is the initial growth and the formation of the first molecular layer since this layer acts as a template for further growth, it determines the charge injection properties at the interface, and therefore strongly influences the properties of the interface as well as of any thicker films grown on top [171, 172, 195, 200].
Many studies of molecular adsorbate systems found in literature deal with large π-conjugated molecules on different surfaces. Amongst the most intensively studied systems, one finds the perylene derivative PTCDA and its naphtalene-counterpart NTCDA, as well as different (metal-)phthalocyanines (MePc).
The first group of molecules (PTCDA and NTCDA), when adsorbed on noble metal surfaces like Ag(111) [35, 53, 57, 84, 85, 106, 107, 156], Ag(110) [57, 146, 188], Ag(001) [76], Cu(001) [54], Cu(111) [181], Au(100) [104] or Au(111) [104, 201], was frequently found to form compact molecular islands already at very small coverages (far below one monolayer), and the area in between remains uncovered (apart from a small amount of diffusing molecules). This is due to attractive forces between the molecules, not only caused by van der Waals interaction, but by the quadrupole moment which these molecules exhibit due to their anhydride groups. In many cases, this interaction is also influenced by substrate mediated coupling mechanisms [97, 167]. With increasing coverage, the islands grow in size until the entire surface is covered, and multi-layer growth occurs consequently in a layer-by-layer (Frank-van der Merwe) growth mode, or in the form of three-dimensional islands on one (or more) wetting layer(s) (Stranski-Krastanov growth mode). In the submonolayer regime, transitions between phases with different packing densities occur frequently.
The second group of molecules mentioned, MePcs, exhibits a different behaviour on certain surfaces. For CuPc, SnPc, TiOPc and H_2Pc on Ag(111), the formation of a diluted two-dimensional (2D) gas phase was reported [92–95, 154, 159, 176] covering the entire surface completely already in the low coverage regime. When the coverage is increased, the density of the gas increases; therefore, the average intermolecular distance becomes smaller which can be traced back in low energy electron diffraction (LEED). Only above a critical coverage, which – depending on the system – lies between 0.7 ML and 0.95 ML, well-ordered phases occur, in some cases exhibiting a unit-cell the size of which changes continuously with coverage. This proofs that the behaviour of this molecular adsorbate is determined

by a (substrate mediated) repulsive intermolecular interaction [94, 95, 154, 159].

In the first and second section of this chapter, a growth mode is discussed that does not correspond to these two scenarios. Based on low-energy electron microscopy (LEEM) and diffraction (LEED) as well as scanning tunneling microscopy (STM), evidences for dendrite-like, fractal growth of NTCDA on Cu(001) in the submonolayer regime are presented. While LEEM and LEED have proven to be excellent tools to investigate growth and lateral structure of molecular (mono)layers on metal surfaces in-situ and in real time [34, 67, 107, 132, 134, 140, 141, 158], normal incidence x-ray standing waves (NIXSW) and angle-resolved photoelectron spectroscopy (ARPES) have been additionally applied to study the vertical geometric and the electronic structure of this system. Therefore, a comprehensive characterization of this interesting adsorbate system is presented including a growth model that can explain the unexpected fractal growth mode.
In section 3, the system NTCDA on Cu(001) is used as prototype system for a proof of principle experiment, namely to demonstrate that momentum microscopy of a single domain of NTCDA is possible with the LEEM/PEEM instrument.
Finally, a second phase of NTCDA on Cu(001), which occurs at higher substrate temperatures, is discussed in section 4.
Please note that the study of NTCDA on Cu(001) presented in the first two sections corresponds to a joint project of Markus Franke and myself. Markus Franke was responsible for the XSW and PES analysis and performed the STM measurements (more details can be found in [50]) while I was responsible for the LEEM and LEED data and performed the PP calculations.
Furthermore, the majority of the LEEM and LEED data presented in this chapter was collected under my guidance in the framework of the Master's thesis of Jana Wolters.
Shortly after the submission of this thesis, the content of sections 5.1 and 5.2 was published in [41] and the content of section 5.3 was published in [43].

5.1 NTCDA on Cu(001) at room temperature

In this section, the dendrite-like, fractal growth of NTCDA on Cu(001) in the submonolayer regime at room temperature is discussed. First, evidences for this unexpected growth mode based on low-energy electron microscopy (LEEM) and diffraction (LEED) as well as scanning tunneling microscopy (STM) are presented. Additionally, normal incidence x-ray standing waves (NIXSW) and angle-resolved photoelectron spectroscopy (ARPES) are applied to study the vertical geometric and the electronic structure of this system. Finally, a growth model is discussed that can explain the unexpected fractal growth mode by an intermolecular interaction favouring growth of long and thin molecular chains which is mainly caused by the molecule-substrate interaction.

5.1.1 Experimental results

Low energy electron microscopy

The growth of NTCDA on Cu(001) in the submonolayer regime is investigated using LEEM and LEED in real time during the deposition process. At first, the bright field (BF-)LEEM mode was chosen since island formation was expected as it was found for PTCDA on Ag(111), Cu(001) (compare chapter 4) and Au(111), or for NTCDA on Ag(111) and Au(111) [67, 107]. For these adsorbate systems, compact islands were found, and could be clearly distinguished from the clean substrate surface due to their different intensity in the (00) LEED spot. Therefore, BF-LEEM was the right choice for these *in situ* experiments. For NTCDA on Cu(001), however, no indications for compact islands are found in the BF-LEEM mode, as can be seen in Fig. 5.1 (a) and (b). Beside step edges and some point-defects, no structures or islands are visible. When the coverage is increased, the only clear change in the BF-LEEM images is a decrease of the over-all intensity, homogeneously in the entire field of view. A full series of images from 0 to 1 ML can be found in section 5.2.1. The observation holds for different focus settings and start voltages, and was found all over the sample surface. For the case of $U_{\mathrm{start}} = 2$ V, the overall BF-LEEM intensity vs. coverage is plotted in Fig. 5.1 (e). It can be seen that the intensity decreases almost linearly, interrupted by a small plateau at 56 min which corresponds to the closing of the first adsorbate layer. Afterwards, when the second layer starts growing, the BF-LEEM intensity decreases further, and at the same time compact (2nd-layer) islands are visible in the BF-LEEM images (see section 5.2.1).

The obvious conclusion from these observations, namely that NTCDA does *not* form ordered islands on Cu(001) but possibly a disordered 2D gas similar to phthalocyanine molecules on many coinage metal surfaces (see above and Refs. [94, 95, 154, 159, 176]), is thwarted by LEED: Figure 5.1 (c) and (d) show LEED images recorded at the same coverages as the BF-LEEM images in panels (a) and (b). In both cases, a clear diffraction pattern is visible, unambiguously proving that there are long-range ordered structures present on the surface. The LEED pattern becomes visible already at about 0.2 ML, whereby the spots are slightly elongated at these low coverages (up to about 0.6 ML). With the coverage increasing to 1.0 ML, the spots become continuously sharper and round, see section 5.2.1. The LEED pattern corresponds well to the superstructure found by Fink et al. [44]. As a matter of fact, it is therefore stated that NTCDA forms ordered structures already in the (low) submonolayer regime which are invisible in BF-LEEM. As one can easily see from Fig. 5.1 (f), this is not due to an accidentally vanishing contrast between the NTCDA islands and the bare copper substrate. The LEEM-IV curves plotted for the bare and NTCDA-covered Cu(001) surface (black and green data points, respectively), as recorded from the clean (0 ML coverage) and fully covered surface (1 ML coverage), clearly show sufficient contrast in a rather wide range of start voltages from 1 V to 3.5 V. The BF-LEEM images shown in Fig. 5.1 and in section 5.2.1 were recorded at $U_{\mathrm{start}} = 2$ V. Therefore, compact NTCDA-islands above the resolution limit of 10 nm (the experiments were performed without the abberation corrector) would be clearly visible in the BF-LEEM images if they were present.

To shine light on this puzzle, DF-LEEM was applied, which was easily possible

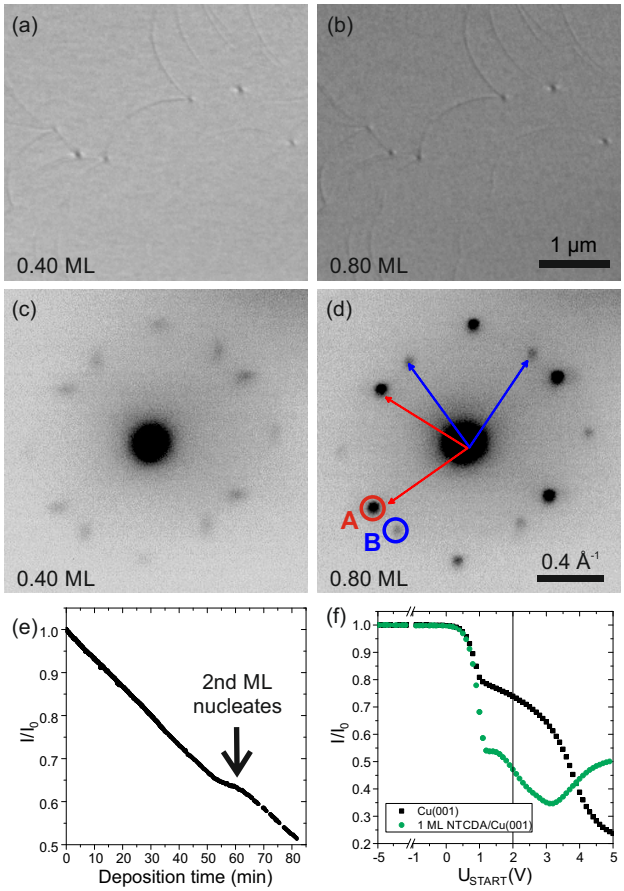

Figure 5.1: (a) and (b) BF-LEEM images of NTCDA on Cu(001) at coverages of 0.4 ML and 0.8 ML, respectively ($U_{\text{start}} = 2$ V). The over-all intensity is decreasing with coverage but no island formation is visible. (c) and (d) μLEED images recorded at the same coverages ($U_{\text{start}} = 7.5$ V). In (d), the reciprocal lattice vectors of the two domains and the LEED spots selected for DF-LEEM (see Fig. 5.2) are indicated in red and blue. (e) BF-LEEM intensity plotted vs. deposition time ($U_{\text{start}} = 2$ V). After 56 min, the nucleation of the second layer is clearly visible in the otherwise linear progress. (f) LEEM-IV measurements performed for a clean Cu(001) surface (black data points) and for one closed layer (1 ML) of NTCDA on Cu(001) (green data points). At a start voltage of 2 V, as it was used for the BF-LEEM images, a clear contrast is present for both curves. For complete LEEM and LEED series, see section 5.2.1.

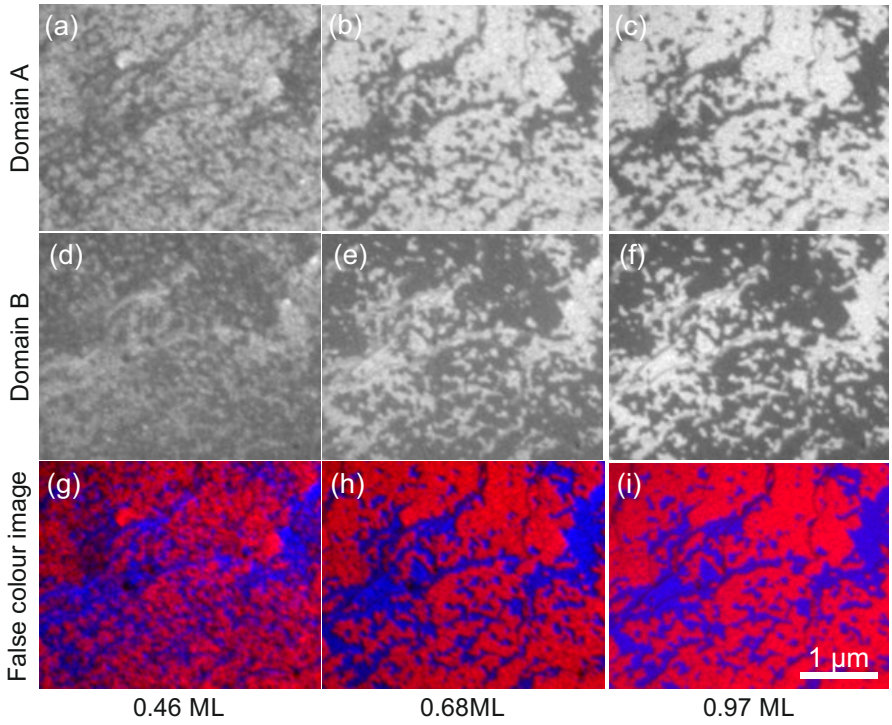

Figure 5.2: DF-LEEM of NTCDA on Cu(001) at different coverages (0.46 ML, 0.68 ML and 0.97 ML, U_{start} = 2.4 V). For (a)-(c) and (d)-(f), the rotational domains A and B were selected, respectively. (g)-(i) False colour representation of the rotational domains. Red and blue coloured areas indicate those parts of the surface which are covered by domain A and B, respectively. Colour coding corresponds to the selected spots in the μLEED images shown in Fig. 5.1 (d).

since LEED spots can be identified above 0.2 ML coverage. As indicated in Fig. 5.1 (d) in red and blue, the LEED image is the superposition of the patterns of two domains of NTCDA on Cu(001) which are rotated by 90° with respect to each other. In DF-LEEM, these two different domains can be made visible by selecting one of the LEED spots corresponding to just one of the domains for imaging. The result is shown in Fig. 5.2 (a)-(c) for one (the "red") domain, and in (d)-(f) for the other ("blue") domain. In these images, only those parts of the surface appear bright that are covered by a structure corresponding to the LEED spot selected for DF imaging. In Fig. 5.2 (g)-(i), false-colour images are shown which are obtained by merging the corresponding DF-LEEM images of both domains after colouration with their representative colour, red or blue. These images therefore indicate the parts of the surface covered with domain A in red and with domain B in blue.

In DF-LEEM, a (domain) contrast is already visible at moderate coverages (in contrast to the BF-LEEM images shown above). As can be seen clearly in all three series (a)-(c), (d)-(f) and (g)-(i) of Fig. 5.2, the size and shape of the domains are formed early (at coverages below 0.5 ML), and do *not* change signifi-

cantly during further deposition of NTCDA. The contrast between both domains becomes much clearer since the DF-LEEM intensity increases with increasing coverage but the size and shape of both domains hardly changes. This is very surprising and remarkable, since it means that already at low coverages certain areas of the surface are "reserved" for each of the two domains, and within these reserved areas, the NTCDA structure is already formed to such an extend that it gives rise for a decent LEED pattern. With increasing coverages, the structure on these areas becomes more and more distinct, as can be seen by the increase in the DF-LEEM intensity, but the shape and size of the "reserved" space remains unchanged during the entire growth experiment.

Both BF- and DF-LEEM results are not compatible with the originally expected growth of compact, ordered islands of NTCDA/Cu(001). The conclusion from these result is that at low coverages the molecules spread over the entire surface, reserving a certain space for "their" domain orientation, and in some way stamp the domain type on the respective surface area. When the coverage increases, these areas (and therefore the domain size and shape) are static while the DF-LEEM contrast increases, and the LEED spots become sharper and sharper. The fact that BF-LEEM does not show any (domain) contrast is simply a consequence of the (00) spots of both domain types being equivalent in their intensity. However, the fact that the BF-LEEM intensity decreases homogeneously indicates that the molecular density does increase linearly and homogeneously with increasing coverage. Therefore, the islands of both domains formed early in the growth experiment must be rather diluted in the beginning, and become more and more densely packed during NTCDA deposition. These observations are compatible with fractal growth.

Scanning tunnelling microscopy

The system NTCDA/Cu(001) has been investigated with room-temperature (RT) STM by Markus Franke [50]. Figure 5.3 (a) shows an STM image ($U_{\text{bias}} = -0.75\,\text{V}$, $I_{\text{tunnel}} = 0.03\,\text{nA}$) of approx. 0.8 ML NTCDA on Cu(001). Rows of molecules are clearly visible (marked in red and blue for the two different domains), and the islands are clearly elongated in the direction of these rows. This leads to a preferred island shape, as illustrated in Figure 5.3 (d) with blue and red lines following the contour lines of the islands. In (b) and (e), a larger section of the same sample is shown. The island shape allows us to identify the domain type, as marked in (e). Rather large coherent areas are observed on the surface, which are filled with several smaller islands of the same domain type. Many of the small islands are connected but they do not coalesce or form compact islands.

At lower coverage (< 0.5 ML, Fig. 5.3 (c)), the situation is similar: Many elongated islands (dark contrast) cover the surface, separated by as many clean surface areas. The islands do not coalesce, and change only slowly when the same surface area is scanned by the STM tip repeatedly (as reported in Ref. [168] and section 5.2.2). However, when the islands are marked again according to their rotational domain type (Fig. 5.3 (f)), it can be seen that neighboring islands very often exhibit the same orientation. Hence, both domains occupy large connected regions already at this small coverage whereby the available surface area is by far not completely filled yet. The "reserved" regions of both domain types are of similar size as observed at higher coverages (compare the sizes of the regions

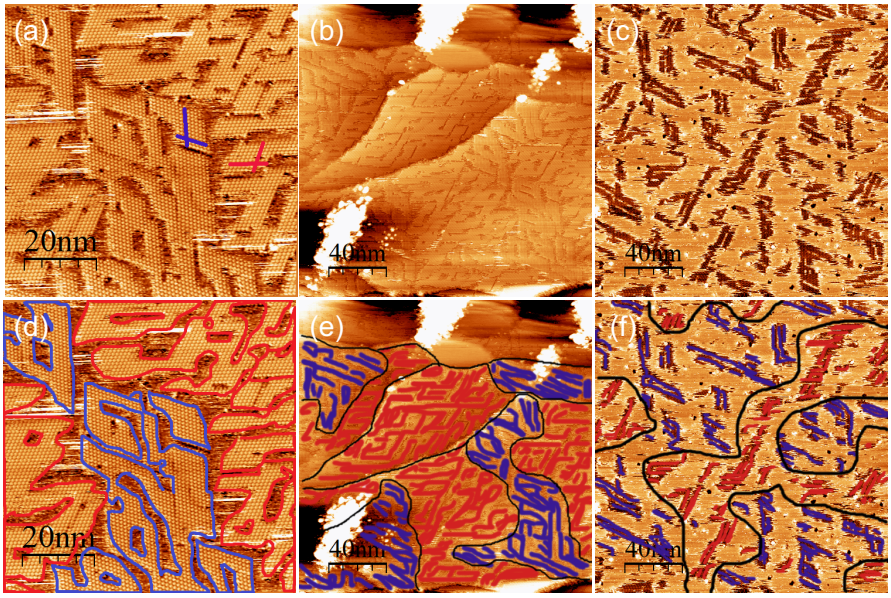

Figure 5.3: (a) and (b) STM images recorded at room temperature for ≈ 0.8 ML of NTCDA on Cu(001) ($U_{\text{bias}} = -0.75\,\text{V}$, $I_{\text{tunnel}} = 0.03\,\text{nA}$). (c) Similar image recorded at a coverage below 0.5 ML ($U_{\text{bias}} = 1\,\text{V}$, $I_{\text{tunnel}} = 0.03\,\text{nA}$). (d)-(f) Same images as in (a)-(c), but with the domain orientation colour-coded in red and blue. This figure has been adapted from [190] with permission.

enclosed by black lines in panels (e) and (f)). This finding is in good agreement with the static domain shape observed in DF-LEEM (see above). However, it is still surprising not to find a statistic distribution of domain orientations. A sort of "interaction" was rather identified between the neighboring islands, which results in identical orientations of the molecules in the islands, so that the islands belong to the same domain type. This interaction must exists already at very low coverages. Here, it is suggested that the mechanism for this "interaction" between the islands is a one-dimensional growth mode of the NTCDA structure which leads to well ordered, molecular chains interconnecting the islands and therefore inducing the cross-talk between them (for details see Discussion). In Fig. 5.3, these very thin interconnecting molecular chains are not visible since they cannot be imaged in RT-STM. Also BF-LEEM cannot image these chains, and not even the islands visible in STM since they are below or very close to the resolution limit of the LEEM/PEEM instrument (about 10 nm). However, LEED is able to trace the strongly anisotropic island shape that is observed here. The elongated LEED spots seen in Fig. 5.1 (c) (see also section 5.2.1), which gradually change to a round shape with increasing coverage, clearly results from the anisotropic shape of the NTCDA islands.

Normal incidence x-ray standing waves

In this and the following section, the results of NIXSW and valence-band photoelectron spectroscopy (PES) experiments are discussed which were obtained for NTCDA/Cu(001) and analysed by Markus Franke [50]. Both studies were initiated in order to investigate the adsorbate-substrate interaction which obviously plays a decisive role for the growth behavior of the system. NIXSW is able to measure the vertical distances (adsorption heights) of the atomic species of the molecules with respect to the underlying substrate. Since these heights can be interpreted as bonding distances, they give insight in the strength of the adsorbate-substrate interaction when compared to covalent or van der Waals bonding distances (geometric fingerprint of interaction strength). Valence-band PES, on the other hand, investigates the electronic structure and can reveal any transfer of electronic charge, most prominently, from the substrate into the (former) lowest unoccupied molecular orbital (F-LUMO). In this sense, valence-band PES can be seen as the electronic fingerprint of the interaction strength.
All photoemission-based data presented here was recorded in the dual-beam UHV end station of beamline I09 at the Diamond Light Source (DLS, Didcot, United Kingdom) using the Scienta EW4000 HAXPES hemispherical electron analyser at beamline I09 having an acceptance angle of 60°.

For NIXSW, C1s and O1s core level spectra have been measured at photon energies close to the Bragg energy of the Cu(002) reflection (3431 eV at RT). Typical XPS data is plotted in Fig. 5.4 (a) and (b). The C1s spectrum shows three main spectroscopic features that can be assigned to C-C and C-O bonded carbon species (labeled "1", main peak and satellite, and "2", respectively). At higher binding energies, a broad energy loss tail together with other satellites is observed which cannot unambiguously be assigned to one of the two species. For the analysis of the carbon species, the sum of the two main peaks of the spectrum is used. The O1s spectrum (Fig. 5.4 (b)) is fitted with four peaks corresponding to the carboxylic ("1") and anhydride ("2") oxygen atoms and their satellites.

The XPS data was recorded at about 25 different photon energies around the Bragg energy. By applying the models shown in Fig. 5.4 (a) and (b), the data was fitted using CasaXPS [37] and the built-in error analysis. The resulting partial yield curves are obtained as function of photon energy. In turn, fitting these yield curves, using our NIXSW analysis software Torricelli [17] that is available as open-source code, allows to determine the adsorption heights of all three relevant atomic species (C as well as O "1" and "2"), and therefore the overall adsorption height of the molecule and the bending due to a more specific interaction of the anhydride groups. For fitting the yield curve, the "dipole+quadrupole" approximation was applied, i.e., non dipolar effects were taken into account [17]. Furthermore, it was considered that our experiment (as every NIXSW experiment) was not performed in perfect normal incidence but with a Bragg angle of $\Theta \approx 86.5°$. This is due to the fact that the intensity of the Bragg reflected beam has to be measured to obtain the reflectivity of the Bragg reflection, and therefore the beam cannot be reflected precisely upstream the incident beam. This small deviation from perfect normal incidence has a non negligible effect, as demonstrated recently [17, 175]. For more details on the correction factors applied in the NIXSW analysis, see section 5.2.3.

The result of the NIXSW analysis performed by Markus Franke [50] is shown

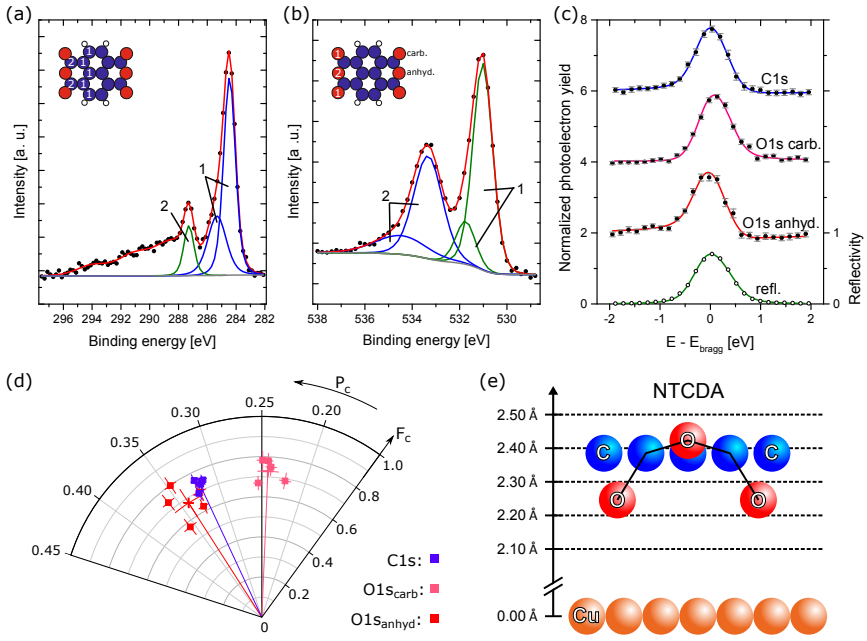

Figure 5.4: XSW results for NTCDA on Cu(001): Typical XPS data for the C1s (a) and O1s (b) core level and best fits to the data. The fitting model was propagated to all XPS data recorded at different photon energies. (c) Reflectivity and (partial) photo-electron yield curves for the relevant species: C represents the molecular backbone, $O_{carb.}$ and O_{anhyd} the two different oxygen species. (d) Argand representation of the fitting results: Data points represent the fitting results (i.e., coherent fractions F^H and positions P^H) of individual scans, thin lines the average for the respective species. Error bars are propagated through XPS [37] and photoelectron yield fitting [17]. (e) Structure model of the adsorption of NTCDA on Cu(001). This data analysis is part of [50].

in Fig. 5.4 (c)-(e). Panel (c) shows typical yield curves for the carbon and the two oxygen species, together with the best fits to the experimental data. Each species was measured several times at different sample positions, and the fit results, which are the coherent position P^H and the coherent fraction F^H for each of the measurements, are plotted in a polar diagram (Fig. 5.4 (d), so called Argand representation). In this diagram, the result of one fit (F^H, P^H) is represented by a polar vector, the length and phase angle of which correspond to the coherent fraction F^H and position P^H, respectively: $(F^H, P^H) = F^H \cdot \exp(2\pi i P^H)$. The coherent position hereby represents the (averaged) vertical position of the adsorbate species to the nearest bulk lattice plane below, in units of the lattice spacing $h_{hkl} = 1.807$ Å. This means that the adsorption height D^H for this species is found by $D^H = d_{hkl}(n + P^H)$, where n is an integer corresponding to the number of lattice planes lying between sample surface and adsorbate. The principally unknown number n usually introduces only an apparent uncertainty since in most cases only one value for n results in reasonable bonding distances. In our case, $n = 1$, since all adsorption heights are slightly larger than the lattice spacing. The

Table 5.1: NIXSW fit results: In the first columns, the coherent position P^H, coherent fraction F^H and the adsorption height D^H are listed for the three relevant species of NTCDA/Cu(001). D^H is also given in units of the corresponding covalent and van der Waals bonding distances ($\frac{D^H}{d_{\text{cov.}}}$, $\frac{D^H}{d_{\text{vdW}}}$), respectively. The last three columns contain values obtained for NTCDA/Ag(111) for comparison. All relative values are calculated based on covalent [29] and van der Waals radii [18] from literature: $r_{\text{C}}^{\text{cov}} = 0.76\,\text{Å}$, $r_{\text{O}}^{\text{cov}} = 0.66\,\text{Å}$, $r_{\text{Cu}}^{\text{cov}} = 1.32\,\text{Å}$, and $r_{\text{Ag}}^{\text{cov}} = 1.45\,\text{Å}$; $r_{\text{C}}^{\text{vdW}} = 1.77\,\text{Å}$, $r_{\text{O}}^{\text{vdW}} = 1.5\,\text{Å}$, $r_{\text{Cu}}^{\text{vdW}} = 1.4\,\text{Å}$ and $r_{\text{Ag}}^{\text{vdW}} = 1.72\,\text{Å}$. This data analysis is part of [50].

	NTCDA/Cu(001) (system under study)					NTCDA/Ag(111) [153]		
species	P^H	F^H	D^H[Å]	$\frac{D^H}{d_{\text{cov.}}}$	$\frac{D^H}{d_{\text{vdW}}}$	D^H[Å]	$\frac{D^H}{d_{\text{cov.}}}$	$\frac{D^H}{d_{\text{vdW}}}$
C1s	0.320(5)	0.74(3)	2.384(9)	1.15	0.75	3.00	1.35	0.86
O1s$_{anh}$	0.34(2)	0.68(8)	2.42(4)	1.22	0.84	3.00	1.42	0.93
O1s$_{carb}$	0.24(1)	0.73(5)	2.25(2)	1.13	0.77	2.75	1.30	0.85

second fit parameter, the coherent fraction, is a measure for the vertical ordering of the considered species. It takes numbers between 0 and 1, 0 corresponding to complete vertical disorder, 1 to perfect order of all atoms on exactly the same adsorption height.

In Fig. 5.4 (d), the result of each individual scan is shown as data point, the averaged result for each species as a thin radial line. The corresponding values of the averaged results are also listed in Table 5.1, in absolute units, as well as relative to the sum of the corresponding covalent [29] and van der Waals [18] radii. Finally, the resulting structure model is shown in Figure 5.4 (e).

Adsorption heights between 2.25 Å and 2.42 Å are found for the three atomic species. All these values are significantly smaller than the sum of the corresponding van der Waals radii (between 75% and 84%) and – in case of C and $\text{O}_{\text{carb.}}$ – already rather close to covalent bonding distances. Compared to the values obtained for NTCDA/Ag(111) (see last three columns in Table 5.1), these bonding distances are significantly shorter [153]. Also in relation to the adsorption heights of PTCDA on different Cu, Ag and Au surfaces, they are extraordinary short [15, 56, 65, 68, 126]. So far, there are only two exceptions known which exhibit similar or even smaller bonding distances for the carboxylic oxygen and the carbon species: PTCDA on Cu(001) (i.e., on the same substrate as studied in this work [186]) and on Ag(110) (i.e., on the most reactive of all Ag surfaces [15]). We conclude that this finding is compatible with an overlap of the molecular orbitals and the metal bands. It indicates a rather strong π-bonding of the naphtalene core of the NTCDA molecule to the surface, and additionally local σ-like bonds between the carboxylic oxygen and the surface Cu atoms. Traces of this weak chemisorption should be visible in the electronic properties of the system as well.

Valence band photo-electron spectroscopy

Valence band PES experiments have been performed using the soft x-ray beam of beamline I09 at the Diamond Light Source during our NIXSW beamtime. There-

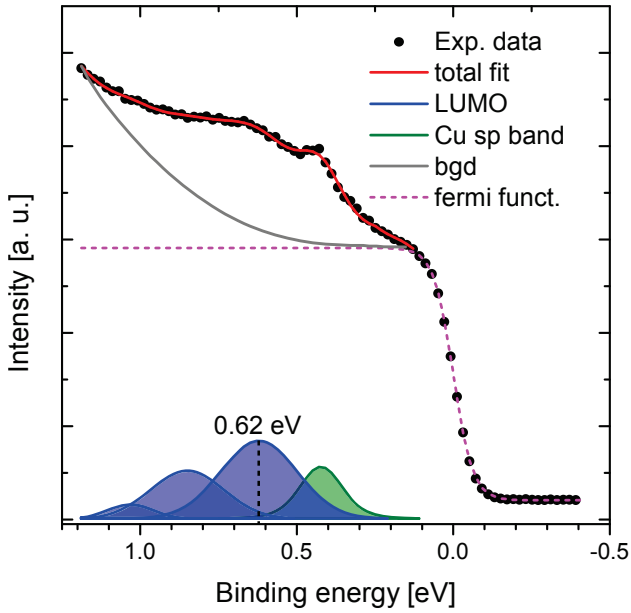

Figure 5.5: Valence band PES measurement of NTCDA on Cu(001) (photon energy = 110 eV, after background subtraction). The broad peak is attributed to the F-LUMO of NTCDA and fitted by a vibronic progression (blue peaks, main component at 0.62 eV). This data analysis is part of [50].

fore, this data is recorded from precisely the same sample for which the NIXSW data was recorded. The analysis was done by Markus Franke [50].
The valence band PES data in the energy range close to the Fermi edge is depicted in Figure 5.5. It was recorded using a photon energy of 110 eV close to normal emission geometry (at an angle of 85° between x-ray beam and sample surface normal). After background subtraction, two main features are visible, a broad asymmetric peak at a binding energy slightly above 0.6 eV and a much sharper feature at about 0.4 eV. While the latter stems from the Cu sp-band, the first is attributed to the F-LUMO of the NTCDA molecule which became filled by charge being transferred from the surface. This asymmetric peak was fitted with three components according to a vibronic progression, as introduced by Wießner et al. [187]. This results in a binding energy of 0.62 eV for the main peak, clearly indicating that the F-LUMO state is completely filled (in agreement with earlier publications [168, 187]). Hence, a charge transfer of two electrons from the substrate into the LUMO state is found, clearly indicating a chemisorptive interaction between the NTCDA molecule and the Cu(001) substrate. This agrees very well with the very small adsorption heights found in NIXSW.

5.1.2 Discussion

The key finding reported in the experimental section is that NTCDA does not form compact islands on Cu(001) up to very high coverages within the submonolayer regime although a rather clear LEED pattern is visible already at approx.

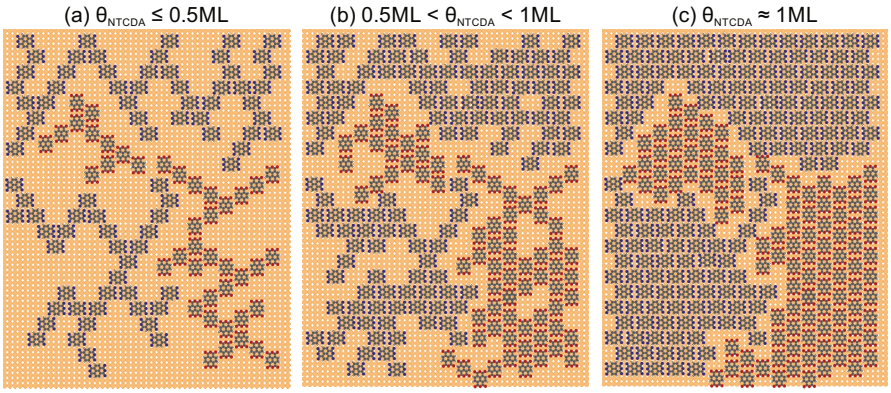

Figure 5.6: Schematic model of dendrite-like growth of NTCDA on Cu(001). (a) For coverages below 0.5 ML, the molecules grow in 1D chains rather than in compact 2D islands, but on a well defined lattice and therefore with good long-range order. Two domains of such dendrite-like structures are formed, as indicated by molecules with red and blue oxygen atoms. (b) With increasing coverage, the voids in the dendrite-like structure are gradually filled with NTCDA molecules, on the basis of the pre-defined lattice. Therefore, the domain size and shape is conserved during this process. (c) The process continues until the surface is entirely covered. This figure has been adapted from [190] with permission.

0.2 ML indicating that an ordered structure exists at this early growth stage. DF-LEEM and STM reveal that size and shape of the domains are defined also very early although the deposited material is not sufficient at this stage to fill the domain areas with a compact structure. Hence, there must be rather diluted (but long-range ordered) structures present on the surface at low coverages. In the following two subsections, a dendrite-like growth model for NTCDA/Cu(001) is presented, which can explain these observations, and the driving force behind the dendrite-like growth mode is discussed. The second part is also based on the XSW and PES results that have indicated a relatively strong interaction between the NTCDA molecules and the substrate involving transfer of electronic charge.

Model of dendrite-like growth

The model of dendrite-like growth is summarized and illustrated in Fig. 5.6. For coverages below 0.5 ML, the molecules strongly prefer to grow in one-dimensional (1D) chains rather than forming compact 2D islands (panel (a)). Nevertheless, they arrange themselves in an ordered pattern, which can be seen as a long-range ordered brick wall structure [44] with many voids but no structural defects violating the translational symmetry. Therefore, they form very quickly an ordered network of molecular chains over a relatively large area of the surface. Although the islands are by far not compact, this (dendrite-like) network produces a well visible LEED pattern; however, owing to the chain-like character of the structure, the LEED spots are elongated.

This process occurs in two symmetry-equivalent domains as indicated in Fig. 5.6 by the molecules with red and blue coloured oxygen atoms. The growth of

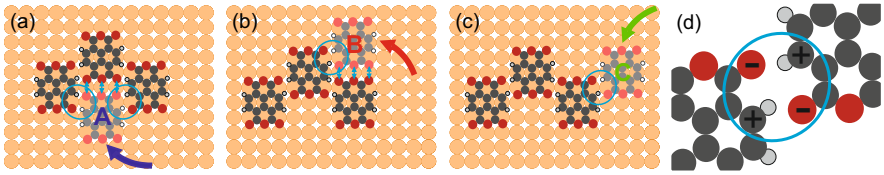

Figure 5.7: (a)-(c) Possible binding sites (labeled "A", "B" and "C") for an NTCDA molecule attaching to an existing cluster of molecules. Blue arrows mark short distances between the (identically charged) anhydride groups of opposing molecules, which are considered energetically unfavourable. Blue circles indicate "quadrupole-like" charge arrangements due to charging of the carboxylic oxygen atoms, as illustrated in (d).

1D chains remains favourable until the growth branches of the domains approach the edges of the neighboring islands. The entire surface is then covered by islands of a diluted, long-range ordered structure. This stage is reached at a coverage clearly below 0.45 ML since DF-LEEM indicated that all surface regions can be attributed to one of the two domain types at a coverage of 0.46 ML (see Fig. 5.2 (g)). From this time on, more molecules being deposited only fill the voids in the dendrite-like structures and arrange themselves on the already defined lattice of the corresponding domain. This is illustrated in Fig. 5.6 (b) and (c). Hence, in this phase, the islands become more compact but the domain shape does not change, in agreement with the static domain shape seen in DF-LEEM and STM. This process of forming more compact islands with less voids furthermore causes an increasing intensity and a roundening of the LEED spots, and therefore also an increasing contrast in DF-LEEM. In BF-LEEM, still no contrast is generated since both domains remain equivalent regarding the intensity of the (00) LEED spot. The homogeneous decrease in the BF-LEEM intensity is due to the increasing overall coverage. Hence, this dendrite-like growth model can explain all experimental results obtained from LEEM, LEED and STM.

Single dendrites were not observed in the STM measurements at low coverages, presumably since the 1D network cannot be imaged by STM at RT. As it is shown in section 5.2.2 for coverages below half a monolayer, even elongated structures with a width of three or more molecules change significantly between consecutive STM scans of the same area, either due to the temperature or due to tip-induced changes. Therefore, it can not be expected that 1D chains of single NTCDA molecules can be imaged under these conditions. However, taking the results of all techniques together, we cannot think of any other conclusive explanation for our observations beside this dendrite-like growth model.

Driving force for dendrite-like growth

The remaining question is the driving force for the 1D growth behavior that causes the formation of molecular chains and dendrite-like structures. This growth mode necessitates that the molecules preferably attach to the ends of the dendrites rather than to their side edges, i.e., they bond to only one molecule of the existing island rather than to two or more. The possible adsorption sites, in accordance

with the lattice of the brick-wall structure [44], are illustrated in Fig. 5.7: Assuming the three darker NTCDA molecules form the existing end of the dendrite-like island, there are basically three different sites where an additional molecule (the lighter one labeled "A", "B" and "C") can attach. While preferred binding to site A and B would result in a more compact island, bonding to site C extends the 1D molecular chain in longitudinal direction and therefore leads to the observed formation of long dendrites.

In the following, pair potential (PP) calculations are utilized in order to estimate the energies that are involved when an NTCDA molecule attaches at one of these three sites. Here, the approach is used, which was suggested at first in Kröger et al. [95] and was successfully applied in several following publications [88, 93, 136, 158]. It is based on a calculation of the interaction potentials of every atom of the first molecule with every atom of all the other molecules, considering van der Waals and electrostatic contributions. In Ref. [95], a simplified way of considering a redistribution of charge in the molecules has been demonstrated, as it originates from, e.g., charge transfer between the molecules and the metal substrate. For the system under study, such charge transfer has to be considered, as clearly indicated by the filling of the F-LUMO.

The filling of the F-LUMO, often entitled as "charge donation" (from the surface into the molecules), is not the only effect of charge reorganization caused by the chemisorptive molecule-substrate interaction. "Back-donation" of charge (from the molecules to the surface) also takes place via a hybridization of the substrate states with the molecular frontier orbitals. This back-donation is counteracting the charging of the molecule caused by filling of the LUMO, but usually does not completely compensate for it so that a (negative) net charging of the molecule remains. This net charging cannot directly be measured, but has been calculated for many organic/metal systems [1, 36, 125–128]. For PTCDA on Ag(111) [126, 128], Ag(110) [1] and Cu(111) [128] and for NTCDA on Ag(111) [36], values for the net charging between 0.35 and 0.50 electrons were calculated. Within the PP approach, the net charge transfer onto the molecule is considered by modifying the partial charges of the individual atoms of the molecule (and in turn the pair potentials), whereby the additional charge can be distributed in different ways over the individual atoms of the molecule.

For the system under study, a complete filling of the F-LUMO state was found (indicated by its binding energy 0.62 eV below the Fermi edge [50]), i.e., a charge donation of 2 electrons into the molecule occurs. Assuming that this charging is not fully compensated by the back-donation effect, the charge q remains on the NTCDA molecule. In a first approach, it is assumed that the two electrons transferred into the LUMO are equally distributed over all atoms that are (spatially) located very close to a high LUMO density of states. That are all C and O atoms except those on the long symmetry axis of the molecule, as can be seen from the inset in Fig. 5.8 (a) showing a real space representation of the NTCDA LUMO. The back-donation is assumed to involve all atoms of the molecule (except the hydrogen atoms) equally, i.e., a total charge of $(2 - q)$ electrons are withdrawn from these atoms. For this scenario, PP calculations have been performed for values of q between 0.0 and 1.0 and for the geometries corresponding to the three adsorption sites A, B and C discussed above. The result is shown in Fig. 5.8 (a). The calculated pair potentials for an NTCDA molecule at the corresponding

positions are plotted versus the net charging of the molecule q.

It can be seen that without charging ($q = 0$) the smallest value for the pair potential energy is calculated for site A, i.e., this site is most favourable. However, the energy increases for all three sites with increasing q, i.e., the charging makes the attachment of the molecules to the existing island less favourable (as it can be expected since the molecules are equally charged). Since the latter effect is much weaker for site C compared to A and B, site C becomes the most favourable site above $q = 0.2$ electrons. At approx. 0.4 electrons, site C is the only one with a negative pair potential, and therefore represents the only energetically stable configuration, before at $q \approx 0.55$ electrons it also becomes unstable.

A possible shortcoming of these first calculations is that a *homogeneous* distribution of the charge surplus is not in good agreement with the NIXSW results [50]. They indicated a strong downward bending of the carboxylic oxygen atoms forming σ-like bonds to the substrate which must influence the charge distribution. In first approximation, one may argue that this leads to a charge accumulation in the vicinity of the carboxylic oxygen atoms. Therefore, a second parameter x is introduced describing the charge redistribution in the NTCDA molecule: The donation of a charge of 2 electrons into the F-LUMO is now not distributed equally: A variable fraction of x electrons is located at the carboxylic oxygens only while the remaining charge of $(2 - x)$ electrons is spread over the other carbon atoms that are located close to the FLUMO. The back-donation of $(2-q)$ electrons, and hence the net charging of the molecule q, remains unchanged. In Fig. 5.8 (b), the calculated pair potentials for this second scenario are plotted, again for all three sites A, B and C. A net charging of $q = 0.4$ electrons is assumed corresponding to the case when site C is clearly preferred over sites A and B. Note that an asymmetry parameter $x = 0.5$ corresponds to the case of a homogeneous filling of the FLUMO as considered in Fig. 5.8 (a), whereas for smaller (larger) values of x, less (more) charge is located on the four carboxylic oxygen atoms.

It can be seen in Fig. 5.8 (b) that in particular the sites A and C are influenced by the asymmetry parameter x while site B is hardly affected. This is due to a "quadrupole-like" arrangement of charge at those locations where carboxylic atoms of one molecule lie close to the hydrogen atoms of the neighboring molecules. These locations are marked with blue circles in Fig. 5.7 (a)-(c), the quadrupole-like arrangement is illustrated in Fig. 5.7 (d). This charge arrangement stabilizes the structures, and for site C it is the only next-neighbor interaction effect. For site A, the effect occurs even twice (on both sides of the attaching molecule) and it is therefore much stronger. But, it is counteracted by the fact that anhydride groups of opposing molecules are facing each other in a relatively small distance (blue arrows in Fig. 5.7 (a)-(c)). Hence, the slope of the pair potential curve is not significantly higher for site A than for site C. For site B, the effects caused by the quadrupole-arrangement of charge (occurring once, as in case of site C) and the opposing anhydride groups almost compensate each other, explaining the flat progression of the pair potential curve for this site.

It can be concluded that site C is, for all values of the asymmetry parameter x, the most favourable site (for $x < 1$ electron it is even the only stable configuration), as long as a net charging of the molecule q is in the range between 0.2 and 0.55 electrons. These numbers appear to be realistic in comparison to similar systems, for which calculations are available in literature (values of $q = 0.35...0.50$

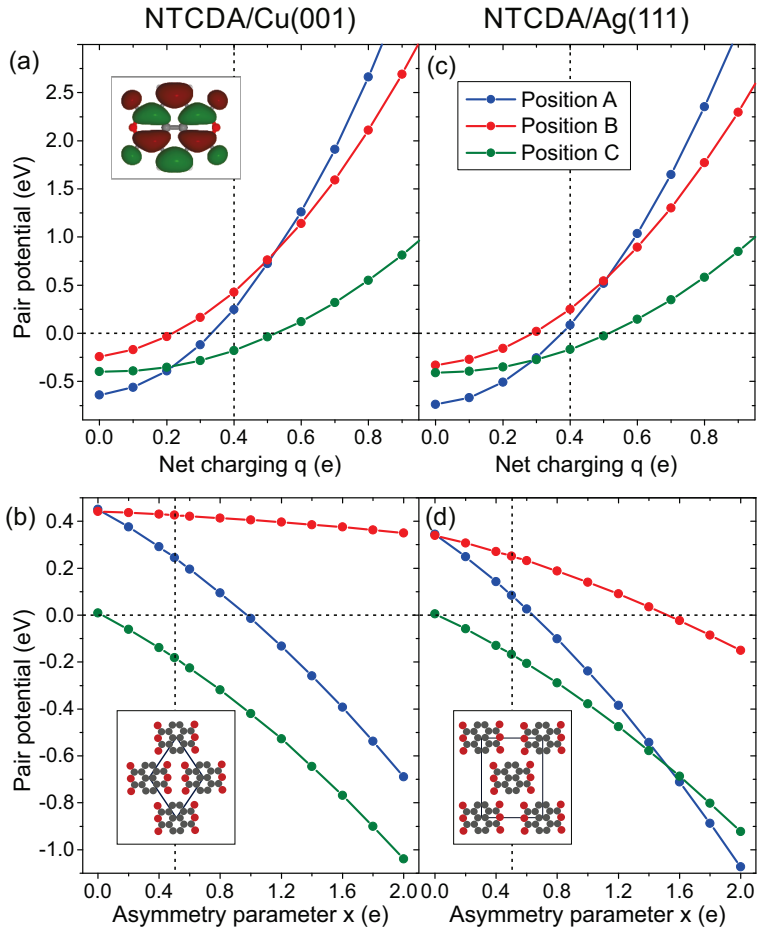

Figure 5.8: Calculated pair potentials for an NTCDA molecule attaching to an existing island at positions A, B and C. (a) Assuming an homogeneous filling of the FLUMO, the pair potentials are plotted versus the net charging q of the molecule. (b) For the case of a net charging $q = 0.4$ electrons, pair potentials are plotted versus the part x of this charge that is localized at the carboxylic oxygens atoms of the molecule. See text for more information.

electrons were reported for PTCDA and NTCDA on Ag and Cu surfaces, see above [1, 36, 125–128]).

Furthermore, the calculations for a varying asymmetry parameter x also indicate why similar systems (e.g., PTCDA or NTCDA on Ag(111) and Cu(111)) do not show fractal but compact island growth. This is demonstrated by comparing the system under study, NTCDA/Cu(001), with NTCDA/Ag(111). The structures found for both systems are very similar, the molecules arrange themselves in almost identical brickwall patterns (see insets in Fig. 5.8 (b) and (d)). Small differences in the size of the superstructure unit cells are responsible for slightly different distances between the molecules. But although these differences are small, the interaction of an attaching molecule and an existing island is influenced significantly, in particular the destabilizing repulsion between the anhydride groups. This is reflected by the pair potentials plotted in Fig. 5.8 (c) and (d) for NTCDA/Ag(111). While the charging q of the molecules yields very similar results for both systems (as to be seen from panels (a) and (c)), the asymmetric charging x (see panels (b) and (d)) does affect the two systems differently: Two relevant effects have been identified, the quadrupole-arrangement of charge, and the repulsion of the anhydride groups. The first is not significantly different for both systems, as revealed by the similar curves for site C (remember that the quadruple effect is the only interaction mechanism of molecules attaching to the island at site C). But, the different slopes of the curves for site B indicate that the repulsion of the anhydride groups cannot compensate the quadrupole effect in NTCDA/Ag(111) (whereas in NTCDA/Cu(001) it can). Hence, this repulsion is much weaker for NTCDA/Ag(111) which is consistent with the larger distance of neighboring molecules along their long symmetry axis. This leads to the fact that for site A, for which the quadrupole-effect occurs twice, the pair potential drops much faster with increasing asymmetry parameter x causing a crossing of the curves for sites A and C at $x \approx 1.5$. This means that site C, which for NTCDA/Cu(001) is clearly the most favourable site for all relevant values of x, becomes less favourable than site A for NTCDA/Ag(111) if the charge asymmetry on the NTCDA molecule exceeds $x = 1.5$. Since molecules attaching the existing island at site A are filling up voids in the structure, they cause a 2D compact growth of the island and clearly do not favour fractal growth. Finally, it should be mentioned that an asymmetry parameter of $x = 1.5$ represents a relatively moderate charge redistribution in the molecule. In numbers, when considering donation of 2 electrons into the LUMO with $x = 1.5$ (corresponding to an asymmetric distribution, 3 : 1 in favour of the carboxylic oxygens), and back-donation of 1.6 electrons (corresponding to a remaining total charge of 0.4 electrons on the molecule), the local accumulation of charge on each of the four carboxylic oxygen atoms is ≈ 0.3 electrons, and the depletion at all other atoms sums up to ≈ 0.04 and 0.08 electrons for the off-axis and on-axis atoms, respectively.

It can be concluded that small differences in the charge distribution, caused by only very small differences in the geometric arrangement of the molecules, may be responsible for fundamentally different growth modes since they are able to cause significant differences in the interplay of attractive (stabilizing) or repulsive (destabilizing) interactions for the different possible adhesion sites. In our case, such differences are able to explain that NTCDA exhibits fundamentally different growth behaviors on Ag(111) (compact, 2D islands) and on Cu(001) (dendrite-like

growth, well oriented 1D chains).

Finally, it should be mentioned that the PP calculations cannot be expected to yield quantitatively precise adhesion energies for the attaching molecules, but should rather be understood as a reasonable estimate of the involved potentials. More precise density functional theory or ab-initio calculations are definitely desired and should give more precise values. But on a semi-quantitative level, the PP results can explain the dendrite-like, fractal growth of NTCDA/Cu(001) found experimentally.

5.1.3 Summary

In summary, clear indications were found for a dendrite-like, fractal growth of NTCDA islands on Cu(001) in the submonolayer regime for temperatures at and above room temperature. The finding is based (i) on BF-LEEM measurements indicating that no compact islands occur, although the LEED pattern is well established already at small coverages, (ii) on DF-LEEM results showing a static domain shape and size during growth within almost the entire submonolayer regime ($\approx 0.2 - 1.0$ ML), and (iii) on RT STM images showing groups of elongated islands at low coverages, which seem to interact with each other since they are identically oriented within clusters of islands on the 100 nm scale. With the aid of valence band PES and NIXSW results revealing a relatively strong (chemisorptive) adsorbate-substrate interaction, the observed growth mode is explained using pair potential calculations. These calculations reveal that – under the specific conditions of net charge transfer into, and charge redistributions inside the molecule – one specific adsorption site is strongly favoured, which is responsible for the growth of long and thin molecular chains. These chains form a dendrite-like network spreading over the entire surface already at very low total coverages. Thereby, they "reserve" certain surface areas for its respective domain, which subsequently are just filled up by the molecules adsorbing additionally. This growth behavior is unexpected and unusual for such a "simple" adsorbate system as NTCDA/Cu(001). The pair potential calculations, which nicely explain the experiential observations, indicate that this behavior is caused by the distinct interplay of charge transfer into and reorganization inside the NTCDA molecule, and that small differences in the geometric structure and the charge redistribution inside the molecules can cause a fundamentally different growth behavior, as it was observed for NTCDA/Ag(111) and other systems.

5.2 Further details on the growth of NTCDA/Cu(001)

In this section, further details are given regarding the growth of NTCDA on Cu(001) at room temperature. First, full series of (bright-field) LEEM and LEED images taken during NTCDA deposition are shown. Then, additional details of the STM and XSW investigations performed by Markus Franke [50] are presented.

5.2.1 LEEM and LEED measurements during deposition

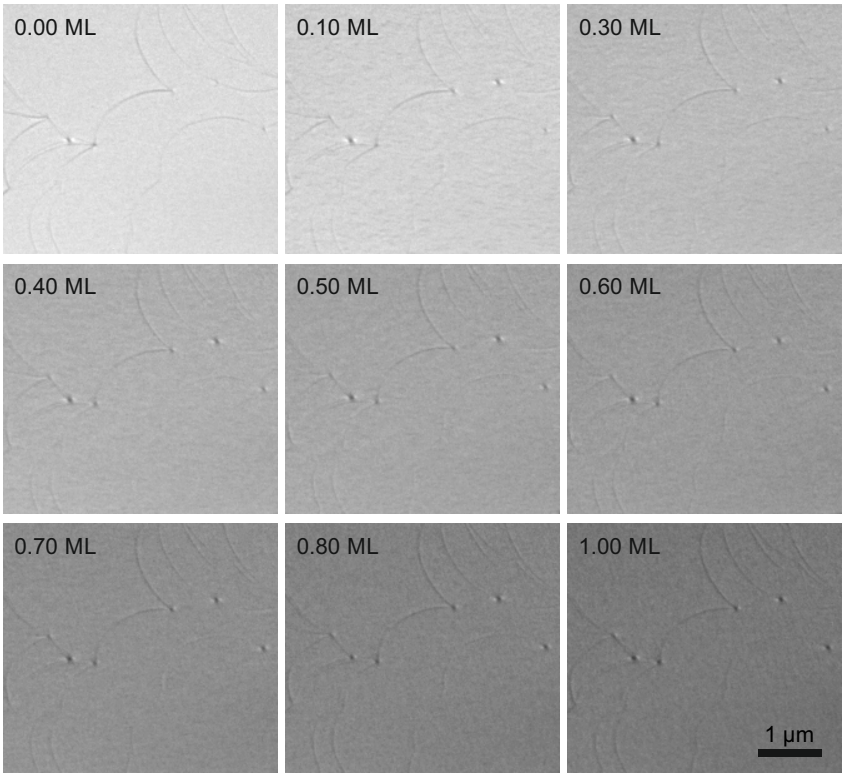

Figure 5.9: BF-LEEM images taken during deposition of the first layer of NTCDA on Cu(001) ($U_{\text{start}} = 2$ V).

The growth of NTCDA on Cu(001) has been studied in the coverage regime up to 2.0 ML using LEEM and LEED in real time during the deposition process. In addition to the selected images shown in section 5.1, full series of BF-LEEM and LEED images are presented here.

Figure 5.9 shows nine BF-LEEM images in the sub-monolayer regime. Beside step edges and point-like defects, no delimited details can be seen, only the overall intensity decreases with increasing coverage. This observation also holds for different focus settings (images not shown).

For coverages between 1 and 2 ML, the BF-LEEM images are shown in Fig. 5.10. The nucleation of the second layer can be seen in form of small dark islands growing larger and larger with increasing coverage. Hence, the second layer grows in form of compact NTCDA islands.

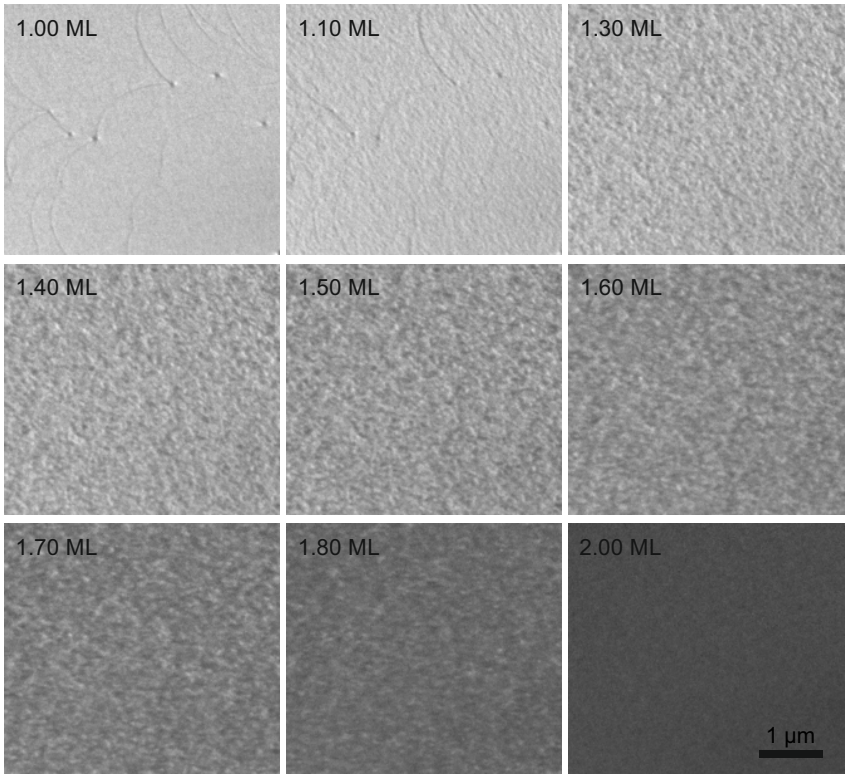

Figure 5.10: BF-LEEM images taken during deposition of the second layer of NTCDA on Cu(001). The start voltage is unchanged compared to Fig. 5.9 ($U_{\text{start}} = 2$ V) but the contrast of the images has been adjusted.

In Fig. 5.11, LEED images are shown taken during the deposition of the first layer of NTCDA on Cu(001). It can clearly be seen that a decent LEED pattern arises at ≈ 0.2 ML, and becomes sharper and more intense with rising coverage. While the LEED spots are elongated in the beginning, they become round indicating isotropic islands above ≈ 0.6 ML. The LEED pattern corresponds to the superstructure found by Fink et al. [44].

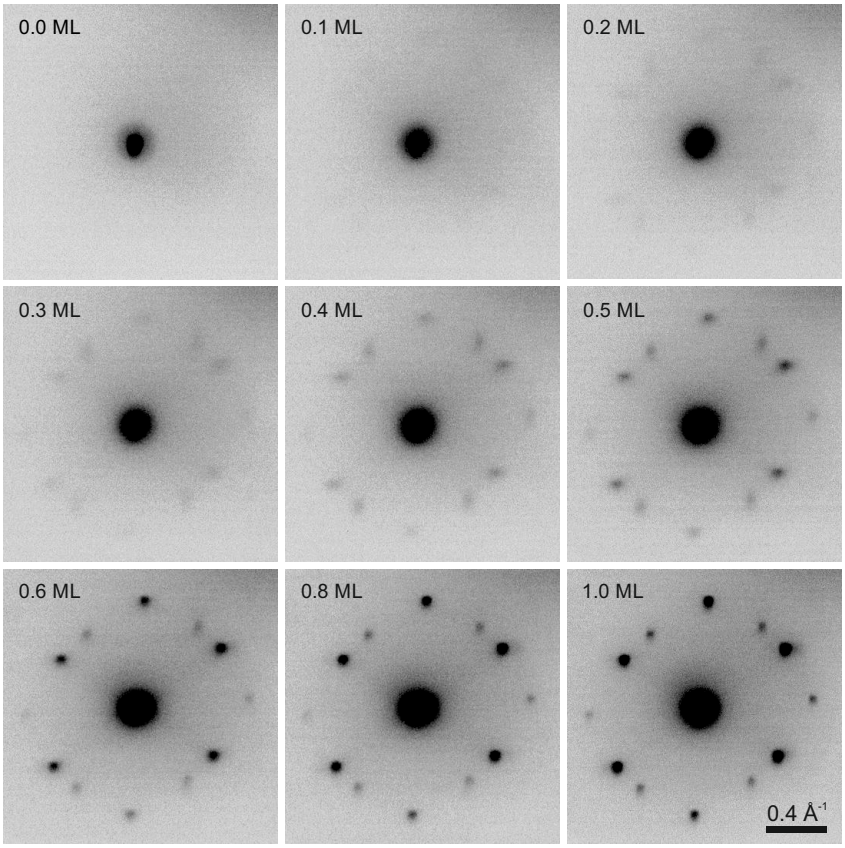

Figure 5.11: LEED images taken during deposition of the first layer of NTCDA on Cu(001) ($U_{\text{start}} = 7.5$ V).

5.2.2 Changes during consecutive STM scans

The stability of the NTCDA islands on Cu(001) have been tested by consecutive scanning of the same surface region for many times. In Fig. 5.12 (a)-(c), a series of such STM images done by Markus Franke [50] is depicted for a sample in the low submonolayer coverage regime. The molecular islands appear dark on a brighter copper surface. In the three consecutive images, only small changes are visible in the island size and shape, as exemplarily indicated by red and blue circles. As discussed in section 5.1, the orientation of the unit cell of the NTCDA structure is clearly correlated to the preferred growth directions of the islands, leading to elongated island shapes. In panels (d)-(f), the two possible domain orientations of the islands are indicated by colouring them in red and blue, and the contour of the domains is indicated by a black line, comprising several identically oriented islands. In the three consecutive images, these contour lines show only small changes due to repeatedly scanning this surface region. Hence, tip-induced or diffusion-related changes do occur to some extend but they are not significantly changing the shape of both individual islands and domain areas.

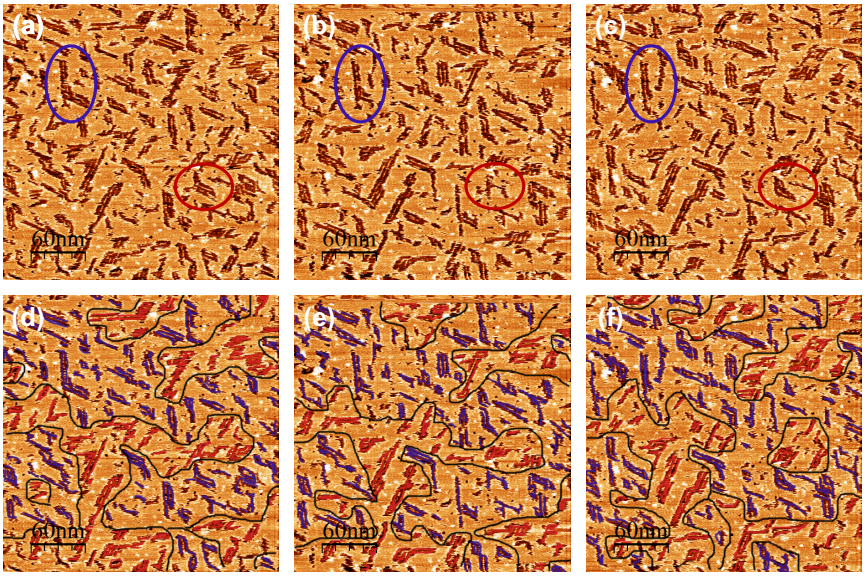

Figure 5.12: (a)-(c) STM images of a low coverage sample of NTCDA on Cu(001) recorded consecutively on the same area on the sample by Markus Franke [50]. (d)-(f) The islands are colour coded according to their domain orientation in red and blue, and black lines indicate the corresponding domain boundaries. ($V_{\mathrm{gap}} = -0.75$ V, $I_{\mathrm{tunnel}} = 0.03$ nA) This figure has been adapted from [190] with permission.

5.2.3 Treatment of non-dipolar effects in normal incidence x-ray standing waves

In XSW, non-dipolar effects usually cannot be neglected since rather high photon energies have to be used in order to fulfil the Bragg condition of the selected bulk Bragg reflection. Markus Franke [50] has performed the NIXSW data analysis within the so-called "dipole+quadrupole" approximation (for details see Bocquet et al. [17]). Within this approximation, the XSW yield curve is described (and fitted) by the equation

$$Y = 1 + S_{\mathrm{R}}R + 2|S_{\mathrm{I}}|\sqrt{R}F^H \cos(\nu - 2\pi P^H + \psi), \tag{5.1}$$

see eq. 46 in Ref. [17] and eq. 13 in Ref. [175]. Beside the reflectivity R of the Bragg reflection, the fit parameters coherent fraction F^H and position P^H, and the phase of the standing wave field ν, this equation contains the non-dipolar correction factors S_{R} and $S_{\mathrm{I}} = |S_{\mathrm{I}}| \cdot \exp(i\psi)$. Note that S_{R} and S_{I} depend on the angle ϕ between the incident synchrotron beam and the direction towards the analyser, and also on the angle 2θ between the incident x-ray beam and the Bragg diffracted beam (with θ being the Bragg angle). While in perfect normal incidence geometry $2\theta = 180°$, this value is never precisely realized in reality since the intensity of the diffracted beam must be recorded by any kind of detector, which then would block the incident beam. Although the deviation from perfect normal incidence is usually small, the effect is not negligible as demonstrated by van Straaten et al. recently [17, 175].

Alternatively, non-dipolar effects can also be parameterized by γ and Δ, which quantify the contribution of the emitted d-wave to the photoemission intensity and the phase difference between the emitted p- and d-waves, respectively. These parameters are independent from any geometry-specific angles and can be found in the literature. γ is tabulated in Refs. [169, 170] while Δ can be calculated using the NIST Software *Electron Elastic-Scattering Cross-Section Database v3.2* [78].

In conclusion, the non-dipolar parameters S_{R} and S_{I} used in eq. (1) are calculated from geometry-free parameters γ and Δ, and the angles ϕ and θ mentioned above. The corresponding relations can be found in Ref. [17], eqs. 84–88, and Ref. [175], eqs. 20, 21 and 23.

In Table 5.2, all relevant parameters are listed that have been used in the present study.

Table 5.2: Non-dipolar parameters and relevant geometry-specific angles used for the analysis of the NIXSW data in this work. Note that the value for ϕ is an averaged value since electrons in the range from $\phi = 60°$ to $90°$ are recorded by the analyser due to its large acceptance angle. ξ is used in Refs. [17, 175] and simply defined as $\xi = 90° - \theta$.

core level	γ	Δ	S_R	$\lvert S_I \rvert$	ψ	ϕ	θ	ξ
C1s	1.250	−0.18519	1.194	1.102	−0.024	75°	86.5°	3.5°
O1s	1.175	−0.25586	1.176	1.093	−0.032			

5.3 Momentum microscopy of a single domain

In this section, the prototype system NTCDA on Cu(001) is used for a proof of principle experiment, namely to demonstrate that momentum microscopy of a single domain of NTCDA is possible with the LEEM/PEEM instrument. First, a short motivation is given by explaining a common problem of high symmetric substrates in momentum microscopy. Then, the μARPES results of NTCDA on Cu(001) are discussed.

5.3.1 Motivation: PTCDA/Ag(111) and other high symmetric systems

Within the orbital tomography approach (as described in detail in chapter 2), the angular-resolved photoemission signal of a certain molecular structure is calculated in the plane wave approach. For a free PTCDA molecule, the resulting constant binding energy (CBE) maps for the HOMO and LUMO are depicted in Fig. 5.13 (a) and (e), respectively. However, different orientations of molecules on the surface can contribute to the angular intensity distribution. On Ag(111), PTCDA forms a herringbone structure which consists of two molecules per unit cell which are rotated by 77° [90] with respect to each other. Averaging the CBE maps for these two molecules leads to the maps for the HOMO and the LUMO as depicted in (b) and (f), respectively. Additionally, the symmetry of the substrates allows six domains of this herringbone structure. Consequently, twelve molecules with different orientations contribute to the CBE maps in (c) and (g). [123, 156] These theoretical maps correspond quite well to the measured maps shown in (d) and (h) which justifies the plane wave approximation for the final state. For this measurement, the large selected-area aperture was used in order to measure a large number of different domains simultaneously.
Although this system exhibits twelve differently orientated molecules, Stadtmüller et al. [156] have shown that the orbital tomography technique allows a meaningful analysis of the different local density of states and reveals different electronic structures for the two symmetrically inequivalent molecules in the unit cell of PTCDA/Ag(111) which are located at different adsorption sites with respect to the silver substrate. However, the quality of this linear regression fitting algorithm would be more reliable when the measured data correspond to just one

domain of the structure under investigation instead of six domains. Then, details would be much easier to distinguish. Especially, when the system becomes more complex for example by mixing two kinds of molecules, it becomes even harder to get information from the experimental maps (although it is still possible as shown for the mixed brick-wall structure of PTCDA and CuPc on Ag(111) [160]) and the need to measure certain phases or domains separately from each other increases. However, this is not possible with the usually applied methods since they are averaging the information of large areas on a sample.
This explains the need for an instrument that enables ARPES measurements on a small sample area, ideally from only one domain. In the following, it is shown that this is possible with our LEEM/PEEM instrument for the prototype system NTCDA/Cu(001). The selection of the region of interest can easily be done by DF-LEEM since this allows to identify the individual domains. Therefore, so called μARPES measurements of a single domain can be taken.

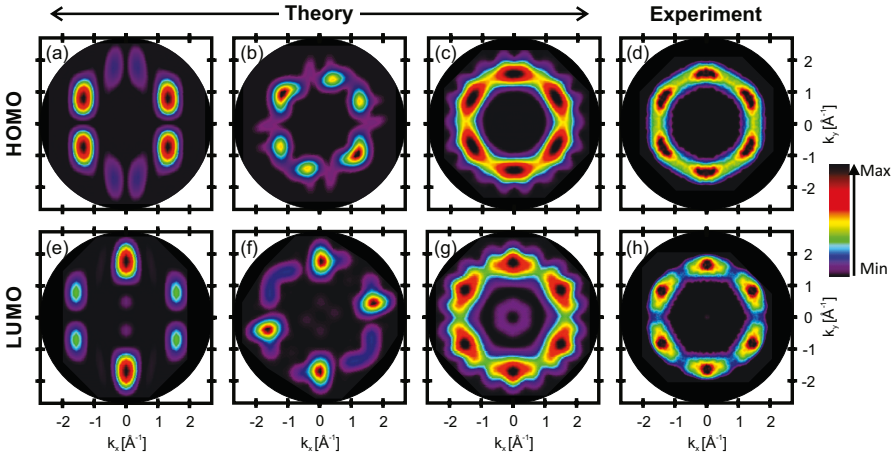

Figure 5.13: Calculated CBE maps for the HOMO and the LUMO of a free PTCDA molcule (a+e), of one domain of PTCDA/Ag(111) (b+f) and of PTCDA/Ag(111) when all six possible domains contribute (c+g). (d+h) Measured angular-resolved photoemission signals for HOMO (E_B = 1.6 eV) and LUMO (E_B = 0.3 eV) of PTCDA on Ag(111) with a large SA aperture. See text for more information. Calculations were performed by Daniel Lüftner, University Graz.

5.3.2 Single domain ARPES of NTCDA on Cu(001)

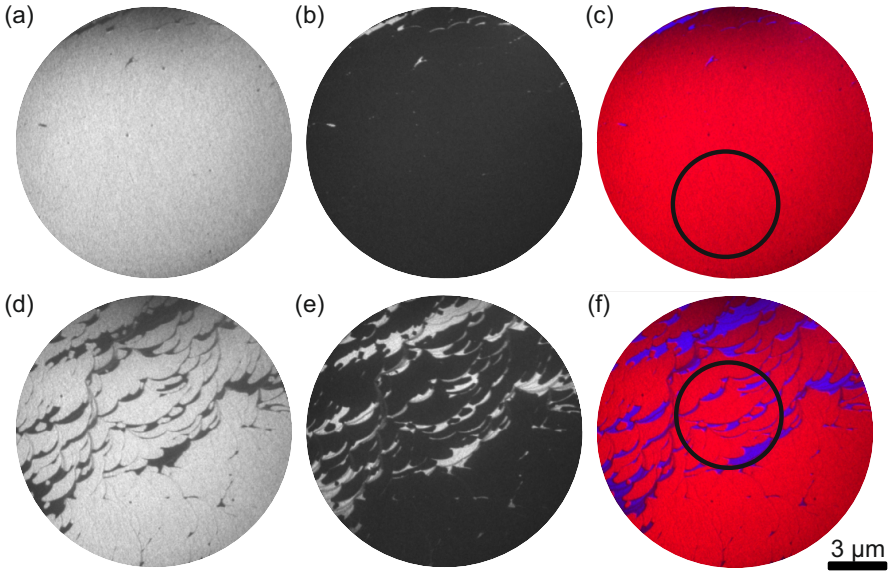

Figure 5.14: DF-LEEM measurements ($U_{\text{start}} = 2.4\,\text{V}$) of the prototype system NTCDA on Cu(001) for two positions on the same preparation (The same nomenclature and colour code as in the previous sections are applied.): (a)+(d) DF-LEEM of domain A. (b)+(e) DF-LEEM of domain B. (c)+(f) False colour image of the two domains for both areas (domain A in red, domain B in blue). The black circles represent areas chosen with the selected area aperture for μARPES.

For NTCDA on Cu(001), only two domain orientations emerge because of the substrate's symmetry. DF-LEEM measurements of these two domains are depicted in Fig. 5.14 for two areas of the same preparation. As can be seen, NTCDA forms very large domains on Cu(001). This is due to slightly elevated substrate temperatures during NTCDA deposition (here: 85°C). This makes it possible to use rather large selected area apertures in μARPES to choose only one domain of NTCDA/Cu(001) as it is indicated in 5.14 (c) with the black circle. This is the reason for choosing NTCDA on Cu(001) as prototype system to demonstrate momentum microscopy of a single domain.
NTCDA forms a commensurate, brick-wall structure with only one molecule per unit cell on Cu(001) [44, 168]. Therefore, the angular-resolved photoemission signal of the LUMO of one domain corresponds just to the signal of a free NTCDA molecule. The two domains of NTCDA/Cu(001) are rotated against each other by 90° as indicated in Fig. 5.15 (a) and (b) where the calculated CBE maps for the LUMO of both domains are depicted separately. In (c), the calculated CBE map of the LUMO is shown for the case that both domains contribute equally.
Figure 5.16 (a) shows the momentum microscopy measurement of a single domain NTCDA on Cu(001) for a selected area as depicted in Fig. 5.14 (c). This measurement taken at $E_B = 0.5\,\text{eV}$ is in very good agreement with the theoretical

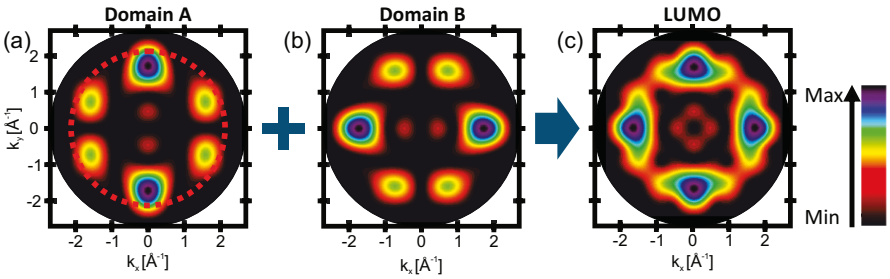

Figure 5.15: Calculated (done by Daniel Lüftner, University Graz) CBE maps of the LUMO of NTCDA on Cu(001) for (a) domain A, (b) domain B or (c) both domains. The photoemission horizon is indicated in (a) by a red circle. When a photon energy of about 21eV is used, only features within this red circle can be observed in a measurement.

map of domain A in Fig. 5.15 (a). Since the photon energy of the He-lamp is fixed to about 21eV, only features within the indicated red circle, the photoemission horizon, can be observed. All main features are very well visible. Definitely, no features of the other domain can be identified between the side lobes.

For comparison, a μARPES measurement is shown in Fig. 5.16 (b) recorded from an area where both domains contribute as indicated in Fig. 5.14 (f). In contrast to Fig. 5.16 (a), features of the second domain occur; in particular between the two side lobes of domain A, the main maxima of domain B are visible. They have a clearly lower intensity than the main maxima of domain A since domain B occupies much less space in the chosen area than domain A.

In summary, it was demonstrated that momentum microscopy measurements of a single domain are possible in the LEEM setup. This can potentially improve the results of orbital tomography by reducing the number of molecule orientations contributing to the measurement and to enable separate measurements of different structural phases coexisting on a sample.

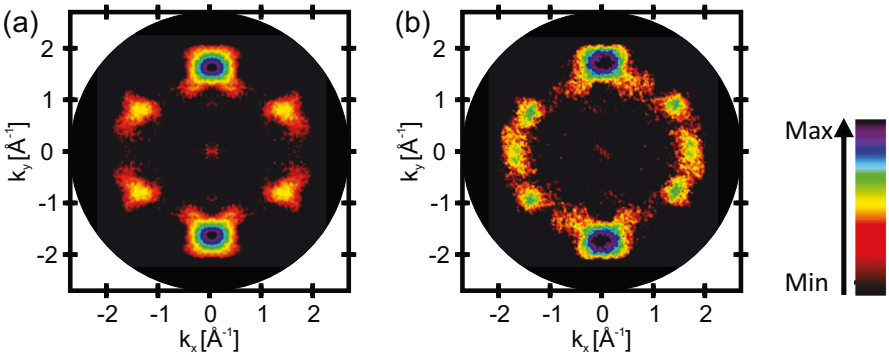

Figure 5.16: (a) Momentum microscopy measurement of a single domain NTCDA on Cu(001) at $E_B = 0.5\,eV$ for a selected area as depicted in Fig. 5.14 (c). (b) Momentum microscopy measurement at $E_B = 0.5\,eV$ for a selected area as depicted in Fig. 5.14 (f).

5.4 NTCDA on Cu(001): β-phase

In the previous three sections, the growth and structure of NTCDA on Cu(001) was investigated for substrate temperatures between 300 K and 370 K. The phase found in this temperature regime and discussed so far is called α-phase. At higher substrate temperatures, a new phase, the β-phase, is found which coexists with the α-phase and is discussed in this section. The majority of the LEEM and LEED analyses presented in this section was performed under my guidance in the framework of the Master's thesis of Jana Wolters. Here, only a short summary of the main results regarding the β-phase is given for reasons of completeness. For more details, please see [190].

In Fig. 5.17, a BF-LEEM image sequence recorded during NTCDA deposition on Cu(001) at a substrate temperature of 433 K is shown. In contrast to the α-phase, the β-phase can be seen in the BF-LEEM mode as islands with a dark contrast at $U_{\text{start}} = 2\,\text{V}$ (c). The β-phase islands nucleate exclusively at step edges and other defects (b). Additionally, its growth is restricted do the direct vicinity of the step edges and only step edges of a certain orientation are decorated with this phase. In contrast, step edges which do not have the "right" orientation seems to not allow the growth of the β-phase. On the rest of the surface, the LEEM intensity decreases with increasing coverage which is in good agreement with the observations made at lower substrate temperatures for the α-phase.
In Fig. 5.19 (a), the strongly elongated, needle-like shape of the islands is visible. Over the whole surface, only two island orientations are found which are orientated perpendicularly to each other. The island's orientation depends on the step edge orientation where the island nucleates.
The number of β-phase islands increases with increasing substrate temperature and, in particular, with increasing step edge density. It should be mentioned that the growth of a second monolayer NTCDA/Cu(001) was not observed at substrate temperatures above 370 K. The deposition was stopped when no changes were observed any more.

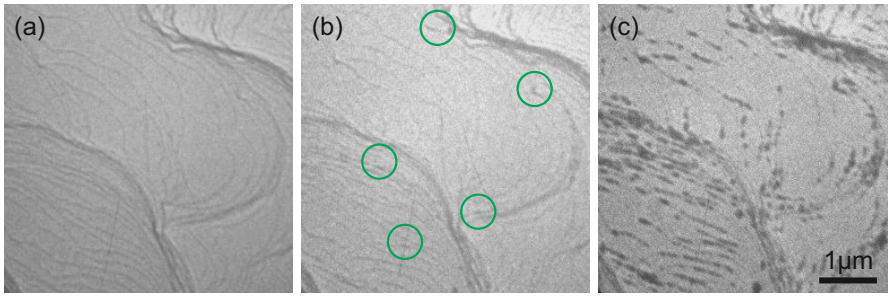

Figure 5.17: LEEM image sequence recorded during NTCDA deposition on Cu(001) at a substrate temperature of 433 K ($U_{\text{start}} = 2\,\text{V}$): (a) Clean surface before deposition. (b) Nucleation of the β-phase at the step edges indicated with green circles. (c) Growth of the β-phase. In contrast to the α-phase, the β-phase can be seen in BF-LEEM mode as islands with a dark contrast.

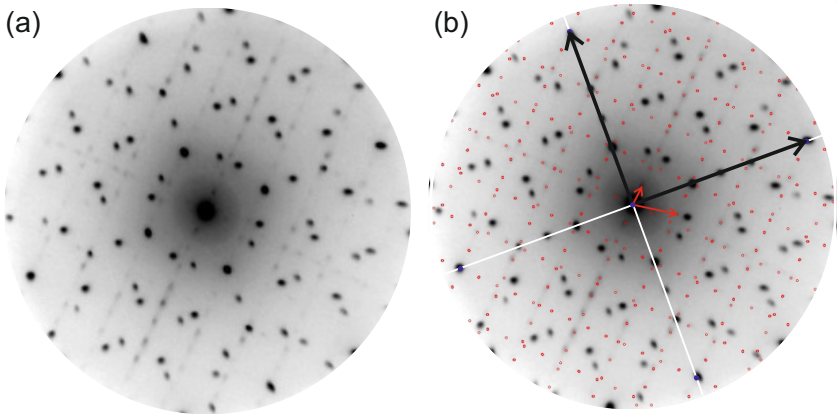

Figure 5.18: (a) Integrated LEED image from $U_{\text{start}} = 7.5 - 30\,\text{V}$ of NTCDA on Cu(001) deposited at 400 K. It corresponds to a superposition of two LEED patterns: α- and β-phase. The image was distortion corrected using the known superstructure of the α-phase. (b) The superstructure pattern belonging to the β-phase is shown according to the superstructure matrix M_β [190].

The LEED image in Fig. 5.18 (a) is taken from NTCDA deposited at 400 K on Cu(001). It corresponds to a superposition of two LEED patterns: The more intense LEED pattern is in good agreement with the α-phase. The additional less intense spots are attributed to the β-phase. This shows that the α- and β-phase coexist on the surface. In Fig. 5.18 (b), the pattern according to the superstructure matrix

$$M_\beta = \begin{pmatrix} 3.00 \pm 0.05 & -3.00 \pm 0.05 \\ 5.0 \pm 0.1 & 8.0 \pm 0.1 \end{pmatrix}.$$

is indicated as found by Jana Wolters [190]. It is in very good agreement with the measured LEED pattern (Fig. 5.18 (b)).
The lattice parameters of the β-phase are (24.1 ± 0.3) Å and (10.8 ± 0.2) Å and the unit cell vectors enclose an angle of $(103 \pm 3)°$. Therefore, the unit cell area is three times larger than the one of the α-phase. The LEED spots are elongated in the direction of the shorter reciprocal lattice vectors of both domains. This is in good agreement with the island shape observed in LEEM. The preferred growth direction of the needle-like islands can be attributed to the direction perpendicular to the longer real-space lattice vector.
The coexistence of the α- and β-phase was also studied with DF-LEEM. In Fig. 5.19, a BF-LEEM image (a) is compared with a false-colour image consisting of four DF-LEEM images of the same area (b). The whole area which is bright in BF-LEEM corresponds to the two DF-LEEM measurements of the α-phase indicated in red and blue. In contrast, the areas showing a darker contrast in BF-LEEM only appear in DF-LEEM for LEED spots of the β-phase (yellow and cyan). Therefore, we conclude that the β-phase is part of the first monolayer (no α-phase below).
In Fig. 5.19 (b), it can be seen that the β-phase islands of the same domain are

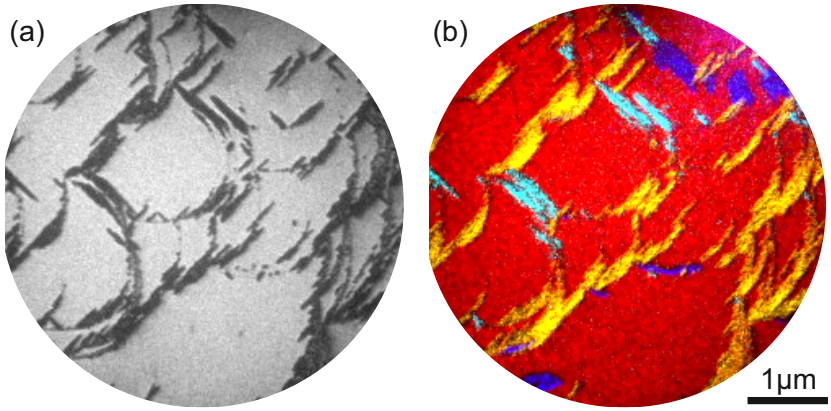

Figure 5.19: (a) BF-LEEM image at $U_{\text{start}} = 5.5\,\text{V}$ of NTCDA on Cu(001) deposited at 390 K. The β-phase has a darker contrast than the α-phase. (b) Composite image of four DF-LEEM images of the same area as in (a) ($U_{\text{start}} = 5.5\,\text{V}$): α-phase domain A (red) and B (blue), β-phase domain 1 (yellow) and 2 (cyan). Most of the area (especially on the terraces) is covered with the α-phase. The islands of the β-phase are only found in the direct neighbourhood of step edges. The domain orientation of the β-phase depends on the step edge orientation. Step edges which do not have the right orientation for the β-phase are decorated with the α-phase.

orientated parallel to each other. Therefore, the domain orientation and also the island shape depends on the step edge direction where the islands have nucleated.

In summary, we found a second phase of NTCDA on Cu(001) for deposition at substrate temperatures above 370 K coexisting with the α-phase. This β-phase forms elongated islands which are visible in BF-LEEM and exhibit only two orientations that are perpendicular to each other. Their growth is restricted to the direct neighbourhood of step edges. The rest of the surface is covered with the α-phase, the properties of which are discussed in the two previous sections. No second layer is observed in this temperature regime. The domain orientation and the island shape of the β-phase depends on the step edge orientation where the island nucleates. Step edges, which do not have the right orientation for the β-phase, are decorated with the α-phase. The LEED pattern indicates that each domain nucleates with the long unit cell vector perpendicularly to the step edges and that the unit cell area is three times larger than for the α-phase.

Therefore, it can be concluded that three NTCDA molecules are located within one unit cell if the molecules are lying flat on the surface. However, it is hard to find a plausible real-space model with three flat lying molecules in this unit cell. A configuration of upright-standing (or at least not completely flat lying) molecules might be reasonable to explain why this phase only occurs at step edges. Although this might be a rather uncommon behaviour for planar molecules, a phase of upright-standing NTCDA molecules has already been found on the Ag(111)-surface by Braatz et al. [19]. Hence, this question remains without an unambiguous answer based on the data available.

Chapter 6

hBN on Cu(111)

Hexagonal boron nitride (hBN), often entitled the "white graphene", is a prominent and frequently studied member of the family of two-dimensional (2D) materials. It forms a hexagonal honeycomb structure of nitrogen and boron atoms, similar to graphene. Due to its structural and electronic properties, in particular its insulating nature (direct band gap of 5.97 eV [184]), it is of highest interest as part of hetero-epitaxial systems in conjunction with other 2D materials (so called van der Waals heterostructures) or organic thin films [55, 193]. However, the production of high quality hBN monolayers and organic thin films on hBN necessitates a deep understanding of nucleation and growth of these materials.
Single hBN layers are typically produced either by mechanical ex-foliation of single crystals [31] or in-situ via a catalytic process on the hot metal surfaces by dissociation of borazine or other precursors [30, 86, 98, 120, 144, 151, 152, 161]. Especially, the latter has a high potential as scalable method and guarantees the lowest level of contaminations. The growth of hBN via chemical vapour deposition was studied on several metal substrates. Generally, the degree of reactivity of the substrate has strong influence on the growth rate and on the morphology of the hBN layer [7, 21, 30, 112, 122, 137, 161]. For highly reactive metals, strongly corrugated and buckled films were found while with decreasing reactivity the films become more flat and weakly bonded to the substrate. This weak bonding could be very important for processes where the substrate has to be etched away for further device production and, additionally, could lead to the decoupling of molecular adsorbates on hBN from the metal states [138].
The Cu(111) surface has been recently shown to exhibit a rather weak hBN/metal interaction. Using scanning tunneling microscopy (STM), Joshi et al. [80] found a Moire-like superstructure caused by the lattice mismatch between the substrate and the hBN layer. However, this pattern occurs only at certain, relatively high bias voltages indicating that it is not caused by a geometric vertical height modulation but results from electronic contrast. This finding is supported by x-ray standing waves (XSW) results of Brülke et al. [21]. These authors found relatively large bonding heights for nitrogen ($d_{\mathrm{N}} = 3.25\text{Å}\pm0.02\text{Å}$) and boron ($d_{\mathrm{B}} = 3.22\text{Å}\pm0.03\text{Å}$), no significant vertical buckling of the hBN layer and no indications of lateral distortions. Additionally in high resolution spot profile analysis low energy electron diffraction (SPA-LEED), they found various azimuthal orientations of hBN domains with respect to the substrate which is also an indication for weak substrate bonding.

In this chapter, the same system, hBN on Cu(111), is investigated particularly with regard to its growth in the submonolayer regime. In the first two sections, the results for high substrate temperatures (1020-1100 K) are discussed including the influence of step edge mobility, the hBN domain formation, shape and orientation, and a fractal, dendrite-like growth pattern exhibiting a three-fold symmetry. Additionally, a growth model is presented which correlates the experimental findings with each other and explains the extraordinary island shape of hBN on Cu(111).
Finally, the influence of the substrate temperature on the growth, structure and growth rate of hBN on Cu(111) is discussed briefly in the third section.

Shortly after the submission of this thesis, the content of sections 6.1 and 6.2 was published in [42].

6.1 hBN on Cu(111) at high temperatures

In this section, the growth of hBN on Cu(111) prepared at high substrate temperatures (1020-1100 K) are investigated. Higher substrate temperatures were not chosen in order to avoid an accidentally melting of the crystal. First, the nucleation of hBN islands and the influence of the step edge movement are discussed. In the following, the growth rate is analysed to show the self-limiting growth of hBN on Cu(111). Thereafter, the domain structure is studied with μLEED and DF-LEEM. Subsequently, the observed growth mode of hBN/Cu(111) is described in detail. Most prominently, fractal, dendrite-like structures with three strongly preferred growth branches are observed which exhibit a three-fold symmetric shape. This dendrite-like growth is finally explained by a growth model which correlates the experimental findings with each other. This model is based on an asymmetry of the bonding energy for the two possible ways a borazine molecule can attach to an existing hBN island, namely either with one of its boron or one of its nitrogen atoms. It is suggested that this asymmetry originates from different dehydrogenation states of the adsorbed borazine molecules and the hBN islands.

6.1.1 Nucleation

The nucleation and growth of the hBN layer is studied with BF-LEEM in several growth series *in-situ* and in real time. Two exemplary images series are shown in Fig. 6.1 and 6.2. Note that all time stamps in this chapter give the growth time after the nucleation of the first observed hBN island. A general finding is that no preferred nucleation site could be identified unambiguously but that islands nucleate on both the clean and flat Cu(111) surface terraces and at all kinds of defects including point-like defects and, in particular, step edges. It should be mentioned that step edges, which in many systems represent preferred nucleation sites, are moving across the surface in this case. The high temperatures (1020 - 1100 K) that are necessary for growing hBN let Cu atoms desorb from the surface evidently preferably from the steps which makes the step edges move across the surface. Figure 6.1 shows an example. The step edge is marked with a yellow dotted line. Panel (c) shows that it is pinned by an hBN island in the center

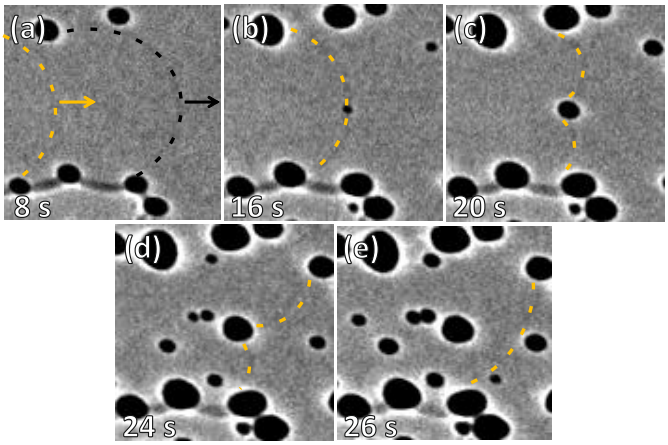

Figure 6.1: Step edge pinning by a nucleating hBN island: The size of the islands is strongly enhanced because of the chosen imaging conditions ($U_{\text{start}} = 0.8\,\text{V}$, underfocus). (a) Two copper step edges marked in yellow and black are moving from left to right. (b) An hBN island (dark contrast) nucleates in the middle of the image close to the step edge marked in yellow. (c+d) This island pins the step edge which bends around the island. (e) When the step edge encloses the island completely, it is able to pass and move on. (FOV 2.5 µm, 1067 K, 4.5×10^{-7} Torr)

of the image (dark island nucleating in panel (b) and quickly growing in size in (c)-(e)). Note that in the chosen imaging conditions ($U_{\text{start}} = 0.8$ V, underfocus) the step edges can be imaged but the island size is strongly overestimated (see section 6.2.1 for more details). The step edge bends around the island (panel (c) and (d)) until the lower terrace is enclosing the entire island. Then, the step edge is moving on (panel (e)). A similar behavior was observed for step edges passing point defects before the nucleation of hBN started.

Due to the overestimated island size in underfocus condition, the surface appears to be covered completely with hBN long before the layer is actually closing. Therefore, the movement of step edges cannot be observed any more at higher hBN coverages (see section 6.2.1 for more details). But it is assumed that the movement of step edges continues until most of the surface is covered, i.e., until a very high density of pinning centers is present just as it is the case for metal crystals with a high density of defects. In conclusion, it is found that nucleating hBN islands influence the movement of step edges across the surface, but reversely, the moving step edges have no significant influence on the growth of the hBN islands.

6.1.2 Growth rate

In Fig. 6.2, a series of LEEM images shows the growth of hBN on Cu(111) at 1085 K and a borazine pressure of 2.6×10^{-7} Torr. In contrast to Fig. 6.1, the imaging conditions are changed to slight overfocus and $U_{\text{start}} = 2$ V. This inverses the contrast so that hBN islands appear bright on the dark Cu(111)

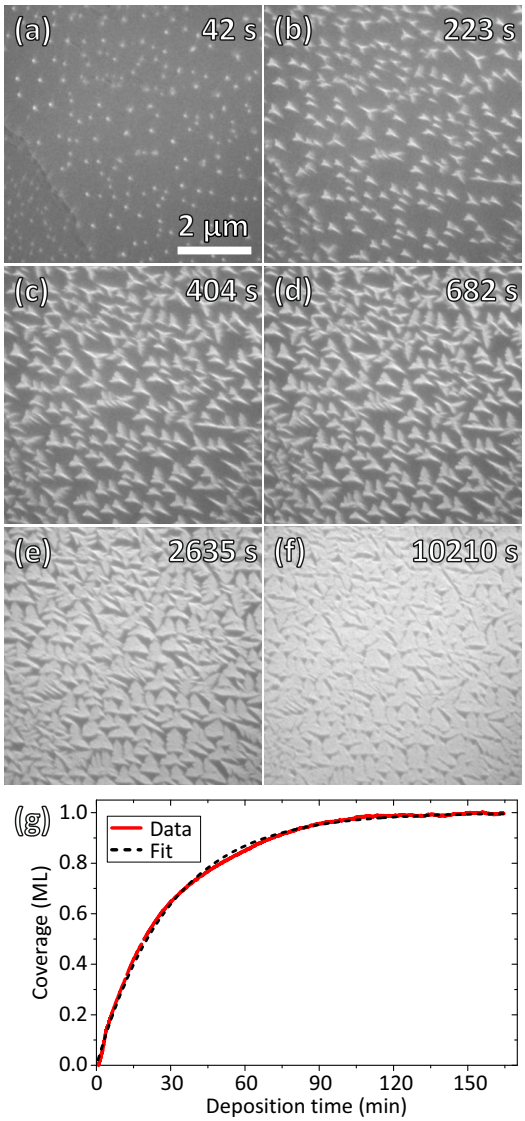

Figure 6.2: (a)-(f) BF-LEEM images recorded during the growth of hBN on Cu(111) at 1085 K and a borazine partial pressure of 2.6×10^{-7} Torr (U_{start} = 2 V, slight overfocus). (g) hBN coverage for a similar experiment (1015 K, 2.5×10^{-7} Torr.), as obtained from the total LEEM intensity plotted versus deposition time (red line). The data is fitted using a simple exponential relation (black dashed line, see text).

surface. Their apparent size and shape are now close to reality. Step edges are no longer visible under these imaging conditions. From the time of nucleation, the islands appear to be fractal and show triangular contour lines as discussed in the following sections in detail. From the image series in Fig. 6.2, which is recorded at constant substrate temperature and partial borazine pressure, it can clearly be seen that the growth rate is significantly decreasing with deposition time and increasing coverage. Under these imaging conditions, the total coverage can be well quantified by measuring the integrated intensity of the entire LEEM images. This is even true for small changes in the focus settings, as shown in more detail in section 6.2.1. In Fig. 6.2 (g), the total coverage, as obtained from the integrated LEEM intensity, is plotted versus the deposition time for a growth experiment performed at very similar conditions (1015 K and 2.5×10^{-7} Torr). The resulting curve is shown as a red line and can be fitted very well using

$$A(t) = 1 - e^{-\frac{t}{\lambda}} \tag{6.1}$$

which indicates that the growth rate $\frac{d}{dt}A$ is proportional to the uncovered surface area $(1 - A)$ (A represents the hBN covered surface area) [70, 111, 117, 161]. Therefore, it can be concluded clearly that the clean and hot Cu surface is necessary for the reaction of borazine to hBN to take place, leading to a self-limitation of the growth of hBN on Cu(111). A similar behavior was found for hBN on Ni(111) [7], Ag(001) [111], Cu(110) [70], Pt(111) [199], Ir(111) [117, 118] and Ru(0001) [161].

6.1.3 Domain structure

For investigating the structure of the individual domains of hBN on Cu(111), μLEED and DF-LEEM are applied. Figure 6.3 depicts a μLEED image of an hBN layer on Cu(111) close to one monolayer coverage. A modulated ring of diffraction intensity is clearly visible which appears to run through the LEED spots of the Cu bulk crystal. However, utilizing the high k-space resolution offered by SPA-LEED, Brülke et al. detected that this is not the case. The ring is slightly larger than the hexagon of the bulk spots, and intensity stemming from the hBN layer can be identified both directly next to the substrate spots as well as all along the ring [21]. While the latter stems from a continuous (although not equal) distribution of rotated islands having various azimuthal orientations, the much more intense LEED spots close to the first order Cu spots are explained by hBN islands that are aligned with the substrate. The strongly preferred azimuthal orientation of these aligned islands and their lattice mismatch of 2.2% at 300 K with respect to the Cu substrate are discussed in detail by Brülke et al. [21]. A closer look at our data (see section 6.2.2) confirms all of these findings.

DF-LEEM allows us to investigate the distribution of islands with various azimuthal orientations in more detail. By inserting an aperture in the beam path, a certain single LEED spot can be selected for imaging, e.g., the (10) spot which is marked by a blue circle in Fig. 6.3. In the corresponding DF-LEEM image depicted in Fig. 6.4 (a), only those parts of the surface appear bright that contribute to this LEED spot. Note that the blue and the red marked spot in Fig. 6.3 are the (10) and (01) reflections of the aligned hBN islands. Due to the three-fold symmetry of the hBN structure, these reflections are inequivalent

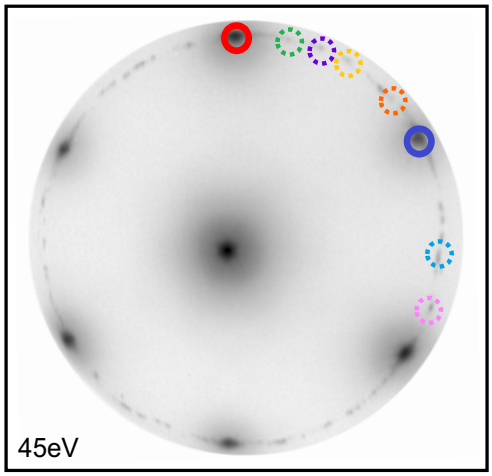

Figure 6.3: μLEED pattern of an almost closed monolayer hBN on Cu(111) at $U_{\text{start}} = 45\,\text{V}$. A modulated ring of LEED intensity is visible, stemming from differently rotated hBN domains, and relatively sharp spots close to the Cu(111) spots from aligned domains with a strongly preferred azimuthal orientation. The spots used for the DF-LEEM images in Figs. 6.4 and 6.5 are marked by solid and dashed circles, respectively.

and therefore visible with different intensities (see section 6.2.2 for more details). However, the six-fold symmetry of the uppermost substrate atomic layer also allows the formation of a second type of aligned hBN islands which are rotated by 60° with respect to the first. As can be seen from Fig. 6.4 (d), this rotation corresponds to an exchange of nitrogen and boron atoms. Since both types of islands are coexisting on the surface, the superimposed intensities of the (10) spot of the first and the (01) spot of the second type of aligned domains are found at the blue marked spot in Fig. 6.3, and vice versa for the red spot. In other words, both spots contain some intensity from both aligned domains, but with a different ratio of intensities, and therefore these spots can be used to identify the two different types of aligned domains in DF-LEEM, as discussed in the following.

In Fig. 6.4 (a) and (b), DF-LEEM images using the (10) and (01) spot (blue and red circles in Fig. 6.3), respectively, are depicted. Hence, in these two DF-LEEM images the two types of the aligned domains are visible. In panel (c), a false-colour image is presented with the two DF-LEEM images coloured blue and red, and superimposed on a BF-LEEM image having the same field of view. One can clearly see that the aligned domains are the majority domain structures. Both types show a distinct triangular shape (illustrated by white triangles) which are also rotated by 60° (resp. 180°) with respect to each other. The fact that the relative rotations of atomic structures and contour shapes of both types of domains are identical, suggests that this triangular shape is due to a preferred island edge termination with one of the two atomic species. In Fig. 6.4 (e), this is illustrated for a compact island terminated by "red" atoms (without an assignment of the two species) which allows the edges to be oriented in only three directions explaining the triangular island shape. Rotating the structure by 60° (or 180°),

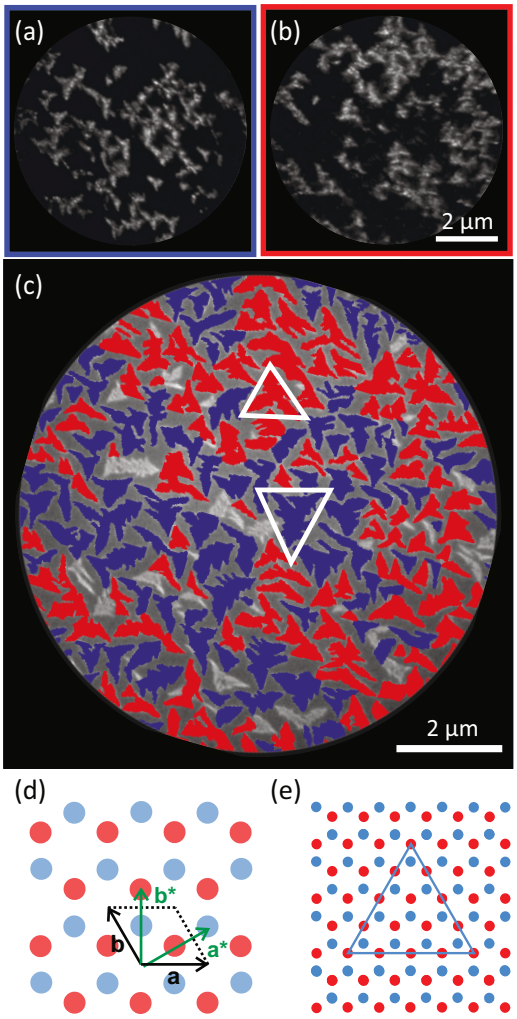

Figure 6.4: (a,b) DF-LEEM images of the two types of aligned domains of hBN on Cu(111), grown at 1025 K and 1.0×10^{-7} Torr ($U_{\text{start}} = 45$ V). LEED spots used in DF-LEEM are marked with blue (a) and red (b) circles in Fig. 6.3. (c) LEEM image of the same field of view ($U_{\text{start}} = 2$ V). Aligned islands of both types, as identified by DF-LEEM in panels (a) and (b), are coloured blue and red, respectively. All islands show a preferred triangular shape, as illustrated by white triangles. (d) Sketch of the hBN structure in real space. The two types of atomic species are shown in blue and red, without an explicit assignment of the species (see text). Unit cell vectors in real and reciprocal space are indicated in black and green, respectively. (e) Illustration of a compact hBN island terminated by one specific species (the red atoms in this case) which causes a triangular island shape.

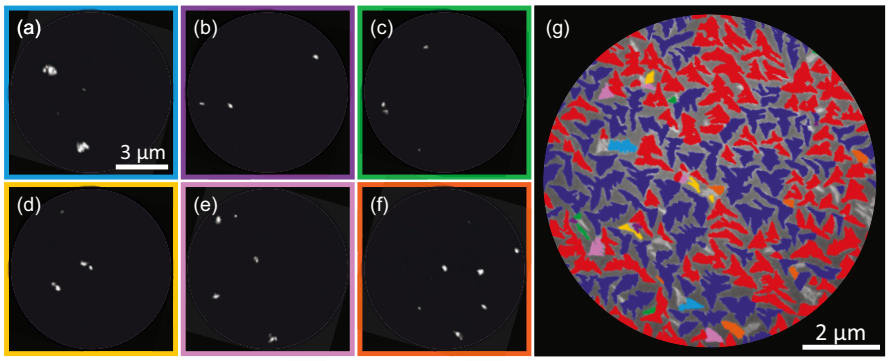

Figure 6.5: (a)-(f) DF-LEEM images of rotated hBN domains on Cu(111) (same growth conditions as in Fig. 6.4). Six different aperture positions along the diffraction ring were selected, as indicated in Fig. 6.3 by dashed circles in the corresponding colours. (g) False colour illustration of all domains discussed so far. The corresponding DF-LEEM images are shown in panel (a)-(f), and in Fig. 6.4 (a) and (b). The remaining (gray) domains correspond to other aperture positions along the diffraction ring, i.e., to other domain orientations. (FOV 10 µm)

also rotates the orientations of the triangles, assuming that the termination (red atoms) is conserved. Similar arguments were discussed in the literature without agreement on the terminating species (Refs. [8, 99] suggest N-termination, Ref. [40] B-termination). However, note that in this case the triangular islands are not compact but rather show dendrite-like growth. This is discussed in detail in the next section.

In Fig. 6.4 (c), about 95 % of the islands belong to one of these aligned domains indicating that this is the strongly preferred orientation of islands. However, even the aligned domains show a (rather narrow) azimuthal distribution (see section 6.2.2). Additionally, there are the rotated domains which are visible as gray (uncoloured) areas in Fig. 6.4 (c). These islands also have a triangular shape and show a slightly different contrast in BF-LEEM compared to the aligned domains (see section 6.2.2 for more details). The latter might indicate a different interaction with the substrate. These rotated islands can also be identified in DF-LEEM for aperture positions along the diffraction ring. In Fig. 6.5, this is shown for six exemplary positions. The individual DF-LEEM images are shown in panel (a)-(f), the corresponding false colour image is depicted in (g). The corresponding aperture positions are indicated in Fig. 6.3 (dotted rings in the same colour code). All other domains (i.e., those not coloured in Fig. 6.5 (g)) correspond to other positions on the diffraction ring.

These findings are in excellent agreement with the work of Brülke et al. [21]. The reason for a much stronger modulation of the diffraction ring in the μLEED images compared to the SPA-LEED image (Fig. 1 in [21]) is the illuminated surface area. In our case, this area is below 20 µm^2 but in the case of SPA-LEED measurements the illuminated area is in the mm^2-range. Therefore, the μLEED image shows a much smaller selection of domain orientations compared to the SPA-LEED image [21]. In conclusion, it can be stated that the diffraction ring

is formed by several islands with various azimuthal orientations (continuously, but not equally distributed) that can be well localized in DF-LEEM. The clear majority of domains, however, is well aligned with the substrate. They fall into two groups, with their lattices oriented 0° and 60° with respect to the substrate lattice.

6.1.4 Preferred growth directions

Now, the growth of individual hBN islands is discussed. Figure 6.6 (a)-(d) shows enlarged LEEM images recorded during growth. It can clearly be seen that the islands grow in three preferred directions having an angle of 120° with respect to each other. In the lower left, one of the rare exceptions is shown, an island with four growth branches caused by a surface defect. These main branches grow quickly in length until they approach the branches of the neighboring islands. Then, side branches start to grow diverting backwards from the main branches, again under an angle of 120°. A schematic illustration of this growth mode is depicted in Fig. 6.6 (e).

Since the LEEM instrument enables to directly correlate growth directions (in real space) with the orientation of LEED patterns (directions in reciprocal space), it is possible to unambiguously identify the crystallographic growth direction of these hBN branches. (Note that it is not trivial to correlate direct and reciprocal space directions in LEEM since changing the magnetic field of electromagnetic lenses in the electron optics, which is necessary to switch from diffraction to

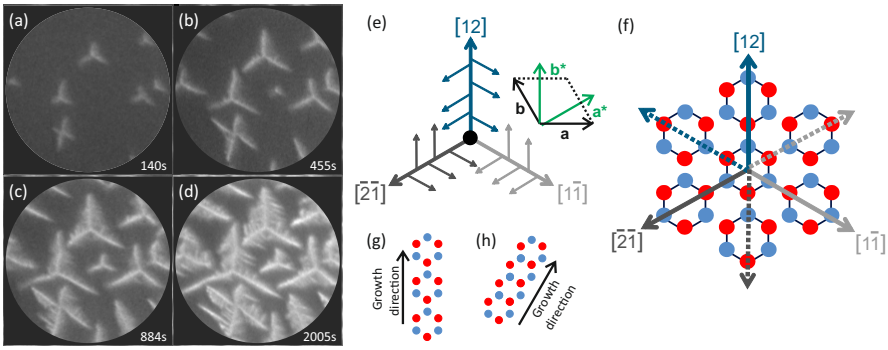

Figure 6.6: (a)-(d) BF-LEEM images showing the fractal growth of hBN islands (FOV 3.5 µm, start voltage 2 V, slight overfocus, temperature 1035 K, partial borazine pressure 0.5×10^{-7} Torr): Main branches grow in three preferred growth directions with an angle of 120° relative to each other. When they approach neighboring islands, side branches start to grow diverting backwards from the main branches, again under an angle of 120°. (e) Schematic representation of the fractal growth. The three preferred growth directions are given in real space coordinates, corresponding to (01), (0$\bar{1}$) and (1$\bar{1}$) directions in reciprocal space. (f) Growth via three of the hexagon corners (solid arrows) is preferred over the other three hexagon corners (dotted lines) and the hexagon sides. (g) Illustration of the growth of hBN in the directions of the corners of the hexagon and (h) via its sides.

image mode, does also rotate the observed image. All images shown in section 6.1 and 6.2 are corrected for this rotation effect. For details see section 6.2.3.) As a result of this analysis, the three preferred growth directions are identified as [1 2], [$\overline{2}$ $\overline{1}$] and [1 $\overline{1}$] in real space (corresponding to (0 1), (0 $\overline{1}$) and (1 $\overline{1}$) in reciprocal space), as illustrated in Fig. 6.6 (e) and (f). This demonstrates that the growth via three of the six corners of the hBN hexagon is preferred over all other directions (solid arrows in Fig. 6.6 (f), see also panel (g)), in particular over the other three hexagon corners (dotted lines), and over the sides of the hexagon (Fig. 6.6 (h)). Comparing Fig. 6.6 (g) and (h) shows that growth via the corners does not require the destruction of the B_3N_3 hexagon during the growth process but allows to attach the intact borazine molecule (after some dehydrogenation), in contrast to a growth via the hexagon sides.

6.1.5 Growth model

The growth of fractal islands, as observed for the system under study, is usually discussed in terms of diffusion-limited aggregation (DLA), a model at first discussed by T.A. Witten and L.M. Sander in 1981 based on computer simulations [189]. It applies to any system where the transport of the structure forming objects (molecules, in this case) is dominated by diffusion, and where the objects adhere to an existing structure as soon as they approach it to a certain level (often entitled "hit-and-stick"). DLA is of course extensively discussed in the literature, a good overview is given in the textbook by T. Michely and J. Krug [110]. Usually, in its simplest form, DLA determined structures are randomly oriented and their branches do not show any preferred growth direction or orientation [189]. Some exceptions to this rule are also discussed by Michely and Krug although for hetero- and homoepitaxial growth of *atomic* layers only. In the case of hBN/Cu(111), it has to be dealt with molecular adsorbates and, as discussed above, strongly preferred growth directions rather than randomly oriented branches are found. Therefore, while DLA certainly plays an important role in the formation of the fractals, other effects must be influencing the growth which are responsible for the three-fold symmetry observed in this study.
The most remarkable observation is that only three (not six) main growth branches occur forming three-fold symmetric islands of the growing hBN fractals. This is unexpected since all six possible directions (those across the corners of the B_3N_3 hexagon) appear to be equivalent, as illustrated in Fig. 6.6 (f). (Note that growth across the sides of the hexagon was already excluded above.) This is valid for all types of domains, in particular for the two aligned domain types but also for the rotated domains. One seemingly obvious reason for this observation might be the substrate, simply because the Cu(111) surface is also three-fold symmetric, only the structure of the uppermost Cu layer has six-fold symmetry. Consequently, as soon as the second bulk layer plays a role in the interaction between hBN islands and the substrate, one might expect a three-fold instead of a six-fold symmetric pattern for the hBN domains. However, in such a case, it would be unexpected to observe *two* aligned domains, since the atomic arrangement for the main branches of the second, 60° rotated domain would be identical to that of the suppressed branches of the first domain. This suggests that the reason for the three preferred growth directions lies in an interaction mechanism within the hBN layer, not in

the symmetry of the substrate.

The experimental finding that growth along the dashed and solid arrows in Fig. 6.6 (f) are not equivalent can be broken down to an asymmetry in the adhesion energy of a borazine molecule attaching with one of its B (or N) atoms to an N (or B) atom of the existing hBN island. This is illustrated in Fig. 6.7 (a): The blue-filled molecule labeled "i" (island) represents the last one of a branch of the already existing hBN island growing towards the lower left. Molecule "1" attaches with its "red" atom to a "blue" one of the existing island while molecule "2" bonds with a "blue" atom to a "red" one of the island. The conclusion from the experimental findings is that the first scenario is the preferred one while the second is strongly suppressed, i.e., the branch continues growing straight to the lower left rather than bending by 60°. Please note that in this work it cannot be unambiguously identified which of the blue and red molecules correspond to the boron or nitrogen species.

The assumption of such an asymmetry in the adhesion energy can fully explain all observations: First, in addition to the three main branch directions, also the growth directions of the side branches can be explained. In the sketch shown

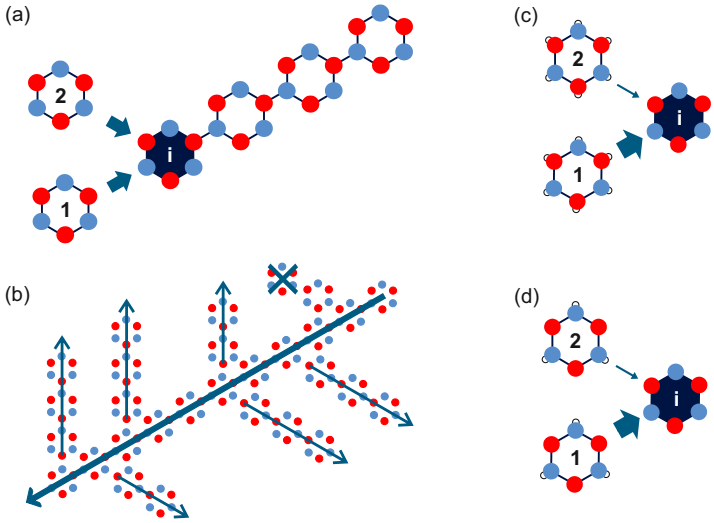

Figure 6.7: (a) An asymmetry in the adhesion energies for the formation of N-B bonds can explain the preferred growth directions. A borazine molecule can either attach with one of its nitrogen atoms to a boron atom of the existing hBN island, or vice versa, with an boron atom of the molecules to a nitrogen atom of the island. Since the two atomic species cannot be distinguished in the experiments, the atoms are colour coded in red and blue without an explicate assignment of the atomic species. The B_3N_3 ring labeled "i" represents the last ring of the existing island, the molecules "1" and "2" illustrate the two described scenarios. (b) Illustration of the growth directions of the side branches. (c) and (d) Illustration of possible reasons for unequal adhesion energies for the two adhesion scenarios: A hydrogenated (d) and partially dehydrogenated (e) borazine molecule attaches to a fully dehydrogenated hBN island.

in Fig. 6.7 (b), the main branch is again growing to the lower left. While the first molecule attaching sidewards forms two bonds to the original hBN chain, one blue-red and one red-blue, already for the second molecule of the side branch the situation is identical to the growth along the main branch, a red atom of the molecule bonds to a blue one of the island. Consequently, the side branches preferably grow "backwards" under an angle of 120°, in agreement with the experimental finding. Secondly, it explains the observation of the second type of aligned islands, rotated by 60° and with an inverted triangular shape (see Fig. 6.4 and discussion above). As long as the interaction of both atomic species with the substrate does not differ too much, islands with inverted structure (i.e., with boron and nitrogen interchanged) should also be stable and show the same growth behavior. Interchanging B and N also swaps the preferred and suppressed growth directions for both main and side branches, and hence explains why the second aligned domains look like mirror domains of the first.

The remaining question is the one for the origin of the asymmetry in the adhesion energies for the formation of N_{mol}-B_{isl} and B_{mol}-N_{isl} bonds. (The indices "mol" and "isl" indicate whether the atom is part of the attaching molecule or the existing island, respectively.) Possibly, dedicated density functional theory (DFT) calculations could give an answer to this. However, due to the incommensurate registry between the hBN islands and the substrate, such calculations are difficult and cannot be precise since they have to be performed with periodic boundary conditions which necessitates the approximation of a commensurate structure.

Without proper DFT calculations, one can only argue qualitatively acting from the known bonding energies for the free borazine molecule that have been calculated by Auwärter et al. [9]. Not surprisingly, these authors found the strongest bond between B and N, 6.29 eV, but also a difference of more than 0.5 eV in the bonding energies of the hydrogen atoms: For B-H and N-H, the values are 4.72 eV and 5.38 eV, respectively. It is well known that (reactive) surfaces reduce dehydrogenation energies strongly, but if this effect is different for atoms being already incorporated in the hBN islands compared to those of the attaching molecule, a scenario becomes possible that induces the asymmetry in the adhesion energies as concluded from the experiments. Two possibilities are sketched in Fig. 6.7 (c) and (d): If it is assumed that the hBN islands are completely dehydrogenated while the attaching molecule is not – this scenario is illustrated in panel (c) – one has to remove one H atom from the borazine molecule, either from a nitrogen atom or from a boron atom, in order to attach the molecule to the island. If it is further assumed that the significant difference between the B-H and N-H bonding energies found for the gas phase is at least partly preserved for molecules adsorbed on the Cu(111) surface, the formation of a bond between the molecule-boron and the hBN-nitrogen atom (B_{mol}-N_{isl}) would be favoured over the alternative scenario, a N_{mol}-B_{isl} bond. The same result is possible if the attaching borazine molecule is partially dehydrogenated, see Fig. 6.7 (d): In this case, the B_{mol}-N_{isl} could attach without any further dehydrogenation process whereas for N_{mol}-B_{isl} bonding the N-H bond still has to be broken. Other scenarios with similar results are possible, e.g., with partly dehydrogenated hBN islands. However, the decisive feature of all scenarios that can explain the observations is a difference in the dehydrogenation state of hBN islands and the borazine molecule when it attaches the island.

Although these qualitative considerations are somewhat speculative, they demon-

strate that there are simple (energetic) mechanisms that favour the asymmetry in adhesion energies as it was deduced from the experimental data. The suggested growth model is therefore realistic.

Finally, the growth of hBN/Cu(111) is discussed in context with studies of hBN on other substrates. Most of them were performed on more reactive surfaces like, e.g., Ni(111), Ru(0001), Rh(111), and Ir(111). On these substrates, compact, triangular islands have been reported [8, 9, 33, 99, 118], and the observation of atomic boron [83, 117, 121] or boron islands at low temperatures [118] indicates that borazine does not only dehydrogenate but that the B_3N_3 ring decomposes upon adsorption on these surfaces. Consequently, not (only) intact molecules, but also fragments attach to existing islands and form compact islands that are terminated by one species causing the triangular form. It is an ongoing discussion whether nitrogen [8, 9, 99] or boron [40] is the terminating species.
The proposed growth model for the case of hBN/Cu(111) does not require that the B_3N_3 ring decomposes. The model rather assumes that intact (at best dehydrogenated) molecules attach to the existing islands on the surface, and the triangular form is a consequence of three preferred growth directions. This is consistent with the fact that no indications for atomic boron was found for hBN on Cu(111) – neither in this study, nor by Brülke et al. [20, 21] who applied the same preparation scheme – or for hBN on Ag(111) [112] and Ag(001) [111]. Apparently, the surfaces of these noble metals are not reactive enough to crack the B_3N_3 ring, in contrast to the transition metal surfaces mentioned above. The different reactivities of these surfaces are also reflected by growth rates and dosages which have been used. While on the transition metal surfaces dosages below 100 L were sufficient for growing a monolayer of hBN, these numbers are higher by at least a factor of 20 for the noble metal surfaces (see section 6.2.4 for details).

6.1.6 Summary

The growth of hBN on Cu(111) at substrate temperatures above 1020 K was investigated *in-situ* and in real time using LEEM and LEED. Beside studying the movement of step edges across the surface and their interaction with impurities and nucleating hBN islands, the growth of hBN islands from nucleation to closing the first layer was discussed. The growth is self-limited to one single layer since the reactive Cu(111) surface is obviously essential for the formation of the hBN layer. As soon as the Cu surface is covered, the growth comes to a halt.

In contrast to what one might expect from earlier studies on many other substrates, no compact islands were found on this surface but the fractal growth of dendrite-like structures clearly exhibiting three different preferred growth branches within each island was observed. The orientation of the islands, in turn, is varying. By far the majority of islands belongs to two aligned domains that are oriented either 0° or 60° to the underlying substrate lattice. The remaining islands exhibit a random azimuthal orientation.

The fractal growth was explained by a model based on the experimental findings and some considerations of the adhesion energies. From LEEM and LEED experiments, the preferred growth directions could be correlated with the crystallographic [12] directions (and its symmetry equivalents) which corresponds to the direction of three of the six corners of the B_3N_3 hexagon (as illustrated in

Fig. 6.6). It is highly interesting that the growth takes place only in the direction of three of the six corners, those which are occupied by the same atomic species. This is explained by an asymmetry in the adhesion energy for the two relevant processes: Apparently, it is favourable to attach a borazine molecule with its atomic species "A" to an atom of species "B" of the existing hBN island. The alternative process, attaching the molecule with species "B" to an "A" atom of hBN, is suppressed. This asymmetry of adhesion energies can conclusively explain all experimental findings. Based on bond energies from the literature it can be speculated that "A" is boron, and "B" is nitrogen, i.e., that the molecules attach with a boron atom to a nitrogen atom of the island. However, it is not unambiguously possible to identify growth directions in relation to the occupancy of lattice sites by the atomic species, and therefore this point remains uncertain.

Furthermore, it is suggested that the asymmetry of adhesion energies is caused by different dehydrogenation states for the borazine molecule adsorbed on the surface and the hBN island. This, in turn, is probably due to an arbitrary but fortunate coincidence of the interaction strength between the borazine (and hBN) and the substrate. Compared to other metal substrates, hBN and borazine exhibit an intermediate interaction with Cu(111): It is (much) weaker than for transition metals but stronger than for Ag(001) and (111). Therefore, it is suggested that the fractal growth of hBN/Cu(111) is caused by different dehydrogenation states of borazine and hBN on Cu(111) which in turn is a consequence of the intermediate interaction strength between adsorbate and substrate.

6.2 Further details on the growth of hBN/Cu(111)

In this section, some further details are given regarding the growth of hBN on Cu(111) at high substrate temperatures. First, the influence of the focus conditions on the contrast, island size and LEEM intensity is discussed for hBN on Cu(111). Then, additional details of the LEED and LEEM investigations are presented. Thereafter, the rotation between real and reciprocal space are analysed and a brief overview of dosages for monolayer preparation of hBN on different metal substrates is given.

6.2.1 Influence of focus conditions on contrast, island size and LEEM intensity

Contrast and island size

What can be observed in LEEM images strongly depends on the imaging conditions that are applied when recording the images. For the system investigated in this work, step edges of the substrate surface are visible when the focus plane is located close to the bulk surface and behind (below) the adsorbate plane. Note that the focus is referred to the topmost objects of the sample, and therefore these imaging conditions are entitled as "underfocus", i.e., the focal length of the objective lens is "too long". Owing to the very small depth of the focus, the adsorbate is then out of focus and appears blurred. Consequently, the apparent size of the adsorbed objects (islands in this case) is bigger than the real size. When

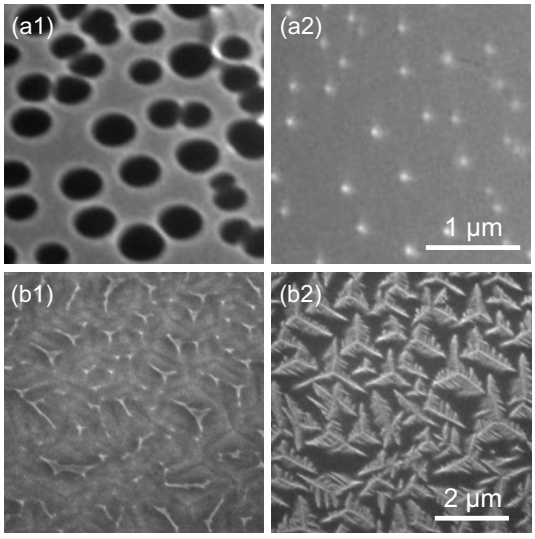

Figure 6.8: LEEM images recorded during the growth of hBN on Cu(111) (1085 K, 2.6×10^{-7} Torr) with different imaging conditions: Left: Underfocus, $U_{\text{start}} = 0.8\,\text{V}$; right: slight overfocus, $U_{\text{start}} = 2\,\text{V}$. The upper images are recorded at a very low coverage, the lower ones for approx. 0.4 ML.

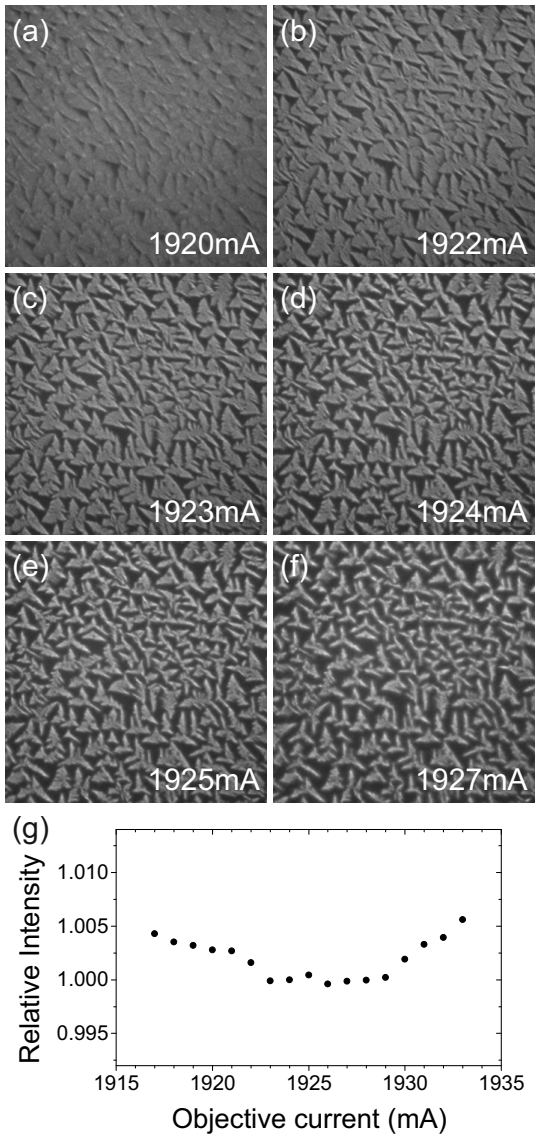

Figure 6.9: (a)-(f) LEEM images of hBN islands on Cu(111) taken after the deposition process (1067 K, 4.5×10^{-7} Torr) at different currents for the objective lens, from slight underfocus (a) to overfocus (f) (7 µm FOV, $U_{\text{start}} = 2$ V). (g) Relative integrated intensity of the LEEM images, plotted versus the objective current, from underfocus (lower current) to overfocus conditions (higher current).

moving further towards underfocus also the step edges appear blurry and become even better visible since they appear broader than in slight underfocus conditions. However, when the focal plane is shifted to the adsorbate plane or slightly above (slight overfocus), the islands are sharply imaged and their apparent size is realistic. Surface step edges cannot be seen any more in these conditions.

In Fig. 6.8, this is demonstrated with images taken for different focus plane positions and for two different coverages. The upper two images (a1) and (a2) are taken at very small coverages, the lower ones (b1) and (b2) at about 0.4 ML. In both cases, the left image (a1) and (b1) is taken in underfocus conditions, and it can clearly be seen that the adsorbate is unsharp and blurry. In panel (a1), it is also strongly enhanced in size. In (b1), the surface seems to be completely covered, although the real coverage is about 0.4 ML. The images recorded in slight overfocus (a2) and (b2), however, reflect the real size of the hBN islands better. Under these conditions, the dendritic shape of the islands is clearly visible, see panel (b2).

LEEM intensity

The fact that the observed island size strongly depends on the chosen imaging condition has to be considered when evaluating island sizes or coverages. However, although islands are not imaged on a real scale, the overall intensity of the LEEM image is almost independent of small changes of the focus. This is shown in Fig. 6.9 for different objective currents corresponding to focus conditions from slight underfocus to overfocus. Figure 2 (g) shows that the integrated LEEM intensity does not change by more than 0.5% in this range. This is very fortunate since it would be extremely difficult to keep the focusing conditions sufficiently constant during a growth experiment. This is mainly due to small drifts in the sample position rather than to instabilities of the current supplies. Note that a typical growth experiment takes up to three hours and the sample temperature must be kept constant at more than 1000 K during this time. For this reason, the integrated LEEM intensity rather than the observed island size is used for determining the growth rate in this work.

6.2.2 Details of the LEED and LEEM investigations of the hBN layer

LEED: Comparison with Brülke et al.

In order to verify that the samples of this thesis are identical to the ones used by Brülke et al. [21], several LEED measurements were performed with different start voltages. Figure 6.10 shows that all relevant details discussed in Ref. [21] are also visible in the LEED data of this thesis: The star-like broadening of the (0,0)-spot, identified as multiple scattering effect, is visible in the upper close-up (green frame). The lower close-up (blue frame) shows a Cu substrate spot and the diffraction ring of the hBN. It can be seen that the ring is located at slightly higher $k_{||}$ compared to the copper bulk spot.

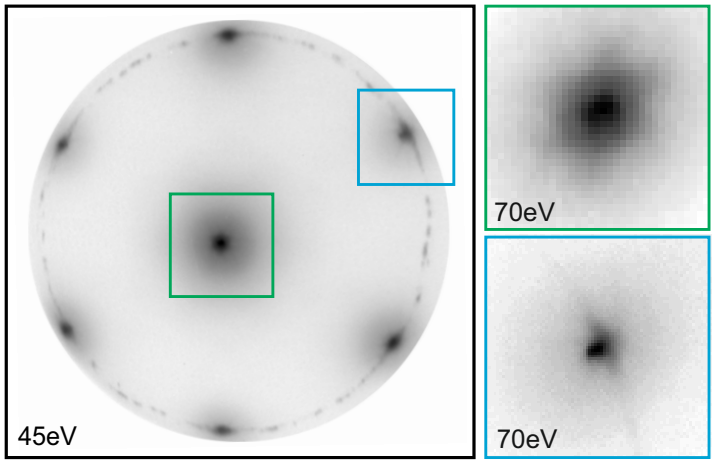

Figure 6.10: μLEED pattern of an almost closed layer of hBN on Cu(111) at $U_{\text{start}} = 45\,\text{V}$. The close-ups recorded at $U_{\text{start}} = 70\,\text{V}$ show the features around the (00) spot (green frame), which are due to multiple scattering, and the (10)-spot (blue frame) indicating that the hBN film and the Cu(111) substrate are incommensurate.

Non-equivalence of the (01) and (10) LEED spots

In section 6.1.3, the two domains of aligned hBN islands are distinguished from each other by using DF-LEEM measurements. This is possible due to the experimentally observed non-equivalence of the (01) and the (10) LEED spot. At first sight, this appears to be a violation of Friedel's rule, which states that the intensities of the (hkl) and the $(\overline{hkl})$ reflections are equal [52]. Since the (10) reflection is equivalent to the $(0\bar{1})$ reflection in three-fold symmetric structures, this rule seems to contradict the experimental observations for hBN/Cu(111). However, there are two reasons why Friedel's rule is not valid in our case.
When comparing (hk) and $(\overline{hk})$ reflections in LEED, one should consider that the diffraction rods for both reflections cut the Ewald's sphere at the same height, i.e. at the same $k_\perp$. Therefore, in LEED, one compares the intensities of (hkl) with $(\overline{hkl})$, not $(\overline{hkl})$. Thus, one expects the same intensity, e.g., if the diffraction rods are homogeneous as it is the case in 2D. In 3D structures, this is not necessarily the case. For the system under study, this means that a difference between the (01) and (10) reflection can be expected if hBN is not perfectly two-dimensional. But even if the system is assumed to be perfectly two dimensional, Friedel's rule is only valid for real atomic scattering factors f_j. If $f_j = |f_j| \cdot exp(i\varphi_j)$ with $\varphi_j \neq 0$, the absolute square $|F_h|^2$ of the structure factor:

$$F_h = \sum_j f_j exp(2\pi i \mathbf{h} \cdot \mathbf{r}_j) \tag{6.2}$$

will not be identical for $\mathbf{h}$ and $-\mathbf{h}$. Here, $\mathbf{h} = (hkl)$ is the reflection vector and $\mathbf{r}_j$ the position vector of atom j in the unit cell. While atomic scattering factors are often considered to be real in XRD, the scattering phases play a more important role in LEED so that in general one has to count on different values for φ_j for

different atomic species. It can be shown that such a phase difference leads to different structure factors, and therefore different intensities, for the (10) and the (01) reflection in the case of hBN on Cu(111).

LEEM on aligned domains

Brülke et al. [21] discussed a small broadening of the LEED maxima stemming from the aligned domains in azimuthal direction. Using a pseudo-Voigt fit, they found a full width at half maximum of 4.4° and interpreted this as a small rotational disorder of these majority domains. The LEED results of this work confirm this finding (see above) but LEEM can add even more detailed information.

Figure 6.12 depicts a series of seven DF-LEEM images corresponding to aperture positions along the diffraction ring very close to one of the main maxima. The path of the aperture (from (a) to (g)) is illustrated by the green arrow in panel (h). The LEEM images clearly show that the disorder is not caused by the islands of the aligned domains being (as a whole) slightly rotated with respect to each other but that the islands consist of many small sub-domains within the aligned hBN island which show a narrow distribution of azimuthal orientations. Hence, the disorder manifests itself on a smaller length scale than the island formation.

LEEM on rotated domains

Figure 6.11 shows that the aligned and rotated hBN domains cannot only be distinguished in DF-LEEM but also in BF-LEEM mode. There, they show a different contrast under certain imaging conditions. Panel (a) highlights the two differently oriented aligned domains in red and blue whereas the rotated domains are visible as gray (uncoloured) islands (see section 6.1.3 and Fig. 6.4 (b)). Panel (b) shows a BF-LEEM image of the same sample area recorded at a much higher

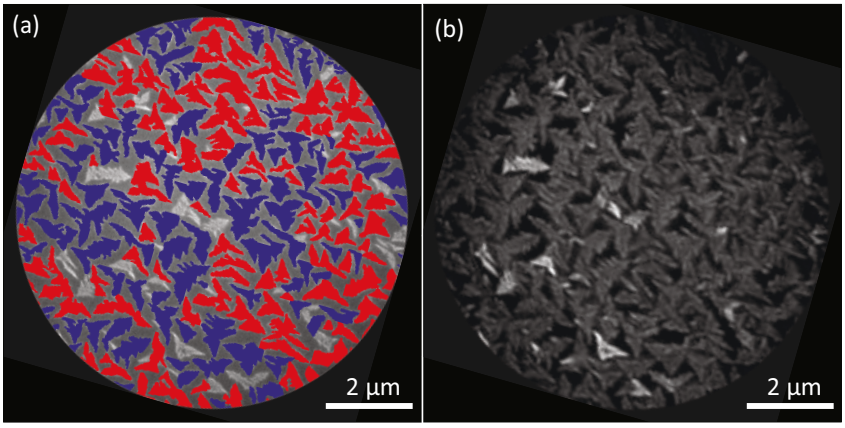

Figure 6.11: (a) False-colour illustration of the two aligned domains (in red and blue) in a BF-LEEM image ($U_{\text{start}} = 2\,\text{V}$). Rotated domains are shown in gray (uncoloured). (b) BF-LEEM image of the same sample area at $U_{\text{start}} = 45\,\text{V}$, indicating different (bright-field) contrast for the aligned and rotated domains.

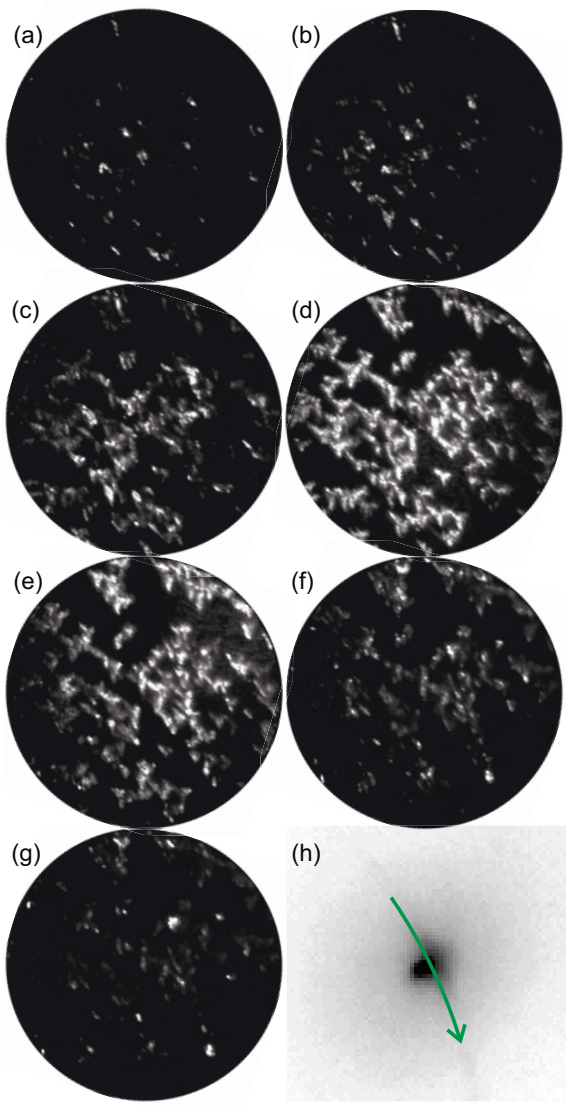

Figure 6.12: (a)-(g) DF-LEEM images recorded for an aperture position along the diffraction ring close to the (10) spot (10 µm FOV, $U_{\text{start}} = 45\,\text{V}$). (h) Close-up of the (10) LEED spot ($U_{\text{start}} = 70\,\text{V}$). The green arrow illustrates aperture positions used for (a)-(g).

start voltage of $U_{\text{start}} = 45$ V. It can clearly be seen that the rotated domains have a brighter contrast than the aligned ones under these imaging conditions. This difference in contrast is interpreted as an indication of differently strong interactions of the aligned and rotated hBN-domains with the substrate.

6.2.3 Rotation of real space vs. reciprocal space

It is a fundamental property of the electromagnetic lenses used in the LEEM instrument that any image projected through the lens is rotated. Since the rotation angle depends on the excitation current of the lens, it has to be considered when images obtained with different lens settings are compared. This is done in the sections 6.1 and 6.2 when relating LEED and LEEM images.

The angle of clockwise rotation θ_i is given as a function of the lens current I_i [51]:

$$\theta_i = \frac{K_i}{\sqrt{U^*}} I_i, \tag{6.3}$$

with $U^* = 1.0000009785\ U_{HV}$ and $U_{HV} = 20\,\text{kV}$. K_i is a constant depending on the type of the lens. The values for all relevant lenses of the microscope are listed in Table 6.1. Negative values of K_i result in a counter-clockwise rotation. Furthermore, the lens currents I_i used for LEED and for LEEM at a field of view of 10 µm are given. The uncertainty is ≈1 % [51].

With these values, the relative rotation between the LEED and the LEEM mode at a field of view (FOV) of 10 µm is 16.7°±2.8°. Note that all LEEM images shown in the sections 6.1 and 6.2 are measured with a FOV of 10 µm although sometimes smaller image sections are shown. This rotation angle was corrected in all LEEM and LEED images shown in the sections 6.1 and 6.2 so that real space and reciprocal space directions can be compared directly.

Table 6.1: Values for K_i and I_i for all relevant lenses used to determine the angle of image rotation θ_i for LEED and LEEM (at 10 µm FOV) in section 6.1 and 6.2.

lens i	$K_i(\frac{\sqrt{V}^\circ}{A})$ [51]	I_i (mA) for LEED	I_i (mA) for LEEM at 10 μm FOV
FL	5909.5	2769.0	1496.0
IL	7168.0	865.5	2062.1
P1	-7168.0	550.0	1134.0
P2	7168.0	1019.0	1126.0
P3	-7168.0	2650.0	2650.0

6.2.4 Dosages for monolayer preparation of hBN on different metal substrates

The reactivity of the substrate strongly influences the observed growth rates of hBN in the monolayer regime. This becomes obvious when the dosages needed to obtain an (almost) closed, 1 ML hBN layer are compared for different substrates. Table 6.2 lists these numbers for several transition metal as well as for noble metal surfaces. It can clearly be seen that for more inert surfaces much higher dosages are needed compared to the more reactive surfaces.

Table 6.2: Dosages needed to grow a closed layer of hBN on several substrate surfaces.

Substrate	Dosage
Ag(111)	135 000 L [112]
Ag(001)	3000 L [111]
Cu(111)	2000 L [121]
Ni(111)	60 - 100 L [7, 61, 121]
Ru(0001)	13 - 55 L [60, 99, 161]
Rh(111)	40 L [30]
Ir(111)	20 L [117]

6.3 Variation of substrate temperature

In this section, the influence of the substrate temperature during hBN preparation on the growth mode, the structure and the growth rate is investigated. For this purpose, the results of an additional growth series with three growth experiments, performed at different substrate temperatures (1061 K, 1015 K and 972 K) but with the same borazine partial pressure (2.5×10^{-7} Torr), are compared.
The sample prepared at 1061 K shows the same growth mode as already discussed in the previous sections. But at lower temperatures, the growth mode and the structural properties changes. Additionally, it is discussed that the growth rate decreases with decreasing substrate temperature.

6.3.1 Growth and structure

In Fig. 6.13, two LEEM image series are shown recorded during the growth of hBN on Cu(111) at substrate temperatures of 1061 K and 1015 K, respectively. At the higher substrate temperature ((a)-(c)), the growth mode is observed which was discussed in detail in section 6.1.4. The islands (bright contrast) show a fractal growth mode with three preferred growth directions per island having an angle of 120° between each other. This mode could be explained with a model based on the experimental observation that the growth preferably proceeds over the borazine ring corners, and the assumption that the attachment of borazine rings to an existing island includes an asymmetry concerning linkage via nitrogen

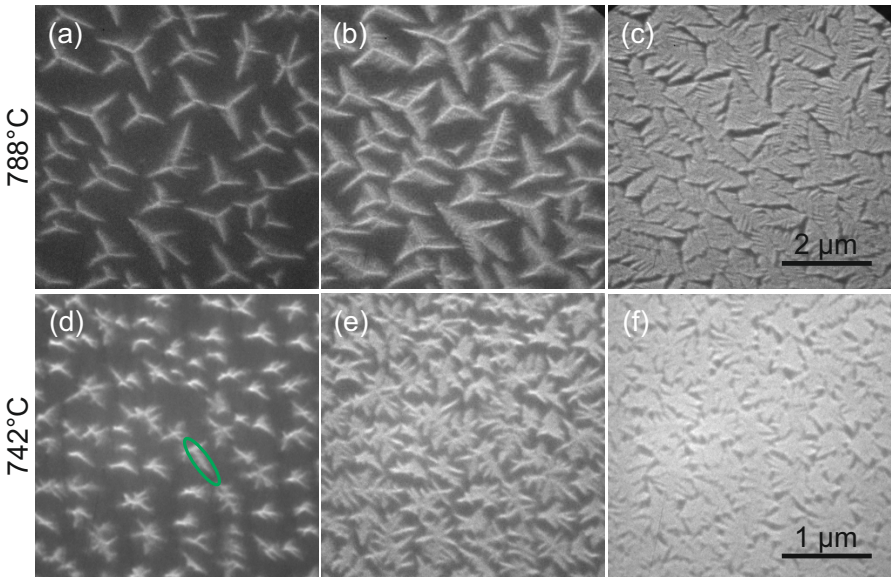

Figure 6.13: LEEM images recorded during the growth of hBN on Cu(111) at substrate temperatures of 1061 K ((a)-(c)) and 1015 K ((d)-(f)) ($U_{\text{start}} = 2$ V, slight overfocus). The hBN islands have a brighter contrast than the copper substrate. The substrate temperature has a strong influence on island shape and size. Please note the different scale bars.

or boron atoms (see section 6.1.5).
Different island shapes can be observed when 46 K or 89 K lower substrate temperatures are applied during growth. In Fig. 6.13 (d)-(f), this is shown for a substrate temperature of 1015 K. (Very similar observations were made for a substrate temperature of 972 K.) The islands still show a fractal growth mode. This is expected since the step edge diffusion decreases with decreasing substrate temperature which favours fractal growth [110]. The hBN also still forms branches preferably. However, the three distinct growth directions are not as clearly visible as for higher temperatures. Instead, various growth directions are found for the branches although some occur still remarkably often. As an example, one growth direction, which can be observed for several branches in various islands, is indicated with a green ellipse for one island in panel (d). Additionally, a clear differentiation in main and side branches is not possible any more and the islands are significantly smaller (note the different scale bars in Fig. 6.13).

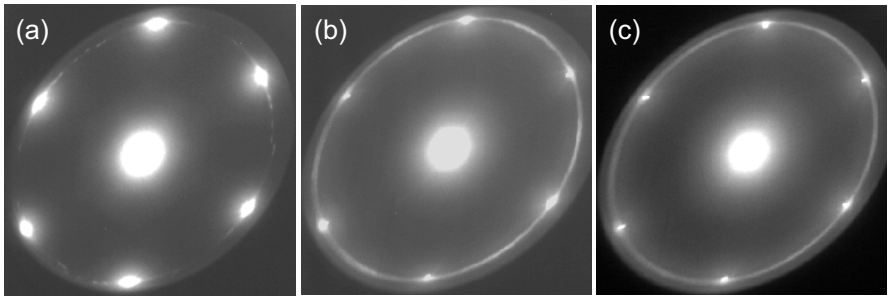

Figure 6.14: LEED images of three hBN/Cu(111) samples prepared at a substrate temperature of (a) 1061 K, (b) 1015 K and (c) 972 K.

LEED images of both preparations shown in Fig. 6.13 and of one performed at 972 K are depicted in Fig. 6.14. In all three LEED measurements, the modulated ring caused by the hBN overlayer is well visible. However, the intensities of the main maxima close to the Cu(111)-spots decrease with decreasing temperature and the intensity along the ring becomes more continuously distributed. The strong modulation observed in (a) was explained in section 6.1 with the small aperture size which allows only a small selection of domain orientations to contribute to the LEED measurement. In contrast, a nearly homogeneous intensity on the diffraction ring and therefore a nearly homogeneous distribution of domain orientations is found for the hBN structure grown at 1015 K (b) and 972 K (c) although the same aperture size was used. This indicates much smaller domains in these cases. Additionally, the intensity on these two rings slightly increases in-between the main maxima. This is more pronounced for the preparation at 1015 K than for the one at 972 K.
In the next step, DF-LEEM measurements of the samples prepared at 1061 K and 1015 K are compared to verify the assumption of smaller domain sizes for the preparations performed at lower substrate temperatures. The results for 972 K are very similar to the case of 1015 K. In Fig. 6.15 (c) and (e), DF-LEEM images using the (01)- and (10)-LEED spots are shown for the sample prepared at

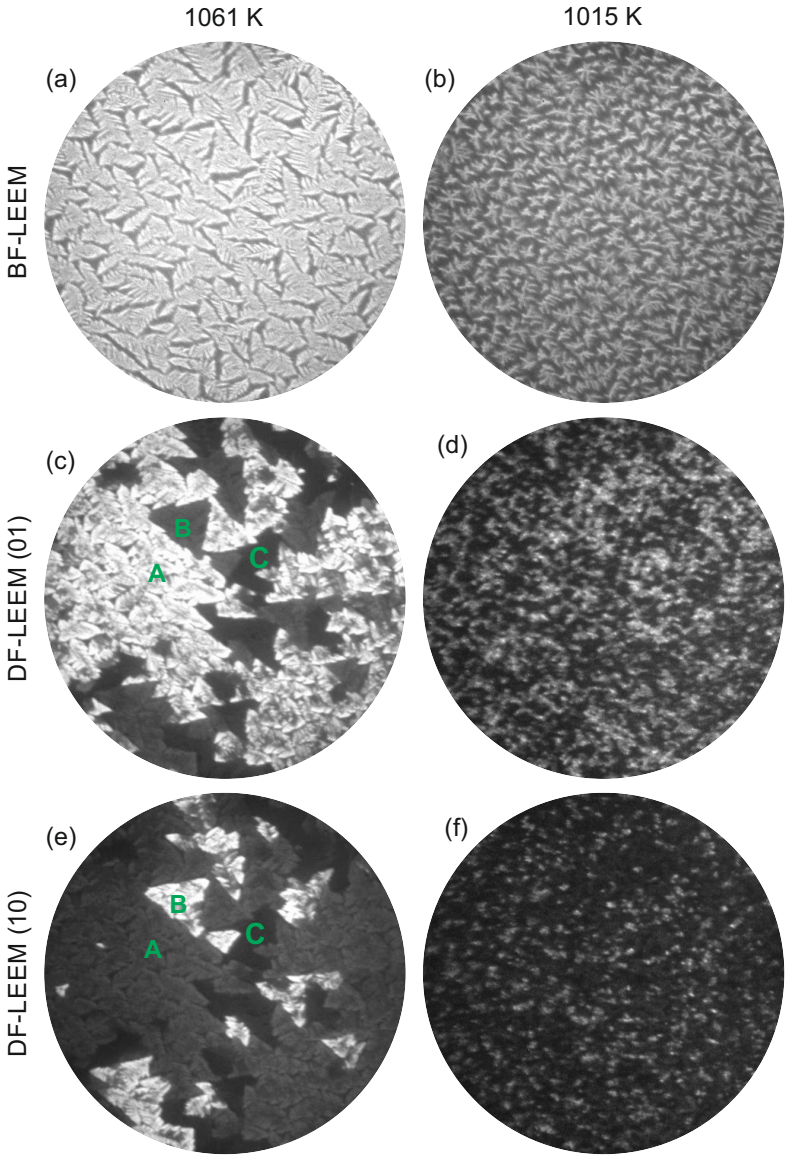

Figure 6.15: (a)+(b) BF-LEEM ($U_{\text{start}} = 2\,\text{V}$, slight overfocus) and (c)-(f) DF-LEEM images ($U_{\text{start}} = 45\,\text{V}$) using the (01)- and (10)-LEED spot, respectively, of two hBN/Cu(111) samples prepared at a substrate temperature of 1061 K (left) and 1015 K (right). All images have a FOV of 10 µm. In (c) and (e), three different levels of contrasts are indicated with A, B and C corresponding to the first and second aligned domain and the rotated domains of hBN on Cu(111), respectively. Please note that the DF-LEEM images ((d)+(f)) were performed on a closed monolayer hBN while the BF-LEEM image (b) was taken during hBN deposition at about 0.5 ML.

1061 K, respectively. In both images, three levels of contrasts can be seen which can be attributed to the first (A) and second aligned domain (B) and the rotated domain orientations (C) (see section 6.1.3 and 6.2.2 for more details). The corresponding images for the preparation done at 1015 K are depicted in (d) and (f). Here, it is more difficult to distinguish the three differently bright regions. However, it is obvious that the domain sizes are significantly smaller than for the preparation performed at higher deposition temperatures. They are even smaller than the hBN islands observed in BF-LEEM (b).

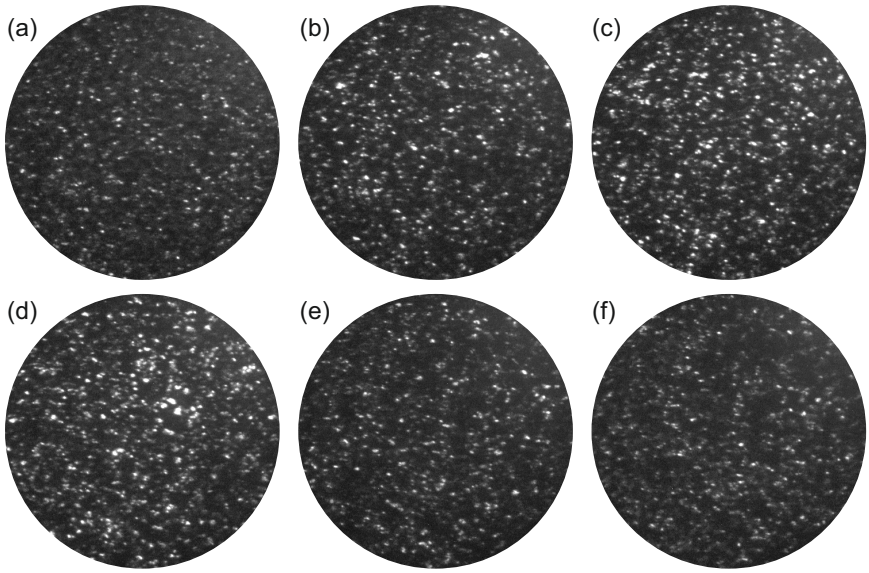

Figure 6.16: DF-LEEM images of hBN islands on Cu(111) grown at 1015 K for six different aperture positions along the diffraction ring between the main maxima (FOV 10 µm, $U_{\text{start}} = 45$ V).

In Fig. 6.16, DF-LEEM images recorded at six different aperture positions along the diffraction ring between the main maxima are depicted for the sample prepared at 1015 K. Again, the observed domains are smaller than the islands observed in BF-LEEM. Additionally at each aperture position along the diffraction ring (not only the shown six ones), many hBN structures with the corresponding domain orientation could be found. In contrast, only a low number of islands could be found at each aperture position for samples prepared at higher substrate temperatures (see Fig. 6.5).
In summary, a different growth mode than for higher substrate temperatures was found for growth temperatures of 972 K and 1015 K. The islands are still fractal but smaller and in particular do not show the three distinct growth directions as for the case of 1061 K. They rather grow towards various directions although there are still some (undefined) preferred directions. Additionally, DF-LEEM shows that the domains are significantly smaller than the ones at higher growth temperatures, and they are even smaller than the observed island sizes, i.e., the

islands contain more than one domain in many cases. This was not the case for higher growth temperatures. Because of the smaller domain size, a nearly homogeneous diffraction ring is observed in μLEED. Additionally, the μLEED measurements show that the total area of the aligned domains decreases with decreasing substrate temperature.
Therefore, we can conclude that at lower growth temperatures each island consist of several domains although it has grown as one island with several branches. However, the straight growth of individual branches indicates that probably each branch still belongs to just one domain.

6.3.2 Growth rate

The substrate temperature during growth has not only influence on the island shape and the structure but also on the growth rate. As discussed in section 6.1, the rate of the hBN growth is not constant although the substrate temperature and the borazine partial pressure are kept constant during one growth experiment. The reason for this is that the hot, uncovered Cu surface is needed for the reaction of borazine to hBN taking place, i.e. the surface acts as a kind of catalyst at these temperatures and gas pressures. The coverage vs. time curves for the three growth experiments performed with the same partial pressure for the borazine gas of 2.5×10^{-7} Torr but at three different substrate temperatures, are shown in Fig. 6.17 (a). They are obtained in a similar way as described in section 6.1.2. Additionally, the fits according to equation 6.1 are indicated (black dotted lines). They are in very good agreement with each of the three measurements showing that the assumption of a self-limiting growth is valid for all three substrate temperatures. However, the growth rate significantly decreases

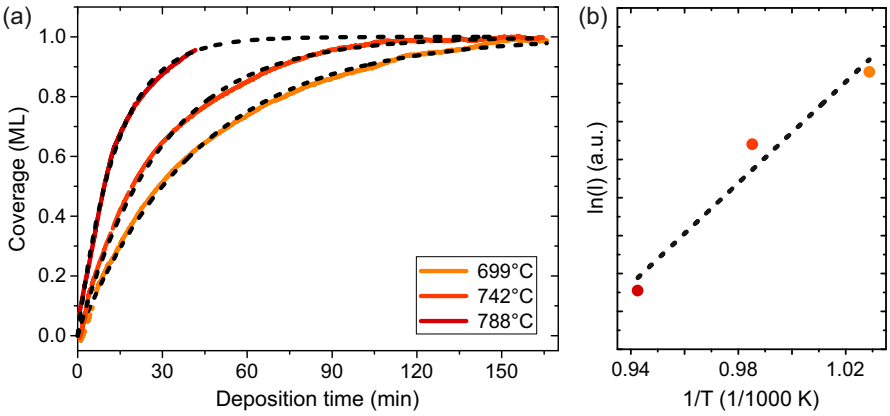

Figure 6.17: (a) Coverage of hBN/Cu(111) vs. the deposition time. The results of three growth experiments performed with different substrate temperatures but the same borazine partial pressure (2.5×10^{-7} Torr) are shown. For each measurement, the data was fitted according to equation 6.1. The growth rate increases with increasing substrate temperture. (b) Arrhenius-type plot of the fit parameter λ for the three experiments shown in (a).

with decreasing substrate temperature. For example, it took 9.5 min, 20.5 min and 30.0 min to reach a coverage of 0.5 ML for substrate temperatures of 1061 K, 1015 K and 972 K, respectively. It can be concluded that the reaction of borazine to hBN is faster for higher substrate temperatures leading to increased growth rates. From an Arrhenius-type plot (Fig. 6.17 (b)), the corresponding activation energy E_{barr} for this reaction can be obtained which is defined by:

$$\lambda = \lambda_0 exp\left(-\frac{E_{\mathrm{barr}}}{k_{\mathrm{B}}T}\right) \tag{6.4}$$

where λ is the fitting parameter in equation 6.1 for the three curves in panel (a) and λ_0 a constant. With only three experiments available, a reaction barrier E_{barr} = (1.2 ± 0.2) eV is found.
This can be compared with bond energies for the B-H and N-H bonds since we have shown above that these are the decisive bonds for growing hBN (compare 6.1.5). Auwärter et al. [9] calculated these bond energies for the gas-phase. For the B-H, N-H and B-N bond, they found bond energies of 4.72 eV, 5.38 eV and 6.29 eV, respectively. Thus, the measured reaction barrier E_{barr} of (1.2 ± 0.2) eV is significantly lower which can be attributed to the catalytic effect of the copper surface which reduces the energy barrier significantly and enables the growth of hBN structures at the temperatures applied here.

Chapter 7

Growth of PTCDA on hBN/Cu(111)

Due to its structural and electronic properties, in particular its insulating nature (direct band gap of 5.97 eV [184]), hBN is of highest interest as template for the formation of epitaxial layers of organic molecules. Recently, Brülke et al. [22] have shown with UPS and XSW measurements that a monolayer of hBN on Cu(111) is able to decouple the first PTCDA layer from the copper substrate chemically and electronically. The authors determined a large vertical bonding distance (3.38 Å) for PTCDA on hBN/Cu(111), only a very small out-of-plane distortion (<0.1 Å) and a HOMO position similar as for PTCDA multilayers.

In this chapter, the growth and lateral structure of PTCDA on hBN/Cu(111) is discussed. First, a short description of PTCDA on Cu(111) is given since this represents a reference system. Then, the growth of PTCDA on a (nearly) completed monolayer hBN and its lateral structure are discussed. Subsequently, the growth of PTCDA on a sub-monolayer hBN is studied.

7.1 Growth of PTCDA on Cu(111)

The system PTCDA on Cu(111) represents a reference system for the growth of PTCDA on hBN/Cu(111). It has already been investigated in several studies with several techniques. XSW was applied to investigate the vertical bonding distances [56]. For the carbon height, a value of 2.66 Å was found which is significantly smaller than the sum of the corresponding van der Waals radii (3.17 Å [18]) which is compatible with an overlap of the molecular orbitals and the metal bands. Additionally, the system was studied with UPS and was compared with PTCDA on Ag(111) and Au(111) [35]. Here, the largest charge transfer is observed for PTCDA on Cu(111) leading to a completely filled LUMO. Both, XSW and UPS data, indicate that the interaction between PTCDA and Cu(111) is rather strong.
The lateral structure of PTCDA on Cu(111) deposited at room temperature was investigated by Wagner et al. [181] with STM. The authors found two superstructures in the monolayer regime each with two molecules per unit cell in a herringbone structure. Nearly rectangular unit cells were proposed for both structures.

In SPA-LEED, Bauer [14] found also two phases, an incommensurate structure as majority phase (α-phase) and a p.o.l. or even commensurate structure as minority phase (β-phase). However, only the β-phase corresponds to one of the phases reported by Wagner et al. [181]. The α- and β-phase found by Bauer could be described by the following matrices A and B, respectively [14]:

$$A = \begin{pmatrix} 4.98(9) & 0.25(7) \\ 4.06(11) & 8.79(15) \end{pmatrix} \text{ and } B = \begin{pmatrix} 5.01(8) & 0.95(9) \\ 3.03(15) & 8.82(20) \end{pmatrix} \tag{7.1}$$

The corresponding LEED simulations are depicted in Fig. 7.1 (g) for the α- and β-phase in green and red, respectively. Furthermore, Bauer deposited PTCDA at 100 K and annealed the sample step-wise. After deposition, no sharp spots were visible but a diffuse intensity was observed where spots of the α- and β-phase are usually found. With increasing temperature, the spots became more distinct.

Overall, the findings reported above correspond very well to the LEED measurements performed in the LEEM instrument for PTCDA deposited at room temperature which are discussed briefly in the following.
During deposition of the first monolayer PTCDA on Cu(111), the LEEM intensity increases continuously ($U_{\text{start}} = 2\,\text{V}$) as it is visible in Fig. 7.1 (a). However, no island growth is observed in real space (b). Probably, the island sizes are below the resolution limit of 10 nm (The microscope was operated without aberration corrector) [58]. The strong interaction between the molecules and the copper substrate might lead to a high diffusion barrier and thus to small islands. According to Bauer [14], the domain sizes are about 31.5 nm for a PTCDA layer prepared at room temperature. He found clearly seperated LEED spots at these conditions. In our case, diffuse LEED spots are visible which could hardly be seperated as shown in Fig. 7.1 (d). This result is very similar to the mentioned SPA-LEED measurements of PTCDA deposited at 100 K [14].
After about 35 min of PTCDA deposition, the intensity increase saturates (Fig. 7.1 (a), $U_{\text{start}} = 2\,\text{V}$) and the nucleation of islands with a slightly darker contrast is observed in LEEM as depicted in Fig. 7.1 (c) ($U_{\text{start}} = 1.3\,\text{V}$). These newly nucleated islands represents the second layer since they disappear upon gentle annealing up to about 425 K after the end of the deposition. This value is even lower than the desorption temperature of the second layer PTCDA on Cu(111) reported by Wagner et al. [182] (573 K). Note that the second layer islands are larger than those in the first layer which can be explained by a higher mobility of PTCDA molecules adsorbed on another layer of PTCDA than on the clean Cu(111) surface. After desorption of the second layer (the first layer is still on the surface), the LEED image in Fig. 7.1 (f) was taken. Here, sharper spots are visible at the same positions as before. Additionally, the spot positions correspond very well to the α- and β-phase, as found by Bauer [14], which are indicated in Fig. 7.1 (g).
A LEEM-IV curve of the first monolayer PTCDA on Cu(111) is depicted in Fig. 7.1 (e). This curve will be applied in section 7.4 to identify PTCDA on Cu(111) next to hBN islands. The increase in intensity at about 0 V is caused by lensing effects induced by the close vicinity of islands of the second monolayer.

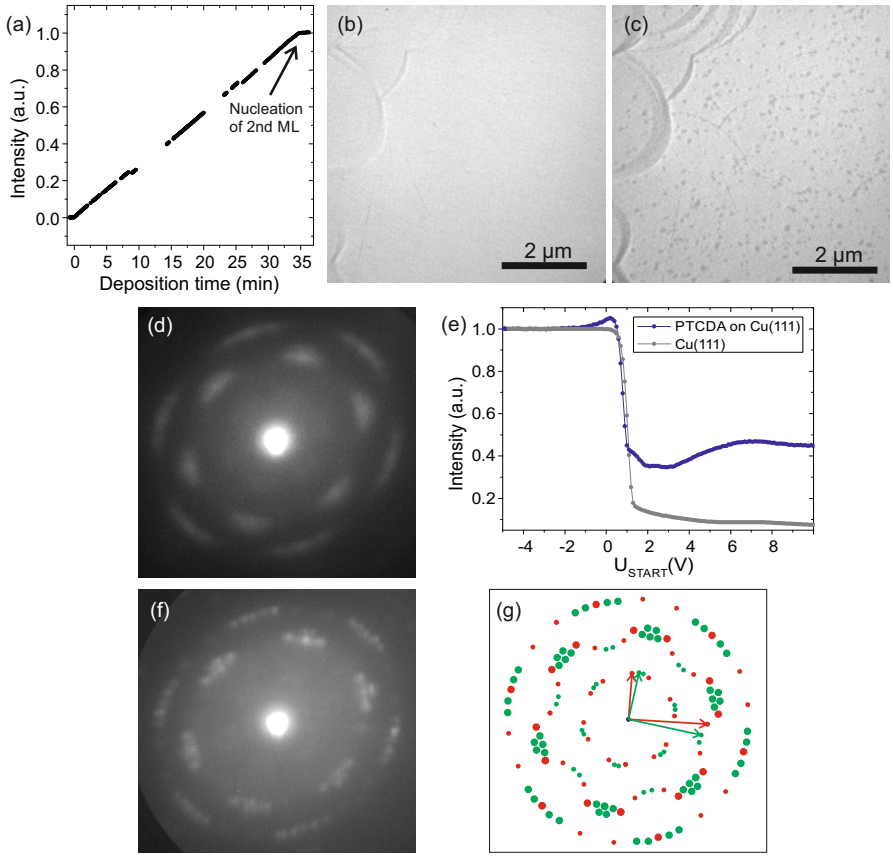

Figure 7.1: PTCDA on Cu(111): (a) LEEM intensity increase during the deposition of PTCDA on Cu(111) ($U_{\text{start}} = 2\,\text{V}$). (b) LEEM image after 25 min. No islands are visible. ($U_{\text{start}} = 2\,\text{V}$) (c) LEEM image after 35 min ($U_{\text{start}} = 1.3\,\text{V}$). The second layer starts to nucleate. (d) LEED measurement of the first layer of PTCDA on Cu(111) after 25 min of deposition ($U_{\text{start}} = 10\,\text{V}$). (e) LEEM-IV measurements of the first layer of PTCDA on Cu(111) and the clean Cu(111) crystal. (f) LEED measurement of one layer PTCDA on Cu(111) after desorption of the second layer by gentle annealing up to about 425 K ($U_{\text{start}} = 10\,\text{V}$). (g) Spot positions of the α- and β-phase, as found by Bauer [14], are indicated in green and red, respectively.

7.2 Growth of PTCDA on hBN/Cu(111)

In Fig. 7.2, a LEEM image series taken during the deposition of PTCDA (0.24 ML to 0.47 ML) on a (nearly) closed monolayer hBN/Cu(111) is depicted. The PTCDA molecules grow in compact islands which have a darker contrast than the hBN on Cu(111) at $U_{\text{start}} = 1.3\,\text{V}$. This is also visible in Fig. 7.3 where the LEEM-IV curves of one monolayer PTCDA on hBN/Cu(111) (red) and of a (nearly) closed monolayer hBN/Cu(111) (green) are compared with each other. Therefore, the intensity in the whole FOV decreases with increasing coverage as shown in Fig. 7.2 (e) (upper panel). This decrease is linear indicating a constant deposition rate. However, the growth of individual islands is not continuous, in contrast to, e.g., PTCDA on Ag(111) [66] or Cu(001) (see chapter 4). On these two substrates after nucleation, each PTCDA island grows linearly with deposition time as long as no step edges disturb the growth in certain directions. In the case of PTCDA on hBN/Cu(111), the growth of one island occurs stepwise. This is well visible in the corresponding LEEM video and in Fig. 7.2 (e) (lower panel) where the intensity of three smaller areas in the FOV are plotted versus the total coverage. These areas are marked in Fig. 7.2 (a) with the corresponding colour. They clearly show no linear but a stepwise decrease in intensity. During the short periods of rapid intensity decrease, the growth of PTCDA islands is observed in the LEEM video within the chosen sample area. In contrast, no change of these PTCDA islands is visible during the periods of stagnation. It should be mentioned that islands which have shown a step-wise growth very often belong to one domain of PTCDA on hBN/Cu(111). This growth mode can therefore not be explained by nucleation of several domains next to each other.

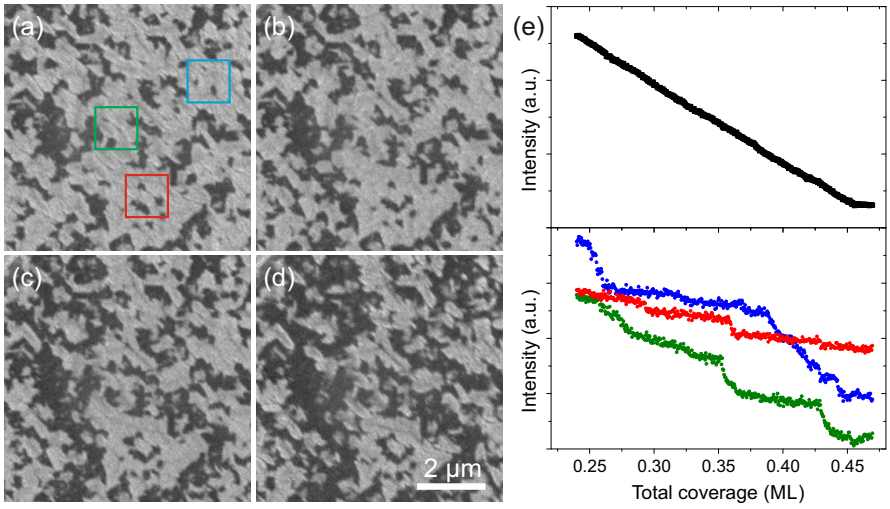

Figure 7.2: (a)-(d) LEEM image series taken during deposition of PTCDA on hBN/Cu(111). The PTCDA coverage raises from 0.24 ML (a) to 0.47 ML (d) (7 µm FOV, focus, $U_{\text{start}} = 1.3\,\text{V}$). (e) Intensity vs. coverage for the whole FOV (upper panel) and three selected areas (lower panel) marked in green, red and blue in panel (a).

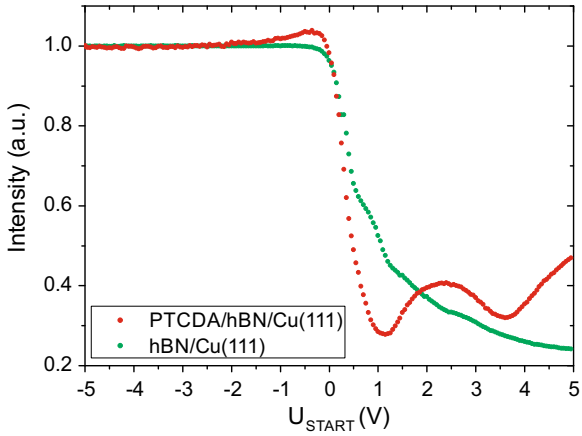

Figure 7.3: LEEM-IV curves of one layer PTCDA on hBN/Cu(111) (red) and of a (nearly) closed monolayer hBN on Cu(111) (green).

A possible explanation for this step-wise growth is that a critical molecular density close to an already existing island is necessary to allow the further growth of this island. A similar explanation was given for the nucleation of BDA c(8x8) crystallites on Cu(001) [141, 142]. Before these crystallites nucleate, the dilute phase of BDA has to reach a certain density which then remains constant while the crystallites are growing continuously.
A similar mechanism could be responsible for the growth behaviour which we observed here for PTCDA on hBN/Cu(111). The periods of growth could be explained by the PTCDA density exceeding a critical value and the periods of stagnation by it falling below this critical density. Apparently, the (fast) growth of the PTCDA islands itself causes the drop of the PTCDA density in the vicinity of the islands.

7.3 Structure of PTCDA on hBN/Cu(111)

A LEED measurement of 0.3 ML PTCDA on a (nearly) closed monolayer hBN on Cu(111) is depicted in Fig. 7.4 (a). The LEED spots are not sharp but rather diffuse and can be divided into outer and inner maxima because of their radial distances to the (0,0)-spot. The maxima are mainly broadened in azimuthal direction which leads to a ring-like appearance. Additionally, the inner maxima appear to be broader in radial direction than the outer ones.

A SPA-LEED measurement of a sample prepared under similar conditions was done by Christine Brülke et al. [20]. Their measurement was performed at 110 K. They also found clearly azimuthaly broadened, ring-like intensity maxima. But in contrast to our data, they could unambiguously identify the individual LEED spot positions within these maxima. Therefore, they determine the superstructure matrix for this structure to be

$$\begin{pmatrix} 5.22(5) & 0.9(1) \\ 3.1(3) & 8.81(9) \end{pmatrix}. \tag{7.2}$$

This corresponds to lattice parameters of $|\mathbf{a}| = 12.07(3)$ Å, $|\mathbf{b}| = 19.33(9)$ Å, $\gamma = 90(3)^\circ$ (angle between lattice vectors) and $\alpha = 9(1)^\circ$ (angle between $\mathbf{a}$ and $[\bar{1}\bar{1}2]_{Cu}$). For comparison, the simulated LEED pattern of this structure is superimposed on our measurement in Fig. 7.4 (b).

The simulated LEED spot positions and the positions of measured intensity maxima are in good agreement. Therefore, it can be assumed that our LEED measurement corresponds to the structure found by Brülke [20] and that the higher resolution of the SPA-LEED instrument compared to our LEEM instrument and

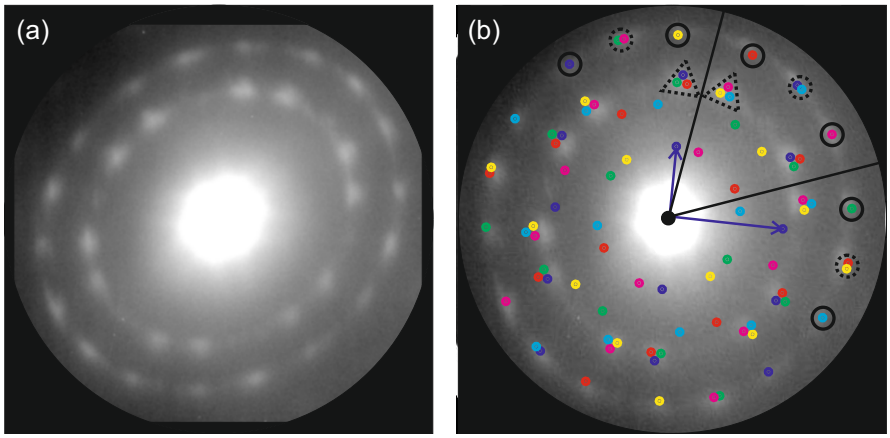

Figure 7.4: (a) LEED measurement of 0.3 ML PTCDA deposited on a (nearly) completed monolayer hBN on Cu(111) at room temperature ($U_{\text{start}} = 10$ V). (b) Simulated LEED pattern of the superstructure determined by Christine Brülke [20] superimposed on (a) after distortion correction. The spots of each domain are shown in a certain colour. The direction of the Cu(111) unit cell are indicated with black lines and the spots used for DF-LEEM are marked with black solid circles ("single-domain spots"), dashed circles ("double-domain spots") and triangles.

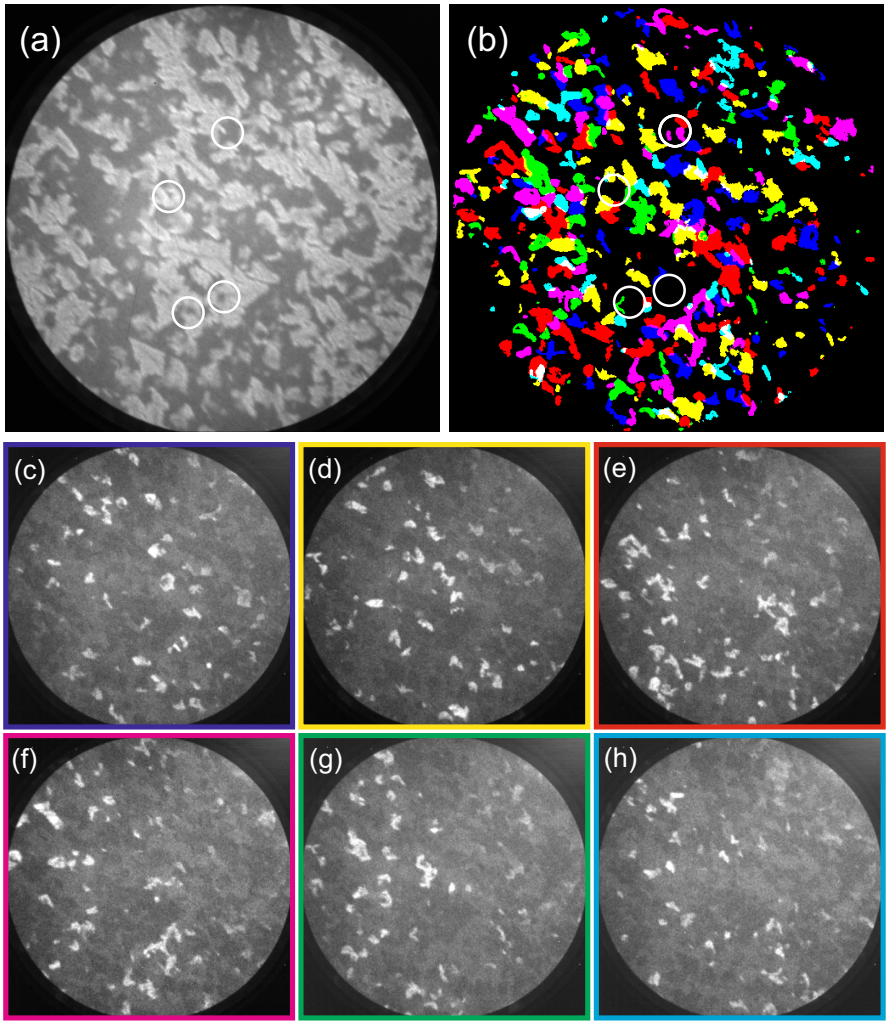

Figure 7.5: (a) BF-LEEM image of about 0.3 ML PTCDA (darker contrast) on a nearly closed monolayer hBN (brighter contrast) on Cu(111) ($U_{\text{start}} = 1.3\,\text{V}$, 5 µm FOV). (b) False colour image of six DF-LEEM measurements in (c)-(h) which corespond to the single domain spots marked in Fig. 7.4 (b) with solid circles ($U_{\text{start}} = 8\,\text{V}$, 5 µm FOV). Some islands are found in BF-LEEM but not in the six DF-LEEM images. Four of them are indicated with white circles in (a) and (b).

possibly a slightly worse ordering or smaller islands can explain the differences. The radially broader spots on the inner intensity ring are than in fact consisting of three diffuse diffraction spots (as marked with dotted triangles in Fig. 7.4 (b)).

In the next step, DF-LEEM measurements are performed using the aperture positions marked in Fig. 7.4 (b) with black circles and triangles. First, the six LEED intensities indicated with black, solid circles are used which correspond to "single-domain spots" according to the overlayer structure determined by Brülke [20]. Therefore, the resulting DF-LEEM images shown in Fig. 7.5 (c)-(h) are marked with the corresponding colour. In the false colour image in Fig. 7.5 (b), these six measurements are superimposed. It shows that the bright areas of the six DF-LEEM images do not overlap and that nearly the whole area covered with PTCDA (darker contrast in Fig. 7.5 (a)) is found in the six DF-LEEM images indicating that PTCDA grows preferably in these six domain orientations. Only, very few islands are found in BF-LEEM but not in the six DF-LEEM images. Four of them are indicated with white circles in Fig. 7.5 (a) and (b). Possibly, they correspond to differently orientated islands and would be found in DF-LEEM for other aperture positions along the outer diffraction ring.

The DF-LEEM images using the three aperture positions indicated with black, dashed circles in Fig. 7.4 (b) are depicted in Fig. 7.6 (a)-(c). According to the overlayer structure proposed by Brülke [20] and as indicated in Fig. 7.4 (b), LEED spots from two domains are located very close to each other at these positions. Therefore, they are called "double-domain spots". In each panel of (d)-(f), the DF-LEEM images of the two corresponding domains (as obtained from measurements on single-domain spots) are shown in their respective colour. The agreement between DF-LEEM measurements and the false-colour images (e.g. (a) and (b)) is quite good.

For the DF-LEEM images in Fig. 7.7 (a) and (b), the two LEED intensities marked with triangles in Fig. 7.4 (b) are used which should correspond to three domains each. The corresponding three domains are shown in panel (c) and (d). Again, a quite good agreement is observed. The slight differences could be explained by the small size of the aperture.

All these results are consistent with the overlayer structure found by Brülke [20] for PTCDA on hBN/Cu(111) under the assumption that 6 domain orientations are strongly preferred on hBN/Cu(111) and that only very small areas show other azimuthal orientations. However, the fact that such azimuthal disorder occurs is a strong indication for a rather weak interaction between PTCDA and the substrate. Another indication for the weak interaction is that the structure for PTCDA on Cu(111) is very similar to the one of PTCDA on the Au(111) surface, which is known for its weak interacting nature [35, 68]. There, a rectangular unit cell was found which has lattice parameters of $|\mathbf{a}| = 12.3(2)$ Å, $|\mathbf{b}| = 19.6(3)$ Å, $\gamma = 89.7(7)^\circ$ (angle between lattice vectors) and $\alpha = 22.0(6)^\circ$ (angle between $\mathbf{a}$ and $[\bar{1}\bar{1}2]_{Au}$) [104]. Therefore, our data is in good agreement with recent XSW and UPS results [22] which show that the hBN layer decouples the PTCDA layer from the copper substrate chemically and electronically.

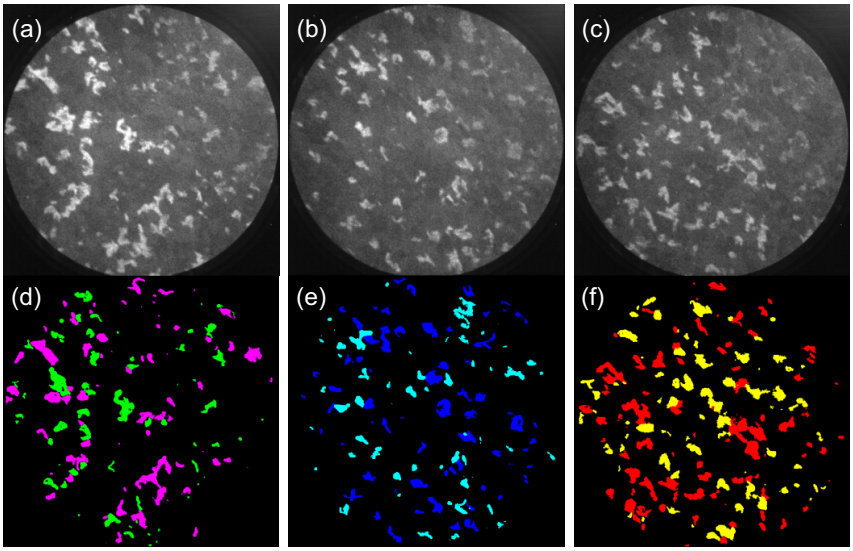

Figure 7.6: (a)-(c) DF-LEEM measurments performed with aperture positions indicated with black, dashed circles in Fig. 7.4 (b) ("double-domain spots"). (U_{start} = 8 V, 5 µm FOV) (d)-(f) False colour images of the two domains contributing to the measurements in (a)-(c) as obtained from two DF-LEEM measurements on single-domain spots.

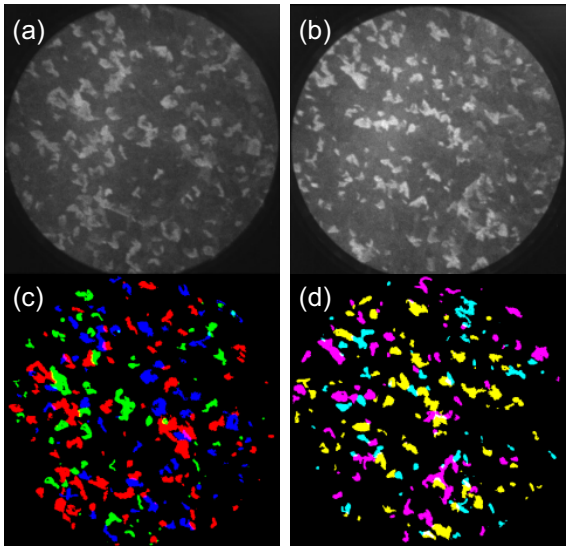

Figure 7.7: (a) and (b) DF-LEEM measurments performed with aperture positions indicated in Fig. 7.4 (b) with black triangles. (U_{start} = 8 V, 5 µm FOV). (c) and (d) False colour images of the three domains contributing to the measurements in (a) and (b) as obtained from three DF-LEEM measurements on single-domain spots.

7.4 Growth of PTCDA on sub-ML hBN/Cu(111)

In this section, the growth of PTCDA on a sub-monolayer hBN/Cu(111) is investigated. Here, the main question is if PTCDA grows preferably on hBN or on Cu(111). For this purpose, a sample with a very low coverage of hBN on Cu(111) is chosen as depicted in Fig. 7.8 (a). Here, the areas between the hBN islands are large enough to be analysed separately from the areas covered with hBN.
With the start of PTCDA deposition, an increase in intensity is observed on the Cu(111) surface, i.e., on the areas between hBN islands (Fig. 7.8 (c), $U_{\mathrm{start}} = 2\,\mathrm{V}$). But on the hBN islands, no PTCDA islands have nucleated within the first 32 min as can be seen in Fig. 7.8 (b) when it is compared to (a). These indications for the growth of PTCDA on Cu(111) are supported by LEEM-IV and LEED.
In Fig. 7.8 (d), a LEEM-IV measurement taken after 32 min of PTCDA deposition next to an hBN island (cyan) is compared with one of a monolayer PTCDA

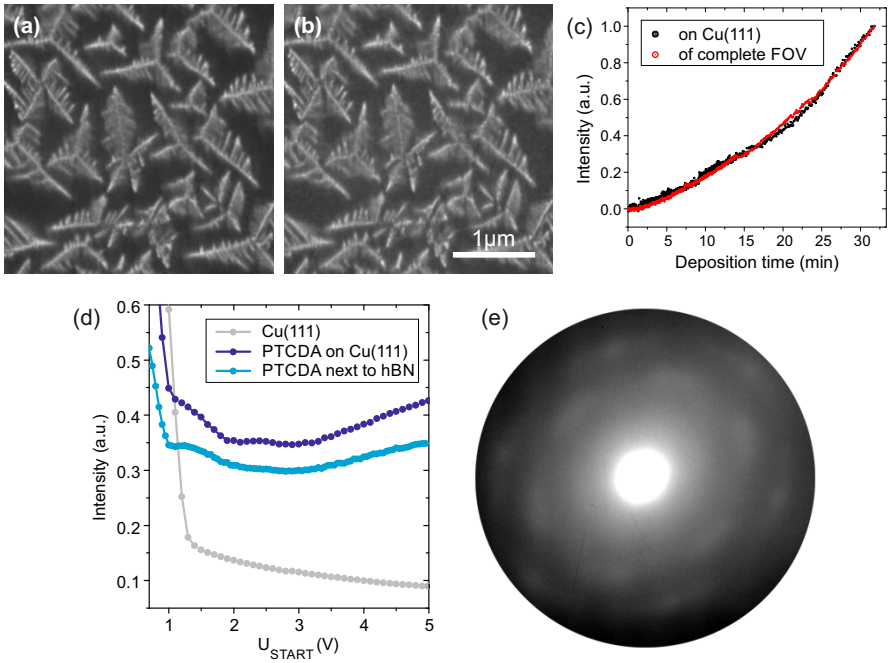

Figure 7.8: (a) hBN islands (bright contrast) on Cu(111) before the deposition of PTCDA. (b) Same sample area after deposition of PTCDA for 32 min and shortly before the growth of PTCDA islands on the hBN starts. (c) BF-LEEM intensity on the areas next to the hBN islands and of the whole FOV plotted vs. the deposition time ($U_{\mathrm{start}} = 1.3\,\mathrm{V}$). (d) LEEM-IV curves for the Cu(111) surface next to an hBN island of the sample shown in (b) (cyan). For comparison, the curves for PTCDA/Cu(111) (without hBN, see Fig. 7.1 (e)) and the clean Cu(111) surface are shown in blue and grey, respectively. (e) LEED image of the sample in (b) ($U_{\mathrm{start}} = 10\,\mathrm{V}$).

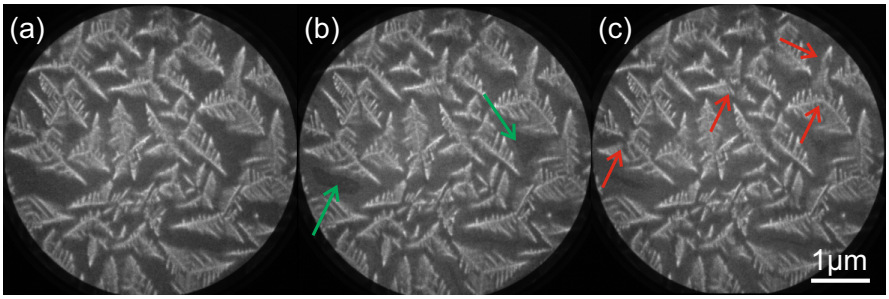

Figure 7.9: LEEM image series taken during deposition of PTCDA on sub-monolayer hBN on Cu(111) after (a) 37 min, (b) 40 min and (c) 42 min (U_{start} = 1.3 V). The green arrows mark phase boundaries (see text for more details) while the red ones are indicating the first PTCDA islands on hBN.

on Cu(111) (without hBN, see Fig. 7.1 (e), blue curve) and of a clean Cu(111) surface (grey). The cyan and grey curves differ strongly from each other indicating that the copper surface is definitely not clean any more. The shape of the cyan and blue curve are also not exactly identical, in particular at low start voltages (below 1 V). However, this can be explained by strong lensing effects caused for the cyan curve by the close vicinity to hBN islands. At higher start voltages, the curves have very similar features. For example, they exhibit a local maximum at about 1.2 V and show an increase in intensity between 3 V and 5 V. Here, higher start voltages were not chosen to circumvent beam damage.
A LEED measurement at the same coverage is depicted in Fig. 7.8 (e). The observed pattern is in very good agreement with the one of a monolayer PTCDA on Cu(111) deposited at room temperature without any hBN on the surface (Fig. 7.1 (d)) which was discussed in section 7.1. Therefore, we can conclude that the PTCDA molecules start to cover the Cu(111) surface before the first PTCDA islands nucleate on the hBN islands.

After about 42 min, the first islands nucleate on the hBN islands as indicated in Fig. 7.9 (c) with red arrows. At $U_{\text{start}} = 1.3$ V, they exhibit a darker contrast than hBN/Cu(111) but appear similar to PTCDA/Cu(111). Shortly before the first nucleation of PTCDA on hBN takes place, a discrete increase in contrast next to the hBN islands is observed. This change propagates from the hBN islands towards the centres of the former uncovered Cu(111) areas. This moving front is indicated in Fig. 7.9 (b) with green arrows. This change could be an indication for a phase change to a slightly different and possibly denser structure of PTCDA on Cu(111) since it is triggered by the increasing amount of PTCDA on the surface. No significant change in LEED could be observed. However, this indicates that the Cu(111) surface is nearly closed before the first PTCDA islands nucleate on the hBN islands. This is supported by the constant LEEM intensity next to the hBN islands for higher PTCDA coverages as shown in Fig. 7.10 (g). Here, the intensities of the complete FOV and of the area next to the hBN islands are plotted vs. the deposition time. The normalization is chosen as in Fig. 7.8 (c). At the point of PTCDA island nucleation on hBN, the intensity of the whole FOV is decreasing while the one next to the hBN islands is nearly constant. Six of the

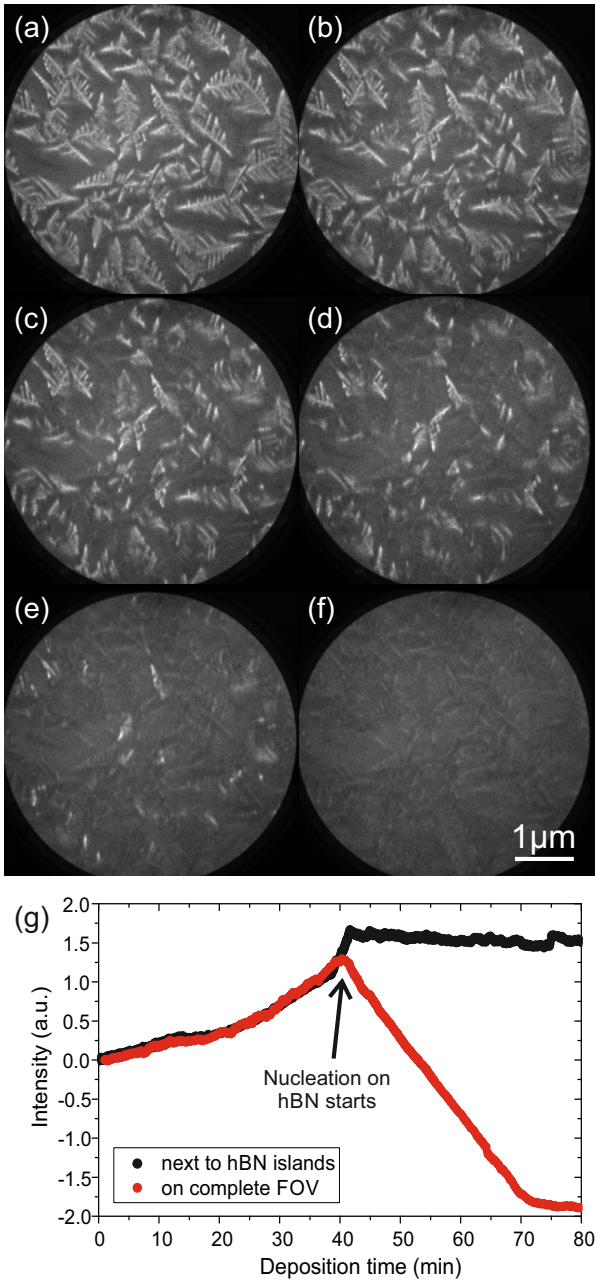

Figure 7.10: LEEM images series recorded during deposition of PTCDA on sub-monolayer hBN on Cu(111) after (a) 42 min, (b) 48 min, (c) 55 min, (d) 61 min, (e) 68 min and (f) 72 min ($U_{\text{start}} = 1.3\,\text{V}$). (g) Intensity next to the hBN islands and of the whole FOV plotted vs. the deposition time. The normalization is chosen as in Fig. 7.8.

corresponding LEEM images are depicted in Fig. 7.10 (a)-(f).
Again, the step-wise growth can be observed in the corresponding LEEM video as already discussed in section 7.2. A preferred nucleation site for the PTCDA islands could not be determined. They start to grow at main branches, side branches and close to the point of hBN nucleation.

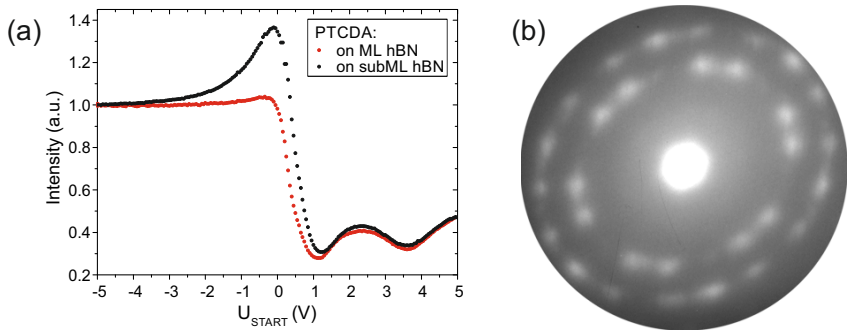

Figure 7.11: (a) LEEM-IV and (b) LEED measurement ($U_{\text{start}} = 10\,\text{V}$) of PTCDA on a sub-monolayer hBN on Cu(111) after 72 min of PTCDA deposition. For comparison, the LEEM-IV curve for PTCDA on a monolayer hBN/Cu(111) as depicted in Fig. 7.3 is shown in (a).

The deposition was stopped after 72 min when the complete surface is covered with PTCDA. The LEEM-IV measurements and the LEED image of this sample (Fig. 7.11) are in good agreement with the ones in Fig. 7.3 and 7.4, respectively.

7.5 Summary

We have unambiguously found that PTCDA molecules deposited on hBN/Cu(111) samples cover the remaining clean copper surface first, before they nucleate on hBN/Cu(111). Then, the individual PTCDA islands do not grow linearly in size although the deposition rate is constant. They show a step-wise growth mode. Usually, the periods of growth are significantly shorter than the periods of stagnation. A possible explanation for this step-wise growth is that a critical molecular density close to the islands is necessary to let the islands grow. If this density is not constant during growth and drops below the critical value, the growth of the islands gets to a halt until the critical density is reached for the next time. Furthermore, it has been discussed that all LEED and DF-LEEM results are consistent with the overlayer structure found by Brülke [20] for PTCDA on hBN/Cu(111). We both observed that 6 domain orientations are strongly preferred on hBN/Cu(111) but that other azimuthal orientations also occur. This azimuthal disorder and the fact that this overlayer structure is very similar to the one of PTCDA on the weakly interacting Au(111) surface [35, 68, 104] are strong indications for a weak interaction between PTCDA and the hBN layer.

Chapter 8

Summary

In this thesis, the growth of two organic molecules, PTCDA and NTCDA, and of the 2D material hBN on copper surfaces are investigated. The particular focus of this work lies on the interplay of different interaction mechanisms occurring for these systems which lead to completely different growth modes including dendrite-like, fractal growth modes and compact island formation.

Organic Molecules
In the first part of this thesis, the growth of PTCDA and NTCDA on the Cu(001) surface are investigated. Although these two molecules are chemically closely related, they exhibit two different growth modes on this metal surface.
For PTCDA on Cu(001), it is well known that the attractive intermolecular interaction of the PTCDA molecules, caused by the quadrupole moment of the molecule, leads to the growth of compact islands at already very low coverage [54, 66]. This process is quantified in this work by determining three important growth parameters which influence the island formation: the critical cluster size, the cohesion energy of two PTCDA molecules and the diffusion barrier of the adsorbed molecules. By analyzing island size distributions within the aggregation regime and applying methods developed for atomic nucleation on surfaces, it was possible to determine the critical cluster size i for temperatures between 300 K and 390 K. This parameter corresponds to the number of molecules in the largest cluster of molecules which is not yet stable. The fact that for temperatures below 317 K two molecules are already forming a stable cluster ($i = 1$) enabled to calculate the diffusion barrier for individual molecules on this surface: $E_{\mathrm{D}} = (0.45 \pm 0.21)\,\mathrm{eV}$. With increasing temperature, one expects an increase of the critical cluster size. However, the case of $i = 2$ is experimentally not observed; instead at temperatures above 317 K, four molecules are needed to form a stable cluster ($i = 3$). This direct change in critical cluster size from 1 to 3 is explained by the specific geometric conditions for the case of PTCDA/Cu(001). Furthermore, using pair-potential calculations it is possible to determine a second crucial energy for layer growth: the cohesion energy of two molecules which amounts to $E_{\mathrm{B}}^{(2)} = (0.89 \pm 0.34)\,\mathrm{eV}$.
In contrast to PTCDA, NTCDA exhibits a completely different growth mode on the same substrate in the submonolayer regime for temperatures at and above room temperature. Clear indications are found for a dendrite-like, fractal growth mode. This finding is based on BF-LEEM measurements indicating that no com-

pact islands occur although the LEED pattern is well established already at low coverage, on DF-LEEM results showing a static domain shape and size during growth within almost the entire submonolayer regime ($\approx 0.2 - 1.0$ ML), and on RT STM images showing groups of elongated islands at low coverage, which seem to interact with each other since they are identically oriented within clusters of islands on the 100 nm scale. With the aid of valence band PES and NIXSW results revealing a relatively strong (chemisorptive) adsorbate-substrate interaction, the observed growth mode is explained using pair-potential calculations. These calculations reveal that – under the specific conditions of net charge transfer into, and charge redistributions inside the molecule – one specific adsorption site is strongly favored, which is responsible for the growth of long and thin molecular chains. These chains form a dendrite-like network spreading over the entire surface already at very low total coverage. Thereby, they "reserve" certain surface areas for its respective domain, which subsequently are just filled up by the molecules adsorbing additionally. Furthermore, the pair-potential calculations show that small differences in the geometric structure and the charge redistribution inside the molecules can cause a fundamentally different growth behavior, as it was observed for NTCDA on other substrates, e.g. on Ag(111) [62].
Additionally, this dendrite-like growth mode leads to very large domains (with diameters > 5 μm) for NTCDA on Cu(001) so that this system is used as prototype system for a proof of principle experiment: Momentum microscopy of a single molecular domain performed with the LEEM/PEEM instrument. Such a single-domain ARPES experiment improves the results of orbital tomography by reducing the number of molecule orientations contributing to the measurement and allows separate measurements of different structural phases coexisting on a sample.
Finally, a second phase of NTCDA on Cu(001) is discussed which occurs at higher substrate temperatures and coexists with the dendrite-like phase. In contrast to the dendrite-like phase, the growth of the second one can be observed with BF-LEEM and is restricted to the direct neighborhood of step edges.

2D materials

The growth of hBN on Cu(111) is investigated in detail in the second part of this thesis. For substrate temperatures above 1020 K, the growth of fractal hBN islands is directly observed in LEEM. Each of these islands clearly exhibits three preferred growth branches leading to a three-fold symmetric shape. However, the orientation of the islands is varying. By far the majority of islands belongs to two aligned domains that are oriented either 0° or 60° to the underlying substrate lattice while the remaining islands exhibit a random azimuthal orientation indicating the rather weak but not negligible influence of the substrate on the hBN island growth.
While the fractal growth mode can be understood in terms of diffusion-limited aggregation (DLA), the preferred growth directions are explained by an asymmetry of the bonding energies for the two possible ways a borazine molecule can attach to an existing hBN island. This growth model is based on the experimental findings and some considerations of the adhesion energies: From LEEM and LEED experiments, the preferred growth directions could be correlated with the direction of three of the six corners of the B_3N_3 hexagon. It is highly interesting

that the growth takes place only in the direction of three of the six corners, those which are occupied by the same atomic species. Apparently, it is favorable to attach a borazine molecule with its atomic species "A" to an atom of species "B" of the existing hBN island while the alternative process, attaching the molecule with species "B" to an "A" atom of hBN, is suppressed. This asymmetry can conclusively explain all experimental findings.
A possible reason for this asymmetry of adhesion energies are different dehydrogenation states for the borazine molecule adsorbed on the surface and the hBN island, which in turn might be a consequence of the intermediate interaction strength between adsorbate and substrate.
Additionally, it is found that the growth of hBN/Cu(111) is self-limited to one single layer since the reactive Cu(111) surface is obviously essential for the formation of the hBN layer, e.g. for the dehydrogenation of the borazine molecules. As soon as the Cu surface is covered, the growth comes to a halt. By varying the substrate temperature and comparing the growth rates of hBN/Cu(111), the reaction barrier for the growth process is estimated to be (1.2 ± 0.2) eV which is significantly lower than the calculated bond energies for borazine in the gas-phase found in literature [9]. This is attributed to the catalytic effect of the copper surface which reduces the energy barrier significantly and enables the growth of hBN structures at the temperatures applied here.

Combining organic molecules and 2D materials
In the last part of this work, the growth and lateral structure of PTCDA on hBN/Cu(111) is investigated. PTCDA molecules deposited on hBN/Cu(111) samples cover the remaining clean copper surface first, before PTCDA islands nucleate on hBN/Cu(111). These islands do not grow linearly in size but show a step-wise growth mode which can be explained by a critical molecular density close to the islands. Furthermore, all LEED and DF-LEEM results are consistent with the overlayer structure found by Brülke et al. [20]. We both obeserved that 6 domain orientations are strongly preferred for PTCDA on hBN/Cu(111) but that other azimuthal orientations also occur. This azimuthal disorder and the fact that the found overlayer structure is very similar to the one of PTCDA on the weakly interacting Au(111) surface [35, 68, 104] are strong indications for a weak interaction between PTCDA and the hBN layer.

The results of this work are an essential step forward in fundamentally understanding the decisive interplay between different interaction mechanisms for adsorbates on metal surfaces leading to various kinds of growth modes. It was shown that small differences in the involved interaction mechanisms can have great influence on the growth of molecules and 2D materials. This potentially allows to tailor the properties of such systems.

Outlook
Various options exist to investigate the growth of organic molecules and of 2D materials further. The studied systems should be analyzed by theoretical approaches in order to improve the understanding of the observed growth modes. Furthermore, the investigation of similar adsorbate/metal systems would lead to an even better knowledge of the interaction mechanisms in order to control the

self-assembly of these systems. Additionally, new concepts for the production of 2D layer stacks should be taken into account.

In order to understand the observed growth modes even better, the studied systems should be analyzed with theoretical approaches. For example, calculations of the diffusion energy of PTCDA on Cu(001) or the cohesion energy of two of these molecules are desired to compare them with the experimentally observed values.
In the case of NTCDA on Cu(001), pair-potential calculations are able to explain the dendrite-like, fractal growth of NTCDA/Cu(001) on a semi-quantitative level. However, more precise density functional theory (DFT) or ab-initio calculations for the adhesion energies are definitely desired and should give more precise values.
Similarly, the origin of the asymmetry in the adhesion energies for the two possible ways a borazine molecule can attach to an existing hBN island, which leads to three preferred growth directions, might be found by dedicated DFT calculations. However, due to the incommensurate registry between the hBN islands and the substrate, such calculations are difficult and cannot be precise since they have to be performed with periodic boundary conditions which necessitates the assumption of a commensurate structure.
The question, whether it is more favorable to attach a borazine molecule with its boron or nitrogen atom to an already existing hBN island, might be answered experimentally by transmission electron microscopy (TEM). The most difficult part will certainly be finding a suitable way of preparing the hBN sample for TEM.
Furthermore, it would be interesting to observe the transition of dendrite-like growth to compact islands growth for hBN. In principle, this transition should be observed at higher substrate temperatures on Cu(111) although this is of course limited by the melting temperature of the crystal. Therefore, it might be more promising to investigate the growth of hBN on slightly more reactive or thermally more stable substrates. Here, the transition temperature is possibly in an accessible range. In general, the variation of the substrate additionally gives the opportunity to understand the substrate-adsorbate interactions better. For this purpose, additional LEEM studies and possibly also single domain ARPES experiments are of interest. Miriam Raths already started with corresponding investigations on Ni(111) in her Master project.
In order to access the full potential of graphene, hBN and other 2D materials, the production of 2D stacks is desired. However, the growth of hBN on Cu(111) with the precursor borazine is limited to the first layer. Therefore, other substrate/precursor combinations have to be investigated (e.g. [86, 151]). Additionally, new concepts to grow 2D materials might be interesting, as the provision of a gaseous catalyst during the CVD process [163], or approaches which are not based on precursors at all so that catalytic driven dehydrogenation or dissociation is not necessary before the desired 2D material is formed [63, 69, 150].

List of Figures

List of Tables

Bibliography

[1] Afshin Abbasi and Reinhard Scholz. Ab initio calculation of the dispersion interaction between a polyaromatic molecule and a noble metal substrate: PTCDA on Ag(110). *J. Phys. Chem. C*, 113(46):19897–19904, 2009. 52, 55

[2] Deji Akinwande, Nicholas Petrone, and James Hone. Two-dimensional flexible nanoelectronics. *Nat. Commun.*, 5(5678), 2014. 1, 2

[3] Abdullah Al-mahboob, Yasunori Fujikawa, Toshio Sakurai, and Jerzy T. Sadowski. Real-Time Microscopy of Reorientation Driven Nucleation and Growth in Pentacene Thin Films on Silicon Dioxide. *Adv. Funct. Mater.*, 23:2653–2660, 2013. 1

[4] M. S. Altman. Trends in low energy electron microscopy. *J. Phys. Condens. Matter*, 22(8):084017, March 2010. 8, 11

[5] Jacques G. Amar and Fereydoon Family. Critical Cluster Size: Island Morphology and Size Distribution in Submonolayer Epitaxial Growth. *Phys. Rev. Lett.*, 74(11):2066–2069, March 1995. 28, 32

[6] Jacques G. Amar, Fereydoon Family, and Pui-Man Lam. Dynamic Scaling of the Island-Size Distribution and Percolation in a model of Sub-Monolayer Molecular Beam Epitaxy. *MRS Proc.*, 317(12):167, January 1993. 28, 32

[7] W. Auwärter, T. J. Kreutz, T. Greber, and J. Osterwalder. XPD and STM investigation of hexagonal boron nitride on Ni(111). *Surf. Sci.*, 429(1):229–236, 1999. 2, 69, 73, 90

[8] W. Auwärter, M. Muntwiler, J. Osterwalder, and T. Greber. Defect lines and two-domain structure of hexagonal boron nitride films on Ni(111). *Surf. Sci.*, 545(1-2), 2003. 76, 81

[9] Willi Auwärter, Hu Suter, Hermann Sachdev, and Thomas Greber. Synthesis of One Monolayer of Hexagonal Boron Nitride on Ni (111) from B-Trichloroborazine (ClBNH)3. *Chem. Mater.*, 16(2):343–345, 2004. 80, 81, 96, 113

[10] Johannes V. Barth, Giovanni Costantini, and Klaus Kern. Engineering atomic and molecular nanostructures at surfaces. *Nature*, 437(September):671–679, 2005. 29

[11] E. Bauer, M. Mundschau, W. Swiech, and W. Telieps. Surface studies by low-energy electron microscopy (LEEM) and conventional UV photoemission electron microscopy (PEEM). *Ultramicroscopy*, 31(1):49–57, September 1989. 8, 9, 11

[12] E. Bauer, Y. Wei, T. Müller, A. Pavlovska, and I. S. T. Tsong. Reactive crystal growth in two dimensions: Silicon nitride on Si(111). *Phys. Rev. B*, 51(24):17891–17901, June 1995. 8

[13] Ernst Bauer. Low energy electron microscopy. *Reports Prog. Phys.*, 57(9):895–938, September 1994. 5, 8, 9, 10, 11

[14] Oliver Bauer. *Surface bonding of a functionalized aromatic molecule: Adsorption configurations of PTCDA on coinage metal surfaces*. Dissertation, Rheinischen Friedrich-Wilhelms-Universität Bonn, 2014. 98, 99, X

[15] Oliver Bauer, Giuseppe Mercurio, Martin Willenbockel, Werner Reckien, Christoph Heinrich Schmitz, Benjamin Fiedler, Serguei Soubatch, Thomas Bredow, Frank Stefan Tautz, and Moritz Sokolowski. Role of functional groups in surface bonding of planar π-conjugated molecules. *Phys. Rev. B*, 86(23):235431, 2012. 48

[16] Amy Szuchmacher Blum, James G. Kushmerick, David P. Long, Charles H. Patterson, John C. Yang, Jay C. Henderson, Yuxing Yao, James M. Tour, Ranganathan Shashidhar, and Banahalli R. Ratna. Molecularly inherent voltage-controlled conductance switching. *Nat. Mater.*, 4:167–172, 2005. 29

[17] F. C. Bocquet, G. Mercurio, M. Franke, G. van Straaten, S. Weiß, S. Soubatch, C. Kumpf, and F. S. Tautz. Torricelli: A software to determine atomic spatial distributions from normal incidence x-ray standing wave data. *Comput. Phys. Commun., in press*, 2018. 46, 47, 61, 62, V, XIII

[18] A. Bondi. Van der Waals Volumes and Radii. *J. Phys. Chem.*, 68(3):441–451, March 1964. 20, 48, 97, XIII

[19] C. R. Braatz, T. Esat, C. Wagner, R. Temirov, F. S. Tautz, and P. Jakob. Switching orientation of adsorbed molecules: Reverse domino on a metal surface. *Surf. Sci.*, 643:98–107, 2015. 68

[20] Christine Brülke. *private communications*, 2018. 81, 102, 104, 109, 113, X

[21] Christine Brülke, Timo Heepenstrick, Niklas Humberg, Ina Krieger, Moritz Sokolowski, Simon Weiß, Frank Stefan Tautz, and Serguei Soubatch. Long Vertical Distance Bonding of the Hexagonal Boron Nitride Monolayer on the Cu(111) Surface. *J. Phys. Chem. C*, 121(43):23964–23973, November 2017. 2, 18, 69, 73, 76, 81, 85, 87

[22] Christine Brülke, Timo Heepenstrick, Ina Krieger, Xiaosheng Yang, Simon Weiss, Frank Stefan Tautz, Serguei Soubatch, and Moritz Sokolowski. Chemical and electronic decoupling of organic molecules by a monolayer of hexagonal boron nitride. Poster on DPG spring conference, 2018. 3, 97, 104

[23] Harald Brune. Microscopic view of epitaxial metal growth: nucleation and aggregation. *Surf. Sci. Rep.*, 31(4-6):121–229, January 1998. 31

[24] Harald Brune, G. Steven Bales, Joachim Jacobsen, Corrado Boragno, and Klaus Kern. Measuring surface diffusion from nucleation island densities. *Phys. Rev. B*, 60(8):5991–6006, 1999. 31, 33

[25] Marcello Campione, Silvia Caprioli, Massimo Moret, and Adele Sassella. Homoepitaxial Growth of α-Hexathiophene. *J. Phys. Chem. C*, 111(34):12741–12746, August 2007. 25, 32

[26] Tian Carey, Stefania Cacovich, Giorgio Divitini, Jiesheng Ren, Aida Mansouri, Jong M. Kim, Chaoxia Wang, Caterina Ducati, Roman Sordan, and Felice Torrisi. Fully inkjet-printed two-dimensional material field-effect herterojunctions for wearable and textile electronics. *Nat. Commun.*, 8:1202, 2017. 2

[27] W. F. Chung and M. S. Altman. Step contrast in low energy electron microscopy. *Ultramicroscopy*, 74(4):237–246, September 1998. 8, 21

[28] W. F. Chung, Y. J. Feng, H. C. Poon, C. T. Chan, S. Y. Tong, and M. S. Altman. Layer Spacings in Coherently Strained Epitaxial Metal Films. *Phys. Rev. Lett.*, 90(21):216105, May 2003. 9

[29] Beatriz Cordero, Verónica Gómez, Ana E. Platero-Prats, Marc Revés, Jorge Echeverría, Eduard Cremades, Flavia Barragán, and Santiago Alvarez. Covalent radii revisited. *Dalton Trans.*, 0(21):2832–2838, June 2008. 48, XIII

[30] Martina Corso, Willi Auwärter, Matthias Muntwiler, Anna Tamai, Thomas Greber, and Jürg Osterwalder. Boron Nitride Nanomesh. *Science*, 303(5655):217–220, 2004. 2, 69, 90

[31] C. R. Dean, A. F. Young, I. Meric, C. Lee, L. Wang, S. Sorgenfrei, K. Watanabe, T. Taniguchi, P. Kim, K. L. Shepard, and J. Hone. Boron nitride substrates for high-quality graphene electronics. *Nat. Nanotechnol.*, 5(10):722–726, 2010. 2, 69

[32] Hugo Dil, Jorge Lobo-Checa, Robert Laskowski, Peter Blaha, Simon Berner, Jürg Osterwalder, and Thomas Greber. Surface Trapping of Atoms and Molecules with Dipole Rings. *Science*, 319:1824–1827, 2008. 3

[33] Guocai Dong, Elodie B. Fourré, Femke C. Tabak, and Joost W.M. Frenken. How boron nitride forms a regular nanomesh on Rh(111). *Phys. Rev. Lett.*, 104(096102):3–6, 2010. 81

[34] Thomas Duden, Andreas Thust, Christian Kumpf, and F. Stefan Tautz. Focal-Series Reconstruction in Low-Energy Electron Microscopy. *Microsc. Microanal.*, 20(03):968–973, June 2014. 1, 40

[35] S. Duhm, A. Gerlach, I. Salzmann, B. Bröker, R. L. Johnson, F. Schreiber, and N. Koch. PTCDA on Au(111), Ag(111) and Cu(111): Correlation of interface charge transfer to bonding distance. *Org. Electron.*, 9(1):111–118, February 2008. 39, 97, 104, 109, 113

[36] Lukas Eschmann. *Ab-initio Studien der Adsorbat- und Oberflächenzustände von NTCDA auf Ag und Au(111).* Master thesis, Westfälische Wilhelms-Universität Münster, 2017. 52, 55

[37] N. Fairley. CasaXPS, version 2.3.18, Casa Software Ltd, Bay House, 5 Grosvenor Terrace, Teignmouth, Devon TQ14 8NE, UK. 46, 47, V

[38] Fereydoon Family and Paul Meakin. Scaling of the Droplet-Size Distribution in Vapor-Deposited Thin Films. *Phys. Rev. Lett.*, 61(4):428–431, July 1988. 28, 32

[39] Fereydoon Family and Paul Meakin. Kinetics of droplet growth processes: Simulations, theory, and experiments. *Phys. Rev. A*, 40(7):3836–3854, October 1989. 28, 32

[40] Ferdinand H. Farwick zum Hagen, Domenik M. Zimmermann, Caio C. Silva, Christoph Schlueter, Nicolae Atodiresei, Wouter Jolie, Antonio J. Martínez-Galera, Daniela Dombrowski, Ulrike A. Schröder, Moritz Will, Predrag Lazić, Vasile Caciuc, Stefan Blügel, Tien Lin Lee, Thomas Michely, and Carsten Busse. Structure and Growth of Hexagonal Boron Nitride on Ir(111). *ACS Nano*, 10(12):11012–11026, 2016. 76, 81

[41] Janina Felter, Markus Franke, Jana Wolters, Caroline Henneke, and Christian Kumpf. Two-dimensional growth of dendritic islands of NTCDA on Cu(001) studied in real time. *Nanoscale*, 11, 01 2018. 40

[42] Janina Felter, Miriam Raths, Markus Franke, and Christian Kumpf. In-situ study of two-dimensional dendritic growth of hexagonal boron nitride. *2D Materials*, 6, 06 2019. 70

[43] Janina Felter, Jana Wolters, François C. Bocquet, F. Stefan Tautz, and Christian Kumpf. Momentum microscopy on the micrometer scale: Photoemission micro-tomography applied to single molecular domains. *Journal of Physics: Condensed Matter*, 31, 01 2019. 40

[44] R. Fink, D. Gador, U. Stahl, Y. Zou, and E. Umbach. Substrate-dependent lateral order in naphthalene-tetracarboxylic-dianhydride monolayers. *Phys. Rev. B*, 60(4):2818–2826, 1999. 41, 50, 52, 59, 64

[45] Gianluca Fiori, Francesco Bonaccorso, Giuseppe Iannaccone, Tomás Palacios, Daniel Neumaier, Alan Seabaugh, Sanjay K Banerjee, and Luigi Colombo. Electronics based on two-dimensional materials. *Nat. Nanotechnol.*, 9:768–779, 2014. 1, 2

[46] Jan Ingo Flege, Björn Kaemena, Axel Meyer, Jens Falta, Sanjaya D. Senanayake, Jerzy T. Sadowski, R. D. Eithiraj, and Eugene E. Krasovskii. Origin of chemical contrast in low-energy electron reflectivity of correlated multivalent oxides: The case of ceria. *Phys. Rev. B*, 88(23):235428, December 2013. 9

[47] Jan Ingo Flege and Eugene E. Krasovskii. Intensity-voltage low-energy electron microscopy for functional materials characterization. *Phys. status solidi - Rapid Res. Lett.*, 8(6):463–477, June 2014. 9

[48] S. R. Forrest and Y. Zhang. Ultrahigh-vacuum quasiepitaxial growth of model van der Waals thin films. I. Theory. *Phys. Rev. B*, 49(16):11297–11308, April 1994. 20

[49] Stephen R. Forrest. The path to ubiquitous and low-cost organic electronic appliances on plastic. *Nature*, 428:911–918, 2004. 1, 29

[50] Markus Franke. *Vertical, lateral and electronic structure of organic adsorbate systems and 2D materials.* Dissertation, RWTH Aachen, in progress. 18, 40, 44, 46, 47, 48, 49, 52, 53, 57, 60, 61, V, VI, XIII

[51] Torsten Franz. *Elmitec GmbH, Clausthal-Zellerfeld, private communications.* 89

[52] G. Friedel. Sur les symétries cristallines que peut révéler la diffraction des rayons x. *C.R. Acad. Sci. Paris*, 157:1533 – 1536, 1913. 86

[53] D. Gador, C. Buchberger, R. Fink, and E. Umbach. "Manipulation" of molecular orientation in ultrathin organic films: NTCDA on Ag(111). *EPL*, 41(2):231, 1998. 39

[54] Stefan Gärtner, Benjamin Fiedler, Oliver Bauer, Antonela Marele, and Moritz Sokolowski. Lateral ordering of PTCDA on the clean and the oxygen pre-covered Cu(100) surface investigated by scanning tunneling microscopy and low energy electron diffraction. *Beilstein J. Org. Chem.*, 10(100):2055–2064, 2014. 2, 3, 34, 39, 111

[55] A. K. Geim and I. V. Grigorieva. Van der Waals heterostructures. *Nature*, 499:419, 2013. 2, 69

[56] A. Gerlach, S. Sellner, F. Schreiber, N. Koch, and J. Zegenhagen. Substrate-dependent bonding distances of PTCDA: A comparative x-ray standing-wave study on Cu(111) and Ag(111). *Phys. Rev. B*, 75(4):045401, January 2007. 18, 48, 97

[57] K. Glöckler, C. Seidel, A. Soukopp, M. Sokolowski, E. Umbach, M. Böhringer, R. Berndt, and W.-D. Schneider. Highly ordered structures and submolecular scanning tunnelling microscopy contrast of PTCDA and DM-PBDCI monolayers on Ag(111) and Ag(110). *Surf. Sci.*, 405(1):1–20, 1998. 3, 39

[58] Elmitec GmbH. Resolution limit in an elmitec ac-leem 3. https://elmitec.de/AC.php?Bereich=ACLEEM. Accessed: 2017-12-07. 5, 98

[59] ScientaOmicron GmbH. Leedlab and leedcal by scientaomicron. http://www.scientaomicron.direct/85/electron-diffraction/leed-lab. Accessed: 2018-04-16. 11

[60] A. Goriachko, A. A. Zakharov, and H. Over. Oxygen-etching of h-BN/Ru(0001) nanomesh on the nano- and mesoscopic scale. *J. Phys. Chem. C*, 112(28):10423–10427, 2008. 90

[61] Thomas Greber, Louis Brandenberger, Martina Corso, Anna Tamai, and Jürg Osterwalder. Single layer hexagonal boron nitride films on Ni(110). *e-Journal Surf. Sci. Nanotechnol.*, 4:410–413, 2006. 90

[62] Ullrich Groh. Spektromikroskopische Untersuchungen an organischen Nanostrukturen. 2006. 2, 3, 112

[63] Joshua Hall, Borna Pielić, Clifford Murray, Wouter Jolie, Tobias Wekking, Carsten Busse, Marko Kralj, and Thomas Michely. Molecular beam epitaxy of quasi-freestanding transition metal disulphide monolayers on van der Waals substrates: a growth study. *2D Materials*, 5(2):025005, 2018. 114

[64] Tae-Hee Han, Youngbin Lee, Mi-Ri Choi, Seong-Hoon Woo, Sang-Hoon Bae, Byung Hee Hong, Jong-Hyun Ahn, and Tae-Hoo Lee. Extremely efficient flexible organic light-emitting diodes with modified graphene anode. *Nat. Photonics*, 6:105–110, 2012. 1, 2

[65] A. Hauschild, K. Karki, B. C. C. Cowie, M. Rohlfing, F. S. Tautz, and M. Sokolowski. Molecular distortions and chemical bonding of a large π-conjugated molecule on a metal surface. *Phys. Rev. Lett.*, 94(3):036106, 2005. 48

[66] Caroline Henneke. *Kinetic and thermodynamic considerations on the formation of heteromolecular layers on metal surfaces.* Dissertation, RWTH Aachen, 2015. 2, 11, 13, 16, 21, 25, 29, 30, 31, 32, 33, 34, 100, 111, III

[67] Caroline Henneke, Janina Felter, Daniel Schwarz, F. Stefan Tautz, and Christian Kumpf. Heteromolecular phases by utilizing intermolecular repulsion. *Nat. Mater.*, 16(June):628–634, 2017. 1, 40, 41

[68] S. K. M. Henze, O. Bauer, T.-L. Lee, M. Sokolowski, and F. S. Tautz. Vertical bonding distances of PTCDA on Au(111) and Ag(111): Relation to the bonding type. *Surf. Sci.*, 601(6):1566–1573, March 2007. 18, 19, 48, 104, 109, 113

[69] Charlotte Herbig, Timo Knispel, Sabina Simon, Ulrike A. Schröder, Antonio J. Martínez-Galera, Mohammad A. Arman, Christian Teichert, Jan Knudsen, Arkady V. Krasheninnikov, and Thomas Michely. From Permeation to Cluster Arrays: Graphene on Ir(111) Exposed to Carbon Vapor. *Nano Letters*, 17(5):3105–3112, 2017. 114

[70] Christoph Herrmann, Pavlo Omelchenko, and Karen L. Kavanagh. Growth of h-BN on copper (110) in a LEEM. *Surf. Sci.*, 669:133–139, 2018. 73

[71] Gregor Hlawacek, Fawad S. Khokhar, Raoul Van Gastel, Bene Poelsema, and Christian Teichert. Smooth growth of organic semiconductor films on graphene for high-efficiency electronics. *Nano Lett.*, 11(2):333–337, 2011. 1

[72] Gregor Hlawacek, Peter Puschnig, Paul Frank, Adolf Winkler, Claudia Ambrosch-Draxl, and Christian Teichert. Characterization of Step-Edge Barriers in Organic Thin-Film Growth. *Science*, 321(5885):108–111, July 2008.

[73] Gregor Hlawacek and Christian Teichert. Nucleation and growth of thin films of rod-like conjugated molecules. *J. Phys. Condens. Matter*, 25(14):143202, 2013. 1

[74] I. Horcas, R. Fernández, J. M. Gómez-Rodríguez, J. Colchero, J. Gómez-Herrero, and A. M. Baró. WSxM: A software for scanning probe microscopy and a tool for nanotechnology. *Review of Scientific Instruments*, 78(013705), 2007. 18

[75] Harald Ibach. *Physics of Surfaces and Interfaces*. Springer-Verlag, 2006. 10

[76] Julian Ikonomov, Oliver Bauer, and Moritz Sokolowski. Highly ordered thin films of perylene-3,4,9,10-tetracarboxylic acid dianhydride (PTCDA) on Ag(100). *Surf. Sci.*, 602(12):2061–2068, 2008. 3, 39

[77] Rashid Ilmi, Ashanul Haque, and M. S. Khan. High efficiency small molecule-based donor materials for organic solar cells. *Org. Electron.*, 58:53–62, 2018. 1

[78] A. Jabloniski, F. Salvat, and C. J. Powell. NIST Electron Elastic-Scattering Cross-Section Database Version 3.2, 2010. 61

[79] B. T. Jonker, N. C. Bartelt, and Robert L. Park. Quantum size effect in electron transmission through Cu and Ag films on W(110). *Surf. Sci.*, 127(2):183–199, April 1983. 9

[80] S. Joshi, D. Ecija, R. Koitz, M. Iannuzzi, A. P. Seitsonen, J. Hutter, H. Sachdev, S. Vijayaraghavan, F. Bischoff, K. Seufert, J. V. Barth, and W. Auwärter. Boron Nitride on Cu (111): An Electronically Corrugated Monolayer. *Nano Lett.*, 12(111):5821–5828, 2012. 2, 69

[81] Hironori Kaji, Hajime Suzuki, Tatsuya Fukushima, Katsuyuki Shizu, Katsuaki Suzuki, Shosei Kubo, Takeshi Komino, Hajime Oiwa, Furitsu Suzuki, Atsushi Wakamiya, Yasujiro Murata, and Chihaya Adachi. Purely organic electroluminescent material realizing 100% conversion from electricity to light. *Nat. Commun.*, 6:8476, 2015. 1, 29

[82] Fawad S. Khokhar, Raoul Van Gastel, and Bene Poelsema. Role of topographical defects in organic film growth of 4, 4'-biphenyldicarboxylic acid on graphene: A low-energy electron microscopy study. *Phys. Rev. B*, 82(205409):1–8, 2010. 1

[83] Piran R. Kidambi, Raoul Blume, Jens Kling, Jakob B. Wagner, Carsten Baehtz, Robert S. Weatherup, Robert Schloegl, Bernhard C. Bayer, and Stephan Hofmann. In situ observations during chemical vapor deposition of hexagonal boron nitride on polycrystalline copper. *Chem. Mater.*, 26(22):6380–6392, 2014. 81

[84] L. Kilian, A. Hauschild, R. Temirov, S. Soubatch, A. Schöll, A. Bendounan, F. Reinert, T.-L. Lee, F. S. Tautz, M. Sokolowski, and E. Umbach. Role of Intermolecular Interactions on the Electronic and Geometric Structure of

a Large π-Conjugated Molecule Adsorbed on a Metal Surface. *Phys. Rev. Lett.*, 100:136103, Apr 2008. 39

[85] L. Kilian, U. Stahl, I. Kossev, M. Sokolowski, R. Fink, and E. Umbach. The commensurate-to-incommensurate phase transition of an organic monolayer: A high resolution LEED analysis of the superstructures of NTCDA on Ag(111). *Surf. Sci.*, 602(14):2427–2434, 2008. 39

[86] K. K. Kim, A. Hsu, X. Jia, S. M. Kim, Y. Shi, M. Hofmann, D. Nezich, J. F. Rodriguez-Nieva, M. Dresselhaus, T. Palacios, and J. Kong. Synthesis of Monolayer Boron Nitride on Cu Foil Using Chemical Vapor Deposition. *Nano Lett.*, 12:161–166, 2011. 2, 69, 114

[87] Charles Kittel. *Einführung in die Festkörperphysik*. R. Oldenbourg Verlag, 12th edition, 1999. 10

[88] Christoph Kleimann, Benjamin Stadtmüller, Sonja Schröder, and Christian Kumpf. Electrostatic Interaction and Commensurate Registry at the Heteromolecular F_{16}CuPc–CuPc Interface. *J. Phys. Chem. C*, 118(3):1652–1660, 2014. 52

[89] H. Koezuka, A. Tsumura, and T. Ando. Field-effect transistor with polythiophene thin film. *Synthetic Metals*, 18(1):699 – 704, 1987. Proceedings of the International Conference of Science and Technology of Synthetic Metals. 1

[90] A. Kraft, R. Temirov, S. K. M. Henze, S. Soubatch, M. Rohlfing, and F. S. Tautz. Lateral adsorption geometry and site-specific electronic structure of a large organic chemisorbate on a metal surface. *Phys. Rev. B*, 74(4):041402, July 2006. 62

[91] Ingo Kröger. *Adsorption von Phthalocyaninen auf Edelmetalloberflächen*. Dissertation, Universität Würzburg, 2011. 19

[92] Ingo Kröger, Patrick Bayersdorfer, Benjamin Stadtmüller, Christoph Kleimann, Giuseppe Mercurio, Friedrich Reinert, and Christian Kumpf. Submonolayer growth of H_2-phthalocyanine on Ag (111). *Phys. Rev. B*, 86:195412, 2012. 39

[93] Ingo Kröger, Benjamin Stadtmüller, and Christian Kumpf. Submonolayer and multilayer growth of titaniumoxide-phthalocyanine on Ag (111). *New J. Phys.*, 18:113022, 2016. 52

[94] Ingo Kröger, Benjamin Stadtmüller, Christoph Stadler, Johannes Ziroff, Mario Kochler, Andreas Stahl, Florian Pollinger, Tien Lin Lee, Jörg Zegenhagen, Friedrich Reinert, and Christian Kumpf. Submonolayer growth of copper-phthalocyanine on Ag(111). *New J. Phys.*, 12(8):083038, August 2010. 40, 41

[95] Ingo Kröger, Benjamin Stadtmüller, Christian Wagner, Christian Weiss, Ruslan Temirov, F. Stefan Tautz, and Christian Kumpf. Modeling intermolecular interactions of physisorbed organic molecules using pair potential

calculations. *J. Chem. Phys.*, 135(23):234703, December 2011. 19, 20, 34, 35, 36, 39, 40, 41, 52

[96] Avijit Kumar, Kaustuv Banerjee, and Peter Liljeroth. Molecular assembly on two-dimensional materials. *Nanotechnology*, 28:082001, 2017. 3

[97] Markus Lackinger, Stefan Griessl, Wolfgang M. Heckl, and Michael Hietschold. Coronene on Ag(111) investigated by LEED and STM in UHV. *J. Phys. Chem. B*, 106(17):4482–4485, 2002. 39

[98] R. Laskowski, P. Blaha, T. Gallauner, and K. Schwarz. Single-Layer Model of the Hexagonal Boron Nitride Nanomesh on the Rh(111) Surface. *Phys. Rev. Lett.*, 98:106802, 2007. 2, 69

[99] Jiong Lu, Pei Shan Emmeline Yeo, Yi Zheng, Hai Xu, Chee Kwan Gan, Michael B. Sullivan, A. H. Castro Neto, and Kian Ping Loh. Step flow versus mosaic film growth in hexagonal boron nitride. *J. Am. Chem. Soc.*, 135(6):2368–2373, 2013. 76, 81, 90

[100] D. Lüftner, Thomas Ules, Eva Maria Reinisch, Georg Koller, Serguei Soubatch, F. Stefan Tautz, Michael G. Ramsey, and Peter Puschnig. Imaging the wave functions of adsorbed molecules. *Proc. Natl. Acad. Sci.*, 111(2):605–610, January 2014. 15

[101] Hans Lüth. *Solid Surfaces, Interfaces and Thin Films*. Springer-Verlag, 3rd edition, 2001. 10

[102] Florian C. Maier. *Spectromicroscopic characterisation of the formation of complex interfaces*. Dissertation, Julius-Maximilians Universität Würzburg, 2010. 3

[103] Icarus K. H. Man and M. S. Altman. Low-energy electron microscopy of layer spacings and quantum electronic structure of ultrathin films. *Surf. Interface Anal.*, 37(2):235–238, February 2005. 9

[104] S. Mannsfeld, M. Toerker, T. Schmitz-Hübsch, F. Sellam, T. Fritz, and K. Leo. Combined LEED and STM study of PTCDA growth on reconstructed Au(111) and Au(100) single crystals. *Org. Electron.*, 2(3-4):121–134, December 2001. 39, 104, 109, 113

[105] H. Marchetto. *High-resolution spectro-microscopic investigations of organic thin film growth*. Phd thesis, Frei Universität Berlin, 2006. 31

[106] H. Marchetto, U. Groh, Thomas Schmidt, R. Fink, H.-J. Freund, and E. Umbach. Influence of substrate morphology on organic layer growth: PTCDA on Ag(111). *Chem. Phys.*, 325(1):178–184, June 2006. 3, 31, 39

[107] Helder Marchetto, Thomas Schmidt, Ullrich Groh, Florian C. Maier, Pierre L. Levesque, Rainer Fink, H. J. Freund, and Eberhard Umbach. Direct observation of epitaxial organic film growth: temperature-dependent growth mechanisms and metastability. *Phys. Chem. Chem. Phys.*, 17:29150–29160, 2015. 1, 3, 39, 40, 41

[108] Giuseppe Mercurio. *Study of molecule-metal interfaces by means of the Normal Incidence X-ray Standing Wave technique*. Dissertation, RWTH Aachen, 2012. 18

[109] Frank-J. Meyer zu Heringdorf, M. C. Reuter, and R. M. Tromp. Growth dynamics of pentacene thin films. *Nature*, 412(6846):517–520, August 2001. 1

[110] Thomas Michely and Joachim Krug. *Islands, Mounds and Atoms: Crystal Growth far from Equilibrium*. Springer-Verlag, Berlin, Heidelberg, 2004. 25, 27, 78, 92

[111] Frank Müller and Samuel Grandthyll. Monolayer formation of hexagonal boron nitride on Ag(001). *Surf. Sci.*, 617:207–210, 2013. 73, 81, 90

[112] Frank Müller, Stefan Hüfner, Hermann Sachdev, Robert Laskowski, Peter Blaha, and Karlheinz Schwarz. Epitaxial growth of hexagonal boron nitride on Ag(111). *Phys. Rev. B*, 82(11):113406, 2010. 2, 69, 81, 90

[113] W. W. Mullins. The statistical self-similarity hypothesis in grain growth and particle coarsening. *J. Appl. Phys.*, 59(4):1341–1349, February 1986. 32

[114] M. Mundschau, E. Bauer, and W. Świech. Initial epitaxial growth of Cu on Mo(001) by low-energy electron microscopy and photoemission electron microscopy. *J. Appl. Phys.*, 65(2):581–584, January 1989. 9

[115] Alpha T. N'Diaye, Raoul van Gastel, Antonio J. Martínez-Galera, Johann Coraux, Hichem Hattab, Dirk Wall, Frank-J. Meyer zu Heringdorf, Michael Horn-von Hoegen, José M. Gómez-Rodríguez, Bene Poelsema, Carsten Busse, and Thomas Michely. In situ observation of stress relaxation in epitaxial graphene. *New J. Phys.*, 11(11):113056, November 2009. 8

[116] K. S. Novoselov, A. K. Geim, S. V. Morozov, D. Jiang, Y. Zhang, S. V. Dubonos, I. V. Grigorieva, and A. A. Firsov. Electric Field Effect in Atomically Thin Carbon Films. *Science*, 306:666–670, 2004. 2

[117] Fabrizio Orlando, Rosanna Larciprete, Paolo Lacovig, Ilan Boscarato, Alessandro Baraldi, and Silvano Lizzit. Epitaxial Growth of Hexagonal Boron Nitride on Ir(111). *J. Phys. Chem. C*, 116(111):157–164, 2012. 73, 81, 90

[118] Marin Petrović, Ulrich Hagemann, Michael Horn-von Hoegen, and Frank J. Meyer zu Heringdorf. Microanalysis of single-layer hexagonal boron nitride islands on Ir(111). *Appl. Surf. Sci.*, 420:504–510, 2017. 73, 81

[119] T. Potocar, S. Lorbek, D. Nabok, Q. Shen, L. Tumbek, G. Hlawacek, P. Puschnig, C. Ambrosch-Draxl, C. Teichert, and A. Winkler. Initial stages of a para-hexaphenyl film growth on amorphous mica. *Phys. Rev. B*, 83(7):075423, February 2011. 28, 32, 35

[120] A. B. Preobrajenski, M. A. Nesterov, M. L. Ng, A. S. Vinogradov, and N. Mårtensson. Monolayer h-BN on Lattice-Mismatched Metal Surfaces: On the Formation of the Nanomesh. *Chem. Phys. Lett.*, 446:119–123, 2007. 2, 69

[121] A. B. Preobrajenski, A. S. Vinogradov, and N. Mårtensson. Monolayer of h-BN chemisorbed on Cu(111) and Ni(111): The role of the transition metal 3d states. *Surf. Sci.*, 582(1-3):21–30, 2005. 81, 90

[122] A. B. Preobrajenski, A. S. Vinogradov, May Ling Ng, E. Ćavar, R. Westerström, A. Mikkelsen, E. Lundgren, and N. Mårtensson. Influence of chemical interaction at the lattice-mismatched h-BN/Pt (111) interfaces on the overlayer morphology. *Phys. Rev. B*, 75(245412):245412, 2007. 2, 69

[123] P. Puschnig, S. Berkebile, A. J. Fleming, G. Koller, K. Emtsev, T. Seyller, J. D. Riley, C. Ambrosch-Draxl, F. P. Netzer, and M. G. Ramsey. Reconstruction of Molecular Orbital Densities from Photoemission Data. *Science*, 326(5953):702–706, October 2009. 14, 15, 16, 62

[124] P. Puschnig, E.-M. Reinisch, T. Ules, G. Koller, S. Soubatch, M. Ostler, L. Romaner, F. S. Tautz, C. Ambrosch-Draxl, and M. G. Ramsey. Orbital tomography: Deconvoluting photoemission spectra of organic molecules. *Phys. Rev. B*, 84(23):235427, December 2011. 15, 16

[125] Gerold M. Rangger, Oliver T. Hofmann, Lorenz Romaner, Georg Heimel, Benjamin Bröker, Ralf Peter Blum, Robert L. Johnson, Norbert Koch, and Egbert Zojer. F4TCNQ on Cu, Ag, and Au as prototypical example for a strong organic acceptor on coinage metals. *Phys. Rev. B*, 79(16):165306, 2009. 52, 55

[126] Michael Rohlfing, Ruslan Temirov, and Frank Stefan Tautz. Adsorption structure and scanning tunneling data of a prototype organic-inorganic interface: PTCDA on Ag(111). *Phys. Rev. B*, 76(11):115421, September 2007. 48, 52

[127] Lorenz Romaner, Georg Heimel, Jean Luc Brédas, Alexander Gerlach, Frank Schreiber, Robert L. Johnson, Jörg Zegenhagen, Steffen Duhm, Norbert Koch, and Egbert Zojer. Impact of bidirectional charge transfer and molecular distortions on the electronic structure of a metal-organic interface. *Phys. Rev. Lett.*, 99(25):256801, 2007.

[128] Lorenz Romaner, D. Nabok, P. Puschnig, E. Zojer, and C. Ambrosch-Draxl. Theoretical study of PTCDA adsorbed on the coinage metal surfaces, Ag(111), Au(111) and Cu(111). *New J. Phys.*, 11(5):053010, May 2009. 52, 55

[129] Ricardo Ruiz, Bert Nickel, Norbert Koch, Leonard C. Feldman, Richard F. Haglund, Antoine Kahn, Fereydoon Family, and Giacinto Scoles. Dynamic Scaling, Island Size Distribution, and Morphology in the Aggregation Regime of Submonolayer Pentacene Films. *Phys. Rev. Lett.*, 91(13):136102, September 2003. 25, 28, 32

[130] Johannes Schindelin, Ignacio Arganda-Carreras, Erwin Frise, Verena Kaynig, Mark Longair, Tobias Pietzsch, Stephan Preibisch, Curtis Rueden, Stephan Saalfeld, Benjamin Schmid, Jean-Yves Tinevez, Daniel James White, Volker Hartenstein, Kevin Eliceiri, Pavel Tomancak, and Albert Cardona. Fiji: an open-source platform for biological-image analysis. *Nat. Methods*, 9(7):676–682, July 2012. 16, 17

[131] A. Schmidt, T. J. Schuerlein, G. E. Collins, and N. R. Armstrong. Ordered Ultrathin Films of Perylenetetracarboxylic Dianhydride (PTCDA) and Dimethylperylenebis(dicarboximide) (Me-PTCDI) on Cu(100): Characterization of Structure and Surface Stoichiometry by LEED, TDMS, and XPS. *J. Phys. Chem.*, 99(30):11770–11779, 1995. 34

[132] Thomas Schmidt, Helder Marchetto, Ullrich Groh, Rainer H. Fink, Hans-Joachim Freund, and Eberhard Umbach. Influence of Substrate Bonding and Surface Morphology on Dynamic Organic Layer Growth: Perylenetetracarboxylic Dianhydride on Au(111). *Langmuir*, 34(19):5444–5453, 2018. 40

[133] Tobias D. Schmidt, Thomas Lampe, Daniel Sylvinson M. R., Peter I. Djurovich, Mark E. Thompson, and Wolfgang Brütting. Emitter Orientation as a Key Parameter in Organic Light-Emitting Diodes. *Phys. Rev. Appl.*, 8:037001, 2017. 1

[134] Stefan Schmitt, Achim Schöll, and Eberhard Umbach. Long-range surface faceting induced by chemisorption of PTCDA on stepped Ag(111) surfaces. *Surf. Sci.*, 643:59 – 64, 2016. 40

[135] Caroline A. Schneider, Wayne S. Rasband, and Kevin W. Eliceiri. NIH Image to ImageJ: 25 years of image analysis. *Nat. Methods*, 9(7):671–675, July 2012. 16

[136] K. Schönauer, S. Weiss, V. Feyer, D. Lüftner, B. Stadtmüller, D. Schwarz, T. Sueyoshi, C. Kumpf, P. Puschnig, M. G. Ramsey, F. S. Tautz, and S. Soubatch. Charge transfer and symmetry reduction at the CuPc/Ag(110) interface studied by photoemission tomography. *Phys. Rev. B*, 94:205144, Nov 2016. 52

[137] Fabian Schulz, Robert Drost, Sampsa K. Hämäläinen, Thomas Demonchaux, Ari P. Seitsonen, and Peter Liljeroth. Epitaxial hexagonal boron nitride on Ir(111): A work function template. *Phys. Rev. B*, 89(235429):235429, 2014. 2, 69

[138] Fabian Schulz, Robert Drost, Sampsa K. Hämäläinen, and Peter Liljeroth. Templated self-assembly and local doping of molecules on epitaxial hexagonal boron nitride. *ACS Nano*, 7(12):11121–11128, 2013. 3, 69

[139] Daniel Schwarz. *Visualization of nucleation and growth of supramolecular networks on Cu(001) and Au(111)* . Dissertation, Universiteit Twente, 2012. 12, 16

[140] Daniel Schwarz, Caroline Henneke, and Christian Kumpf. Towards functionalization of graphene: in situ study of the nucleation of copper-phtalocyanine on graphene. *New J. Phys.*, 18(2):023034, February 2016. 1, 8, 40

[141] Daniel Schwarz, Raoul van Gastel, Harold J. W. Zandvliet, and Bene Poelsema. Phase transformations of 4,4'-biphenyldicarboxylic acid on Cu(001). *Phys. Rev. B*, 85(23):235419, June 2012. 1, 40, 101

[142] Daniel Schwarz, Raoul van Gastel, Harold J. W. Zandvliet, and Bene Poelsema. Size Fluctuations of Near Critical Nuclei and Gibbs Free Energy for Nucleation of BDA on Cu(001). *Phys. Rev. Lett.*, 109(1):016101, July 2012. 101

[143] Daniel Schwarz, Raoul van Gastel, Harold J. W. Zandvliet, and Bene Poelsema. Formation and decay of a compressed phase of 4,4'-biphenyldicarboxylic acid on Cu(001). *Phys. Chem. Chem. Phys.*, 15(14):5007, 2013. 8

[144] Martin Schwarz, Alexander Riss, Manuela Garnica, Jacob Ducke, Peter S. Deimel, David A. Duncan, Pardeep Kumar Thakur, Tien-Lin Lee, Ari Paavo Seitsonen, Johannes V. Barth, Francesco Allegretti, and Willi Auwärter. Corrugation in the Weakly Interacting Hexagonal-BN/Cu(111) System: Structure Determination by Combining Noncontact Atomic Force Microscopy and X-ray Standing Waves. *ACS Nano*, 11(9):9151–9161, 2017. 69

[145] Roy A. Scott and Harold A. Scheraga. Method for Calculating Internal Rotation Barriers. *J. Chem. Phys.*, 42(6):2209–2215, March 1965. 20

[146] C. Seidel, J. Poppensieker, and H. Fuchs. Real-time monitoring of phase transitions of vacuum deposited organic films by molecular beam deposition LEED. *Surf. Sci.*, 408(1):223 – 231, 1998. 39

[147] J. Sforzini, P. Hapala, M. Franke, G. van Straaten, A. Stöhr, S. Link, S. Soubatch, P. Jelínek, T.-L. Lee, U. Starke, M. Švec, F. C. Bocquet, and F. S. Tautz. Structural and Electronic Properties of Nitrogen-Doped Graphene. *Phys. Rev. Lett.*, 116(12):126805, March 2016. 18

[148] J. Sforzini, L. Nemec, T. Denig, B. Stadtmüller, T.-L. Lee, C. Kumpf, S. Soubatch, U. Starke, P. Rinke, V. Blum, F. C. Bocquet, and F. S. Tautz. Approaching Truly Freestanding Graphene: The Structure of Hydrogen-Intercalated Graphene on 6H-SiC(0001). *Phys. Rev. Lett.*, 114(10):106804, March 2015. 18

[149] Jai Shanker, P. S. Bakhshi, and L. P. Sharma. Analysis of the crystal binding and the Anderson-Gruneisen parameters in the halides of copper(I), silver(I) and thallium(I). *J. Inorg. Nucl. Chem.*, 41(9):1285–1288, January 1979. 20

[150] Ha-Chul Shin, Yamujin Jang, Tae-Hoon Kim, Jun-Hae Lee, Dong-Hwa Oh, Sung Joon Ahn, Jae Hyun Lee, Youngkwon Moon, Ji-Hoon Park, Sung Jong Yoo, Chong-Yun Park, Dongmok Whang, Cheol-Woong Yang, and Joung Real Ahn. Epitaxial Growth of a Single-Crystal Hybridized Boron Nitride and Graphene Layer on a Wide-Band Gap Semiconductor. *J. Am. Chem. Soc.*, 137(21):6897–6905, 2015. 114

[151] Gene Siegel, Cristian V. Ciobanu, Badri Narayanan, Michael Snure, and Stefan C. Badescu. Heterogeneous Pyrolysis: A Route for Epitaxial Growth of hBN Atomic Layers on Copper Using Separate Boron and Nitrogen Precursors. *Nano Lett.*, 17(4):2404–2413, 2017. 2, 69, 114

[152] L. Song, L. Ci, H. Lu, P. B. Sorokin, C. Jin, J. Ni, A. G. Kvashnin, D. G. Kvashnin, J. Lou, B. I. Yakobson, and M. A. Pulickel. Large Scale Growth and Characterization of Atomic Hexagonal Boron Nitride. *Nano Lett.*, 10:3209–3215, 2010. 2, 69

[153] C. Stadler, S. Hansen, A. Schöll, T.-L. Lee, J. Zegenhagen, C. Kumpf, and E. Umbach. Molecular distortion of NTCDA upon adsorption on Ag(111): a normal incidence x-ray standing wave study. *New J. Phys.*, 9(3):50–50, March 2007. 48

[154] Christoph Stadler, Sören Hansen, Ingo Kröger, Christian Kumpf, and Eberhard Umbach. Tuning intermolecular interaction in long-range-ordered submonolayer organic films. *Nat. Phys.*, 5(2):153–158, February 2009. 1, 18, 39, 40, 41

[155] B. Stadlober, U. Haas, H. Maresch, and A. Haase. Growth model of pentacene on inorganic and organic dielectrics based on scaling and rate-equation theory. *Phys. Rev. B*, 74(16):165302, October 2006. 25, 28, 32

[156] B. Stadtmüller, M. Willenbockel, E. M. Reinisch, T. Ules, F. C. Bocquet, S. Soubatch, P. Puschnig, G. Koller, M. G. Ramsey, F. S. Tautz, and C. Kumpf. Orbital tomography for highly symmetric adsorbate systems. *EPL*, 100(2):26008, October 2012. 15, 16, 18, 39, 62

[157] Benjamin Stadtmüller. *Study of intermolecular interactions in hetero-organic thin films*. Dissertation, RWTH Aachen, 2013. 18

[158] Benjamin Stadtmüller, Caroline Henneke, Serguei Soubatch, F. Stefan Tautz, and Christian Kumpf. Tailoring metal–organic hybrid interfaces: heteromolecular structures with varying stoichiometry on Ag(111). *New J. Phys.*, 17(2):023046, 2015. 1, 40, 52

[159] Benjamin Stadtmüller, Ingo Kröger, Friedrich Reinert, and Christian Kumpf. Submonolayer growth of CuPc on noble metal surfaces. *Phys. Rev. B*, 83(8):085416, February 2011. 39, 40, 41

[160] Benjamin Stadtmüller, Daniel Lüftner, Martin Willenbockel, Eva Maria Reinisch, Tomoki Sueyoshi, Georg Koller, Serguei Soubatch, Michael G.

Ramsey, Peter Puschnig, F. Stefan Tautz, and Christian Kumpf. Unexpected interplay of bonding height and energy level alignment at heteromolecular hybrid interfaces. *Nat. Commun.*, 5(3685):1–7, April 2014. 1, 15, 16, 18, 63

[161] P. Sutter, J. Lahiri, P. Albrecht, and E. Sutter. Chemical vapor deposition and etching of high-quality monolayer hexagonal boron nitride films. *ACS Nano*, 5(9):7303–7309, 2011. 2, 69, 73, 90

[162] C. W. Tang and S. A. Vanslyke. Organic electroluminescent diodes. *Appl. Phys. Lett.*, 51:913, 1987. 1, 29

[163] Shujie Tang, Haomin Wang, Hui Shan Wang, Qiujuan Sun, Xiuyun Zhang, Chunxiao Cong, Hong Xie, Xiaoyu Liu, Xiaohao Zhou, Fuqiang Huang, Xiaoshuang Chen, Ting Yu, Feng Ding, Xiaoming Xie, and Mianheng Jiang. Silane-catalysed fast growth of large single-crystalline graphene on hexagonal boron nitride. *Nat. Comm.*, 6:6499, 2015. 114

[164] F. S. Tautz. Structure and bonding of large aromatic molecules on noble metal surfaces: The example of PTCDA. *Prog. Surf. Sci.*, 82(9-12):479–520, September 2007. 1

[165] M. Tejima, K. Kita, K. Kyuno, and A. Toriumi. Study on the growth mechanism of pentacene thin films by the analysis of island density and island size distribution. *Appl. Phys. Lett.*, 85(17):3746–3748, October 2004. 25, 28, 32, 34, 35

[166] W. Telieps and E. Bauer. The (7 x 7) to (1 x 1) phase transition on Si(111). *Surf. Sci.*, 162(1-3):163–168, October 1985. 8

[167] R. Temirov, S. Soubatch, A. Luican, and F. S. Tautz. Free-electron-like dispersion in an organic monolayer film on a metal substrate. *Nature*, 444(7117):350–353, 2006. 39

[168] Yongfeng Tong, Francois Nicolas, Stefan Kubsky, Hamid Oughaddou, Fausto Sirotti, Vladimir Esaulov, and Azzedine Bendounan. Interplay between Structural and Electronic Properties in NTCDA Films on Cu(100). *J. Phys. Chem. C*, 121(9):5050–5057, 2017. 44, 49, 64

[169] M. B. Trzhaskovskaya, V. I. Nefedov, and V. G. Yarzhemsky. Photoelectron angular distribution parameters for elements Z=1 to Z=54 in the photoelectron energy range 100–5000 eV. *At. Data Nucl. Data Tables*, 77(1):97–159, January 2001. 61

[170] M. B. Trzhaskovskaya, V. I. Nefedov, and V. G. Yarzhemsky. Photoelectron angular distribution parameters for elements Z=55 to Z=100 in the photoelectron energy range 100–5000 eV. *At. Data Nucl. Data Tables*, 82(2):257–311, November 2002. 61

[171] Nobuo Ueno and Satoshi Kera. Electron spectroscopy of functional organic thin films: Deep insights into valence electronic structure in relation to charge transport property. *Prog. Surf. Sci.*, 83(10-12):490–557, December 2008. 1, 29, 39

[172] E. Umbach, K. Glöckler, and M. Sokolowski. Surface "architecture" with large organic molecules: interface order and epitaxy. *Surf. Sci.*, 402-404:20 – 31, 1998. 39

[173] Jonas van Bebber. *Untersuchung des Wachstums von Kupferphthalocyanin auf Cu(001) mit niederenergetischen Elektronen*. Master thesis, RWTH Aachen, 2014. 23

[174] Michel A. Van Hove, William H. Weinberg, and Chi-Ming Chan. *Low-Energy Electron Diffraction*. Springer-Verlag, 1986. 10

[175] Gerben van Straaten, Markus Franke, François C. Bocquet, F. Stefan Tautz, and Christian Kumpf. Non-dipolar effects in photoelectron-based normal incidence X-ray standing wave experiments. *J. Electron. Spectrosc. Relat. Phenom.*, 222:106–116, January 2018. 46, 61, 62, XIII

[176] Gerben van Straaten, Markus Franke, Serguei Soubatch, Benjamin Stadtmüller, David A. Duncan, Tien-Lin Lee, F. Stefan Tautz, and Christian Kumpf. Role of the Central Metal Atom in Substrate-Mediated Molecular Interactions in Phthalocyanine-Based Heteromolecular Monolayers. *J. Phys. Chem. C*, 122(15):8491–8504, April 2018. 39, 41

[177] J. A. Venables. Nucleation and growth of thin films. *Vacuum*, 33(10-12):701–705, October 1983. 31, 33

[178] J. A. Venables. Nucleation calculations in a pair-binding model. *Phys. Rev. B*, 36(8):4153–4162, September 1987. 31

[179] Tamás Vicsek and Fereydoon Family. Dynamic Scaling for Aggregation of Clusters. *Phys. Rev. Lett.*, 52(19):1669–1672, May 1984. 28, 32

[180] Bert Voigtländer. *Scanning Probe Microscopy*. Springer-Verlag, 2015. 18

[181] Th. Wagner, A. Bannani, C. Bobisch, H. Karacuban, and R. Möller. The initial growth of PTCDA on Cu(111) studied by STM. *J. Phys. Condens. Matter*, 19(5):056009, February 2007. 39, 97, 98

[182] Th. Wagner, H. Karacuban, A. Bannani, C. Bobisch, and R. Möller. Thermal desorption of PTCDA on Cu(111). *J. Phys. Conf. Ser.*, 100(5):052068, March 2008. 98

[183] D. Walton. Nucleation of Vapor Deposits. *J. Chem. Phys.*, 37(10):2182–2188, November 1962. 27

[184] Kenji Watanabe, Takashi Taniguchi, and Hisao Kanda. Direct-bandgap properties and evidence for ultraviolet lasing of hexagonal boron nitride single crystal. *Nat. Mater.*, 3(6):404–409, June 2004. 2, 69, 97

[185] S. Weiß, D. Lüftner, T. Ules, E. M. Reinisch, H. Kaser, A. Gottwald, M. Richter, S. Soubatch, G. Koller, M. G. Ramsey, F. S. Tautz, and P. Puschnig. Exploring three-dimensional orbital imaging with energy-dependent photoemission tomography. *Nat. Commun.*, 6(1):8287, December 2015. 15

[186] Simon Weiß, Ina Krieger, Timo Heepenstrick, Serguei Soubatch, Moritz Sokolowski, and F. Stefan Tautz. Determination of the adsorption geometry of PTCDA on the Cu(100) surface. *Phys. Rev. B*, 96(7):075414, August 2017. 48

[187] M. Wießner, J. Kübert, V. Feyer, P. Puschnig, A. Schöll, and F. Reinert. Lateral band formation and hybridization in molecular monolayers: NTCDA on Ag(110) and Cu(100). *Phys. Rev. B*, 88(7):075437, 2013. 49

[188] M. Willenbockel, D. Lüftner, B. Stadtmüller, G. Koller, C. Kumpf, S. Soubatch, P. Puschnig, M. G. Ramsey, and F. S. Tautz. The interplay between interface structure, energy level alignment and chemical bonding strength at organic-metal interfaces. *Phys. Chem. Chem. Phys.*, 17:1530–1548, 2015. 39

[189] T. A. Witten, jr. and L. M. Sander. Diffusion-Limited Aggregation, a Kinetic Critical Phenomenon. *Phys. Rev. Lett.*, 47(19):1400, 1981. 78

[190] Jana Wolters. *Growth of NTCDA on Cu(001) studied by means of low-energy electron microscopy.* Master thesis, RWTH Aachen, 2016. 23, 45, 50, 60, 66, 67, IV, V, VI

[191] D. P. Woodruff. Normal incidence X-ray standing wave determination of adsorbate structures. *Prog. Surf. Sci.*, 57(1):1–60, January 1998. 18

[192] D. P. Woodruff. Surface structure determination using x-ray standing waves. *Reports Prog. Phys.*, 68(4):743–798, April 2005. 18

[193] M. Xu, T. Liang, M. Shi, and H. Chen. Graphene-Like Two-Dimensional Materials. *Chem. Rev.*, 113:3766–3798, 2013. 2, 69

[194] Fan Yang, Max Shtein, and Stephen R. Forrest. Controlled growth of a molecular bulk heterojunction photovoltaic cell. *Nat. Mater.*, 4:37–41, 2005. 1

[195] Dietrich R. T. Zahn, Gianina N. Gavrila, and Georgeta Salvan. Electronic and Vibrational Spectroscopies Applied to Organic/Inorganic Interfaces. *Chem. Rev.*, 107(4):1161–1232, 2007. 1, 29, 39

[196] J. Zegenhagen. Surface Structure Analysis with X-ray Standing Waves. *Physica Scripta*, T39(T39):328–332, January 1991. 18

[197] J. Zegenhagen. Surface structure determination with X-ray standing waves. *Surf. Sci. Rep.*, 18(7-8):202–271, October 1993.

[198] Jörg Zegenhagen and Alexander Kazimirov. *The X-ray standing wave technique : principles and applications, Series on Synchrotron Radiation Techniques and Applications Vol. 7.* World Scientific, 2013. 18

[199] Yanhong Zhang, Xuefei Weng, Huan Li, Haobo Li, Mingming Wei, Jianping Xiao, Zhi Liu, Mingshu Chen, Qiang Fu, and Xinhe Bao. Hexagonal boron nitride cover on Pt(111): A new route to tune molecule-metal interaction and metal-catalyzed reactions. *Nano Lett.*, 15(5):3616–3623, 2015. 73

[200] X. Zhu. Electronic structure and electron dynamics at molecule-metal interfaces: implications for molecule-based electronics. *Surf. Sci. Rep.*, 56(1-2):1–83, November 2004. 1, 29, 39

[201] J. Ziroff, P. Gold, A. Bendounan, F. Forster, and F. Reinert. Adsorption energy and geometry of physisorbed organic molecules on Au(111) probed by surface-state photoemission. *Surf. Sci.*, 603(2):354 – 358, 2009. 39

Chapter 9

Acknowledgement

This work would not have been possible without the assistance and contribution of many people. I would like to thank:

- first of all Christian Kumpf: thank you for creating such a warm, open and productive working atmosphere in our group. I never met a person who is able to give criticism in such a constructive way. Thank you for including us in decisions which were effecting us directly. Thank you for our countless discussions about my data. Thank you for your many encouraging words and your open door politics often used by myself.
- Joachim Mayer: thank you for agreeing to co-referee my PhD thesis.
- Caroline Henneke: thank you for your excellent introduction into the LEEM setup and for sharing your enormous LEEM experience so that it was possible for me to develop my own magic hands and to have some "Caro moments". Thank you for introducing me to all important "LEEM people" and for your good advice also in interpersonal questions. It was a pleasure to work with you.
- Markus Franke: thank you for your possibility to smile even if the whole UHV system has been vented unintendedly. Thank you for your never-ending patience in giving me advice for problems in the lab. Thank you for our long discussion about my/our data. Thank you for your good mood in the night shifts during my only beam time, our nice stay in London with Jana before and the many enjoyable evenings during business trips with beer and wine. The last three years would have been only half as much fun without you and more than twice as hard.
- Jana Wolters: thank you for your support during your year as a Master student at the LEEM. It was great to get to know the LEEM together and to work on my first LEEM project in a team with you. Thank you for making me a "Mastermama" for the first time.
- Miriam Raths: thank you for your help, patience and reliability during your year as a Master student at the LEEM. Take good care of the LEEM.
- Anja Haags: thank you for your help, enthusiasm and your drive to question many things during your time as a Master student at the LEEM. Thanks for a lot of spontaneous journeys home.

- all members of the Kumpf group: thank you for many fruitful discussions, new ideas, helping hands in the lab and a lot of fun.
- Philipp und Taner: thank you for making the coffee breaks to a source for new ideas and a good mood.
- the Elmitec team, especially Torsten, Florian and Helder: thank you for your quick and thorough help with the LEEM which was often just one call away.
- the Sokolowski group: thank you for the fruitful discussions about hBN on Cu(111) and PTCDA on hBN/Cu(111).
- F. Stefan Tautz: thank you for the chance to work on my PhD thesis in PGI-3 and for the hard work you spend to provide the institute's infrastructure.
- all members of the PGI-3: thank you for the good atmosphere. Thank you for supporting my work in our institute with discussions about my data, by lending equipment, by solving scientific or organizational problems and helping with all possible small tasks in the lab.
- finally my family and friends, especially, my parents, my sister and Kristof: thank you for your loving support and words of encouragement throughout every condition of my life. I would not be the person I am today without you. Thank you for providing me with your incredible belief in me and for helping me to realize my dreams.

Band / Volume 193
Group IV (Si)GeSn Light Emission and Lasing Studies
D. Stange (2019), vi, 151 pp
ISBN: 978-3-95806-389-1

Band / Volume 194
Construction and analysis of a spatially organized cortical network model
J. Senk (2019), 245 pp
ISBN: 978-3-95806-390-7

Band / Volume 195
Large-scale Investigations of Non-trivial Magnetic Textures in Chiral Magnets with Density Functional Theory
M. Bornemann (2019), 143 pp
ISBN: 978-3-95806-394-5

Band / Volume 196
Neutron scattering
Experimental Manuals of the JCNS Laboratory Course held at Forschungszentrum Jülich and at the Heinz-Maier-Leibnitz Zentrum Garching
edited by T. Brückel, S. Förster, G. Roth, and R. Zorn (2019),
ca 150 pp
ISBN: 978-3-95806-406-5

Band / Volume 197
Topological transport in non-Abelian spin textures from first principles
P. M. Buhl (2019), vii, 158 pp
ISBN: 978-3-95806-408-9

Band / Volume 198
Shortcut to the carbon-efficient microbial production of chemical building blocks from lignocellulose-derived D-xylose
C. Brüsseler (2019), X, 62 pp
ISBN: 978-3-95806-409-6

Band / Volume 199
Regulation and assembly of the cytochrome *bc*$_1$-*aa*$_3$ supercomplex in *Corynebacterium glutamicum*
C.-F. Davoudi (2019), 135 pp
ISBN: 978-3-95806-416-4

Band / Volume 200
Variability and compensation in Alzheimer's disease across different neuronal network scales
C. Bachmann (2019), xvi, 165 pp
ISBN: 978-3-95806-420-1

Schriften des Forschungszentrums Jülich
Reihe Schlüsseltechnologien / Key Technologies

Band / Volume 201
Crystal structures and vibrational properties of chalcogenides: the role of temperature and pressure
M. G. Herrmann (2019), xi, 156 pp
ISBN: 978-3-95806-421-8

Band / Volume 202
Current-induced magnetization switching in a model epitaxial Fe/Au bilayer
P. Gospodarič (2019), vi, 120, XXXVIII pp
ISBN: 978-3-95806-423-2

Band / Volume 203
Network architecture and heme-responsive gene regulation of the two-component systems HrrSA and ChrSA
M. Keppel (2019), IV, 169 pp
ISBN: 978-3-95806-427-0

Band / Volume 204
Spin-orbitronics at the nanoscale: From analytical models to real materials
J. Bouaziz (2019), 228 pp
ISBN: 978-3-95806-429-4

Band / Volume 205
Advanced methods for atomic scale spin simulations and application to localized magnetic states
G. P. Müller (2019), xx, 194 pp
ISBN: 978-3-95806-432-4

Band / Volume 206
Different growth modes of molecular adsorbate systems and 2D materials investigated by low-energy electron microscopy
J. E. Felter (2019), vi, 114, XXXIV pp
ISBN: 978-3-95806-434-8

Schlüsseltechnologien / Key Technologies
Band / Volume 206
ISBN 978-3-95806-434-8

Mitglied der Helmholtz-Gemeinschaft